e-ISSN: 2667-7814

$$Zn(OH)_{2(s)} \rightleftharpoons Zn^{2+}_{(aq)} + 2OH^{-}_{(aq)}$$

$$m = \frac{f(x_2) - f(x_1)}{x_2 - x_1}$$

ALANYA ALAADDİN KEYKUBAT ÜNİVERSİTESİ

0101001
1111101
0101010
0101001
1111101
0101001

ALKÜ FEN BİLİMLERİ DERGİSİ

Cilt: 7 Sayı: 1 (Ocak-Nisan 2025)

ALKU JOURNAL OF SCIENCE

Volume: 7 Issue: 1 (January-April 2025)

$$\lambda = \frac{h}{p} = \frac{h}{mv} = \frac{h}{\sqrt{2mE_k}}$$

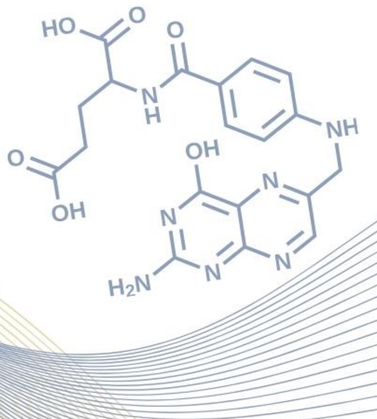

$$E = mc^2$$

DERGİNİN KÜNYESİ / *JOURNAL INFO*

Derginin Adı / *Journal Name*: ALKÜ Fen Bilimleri Dergisi / ALKU Journal of Science

Kısa Adı/ *Short Name*:

e-ISSN: 2667-7814

Doi prefix: 10.46740/alku.

Yayın Dili / *Publication Language* : Türkçe / *English*

Yayın Periyodu / *Publication Period*: Yılda üç kez (Nisan, Ağustos ve Aralık) / *Three times a year (April, August, and December)*

Sahibi / *Owner*: Prof. Dr. Kenan Ahmet TÜRKDOĞAN, Alanya Alaaddin Keykubat Üniversitesi Rektörü

Sorumlu Yazı İşleri Müdürü / *Publishing Manager*: Doç. Dr. Sefa YILDIRIM

Kuruluş / *Establishment*: ALKÜ Fen Bilimleri Dergisi, Alanya Alaaddin Keykubat Üniversitesi Rafet Kayış Mühendislik Fakültesi tarafından tüm mühendislik bilimleri ve temel bilimler alanında yılda 3 kez yayınlanan hakemli bir dergidir. Dergimizde, Türkçe ve İngilizce dillerinde orijinal araştırma çalışmaları ve derlemeler yayımlanmaktadır. Bu dergi, hakemli ve açık erişimli bir uluslararası mühendislik bilimleri ve temel bilimler dergisidir. Değerlendirme ve yayınlanma süreçlerinde yazarlardan ücret talep edilmez.

ALKU Journal of Science is an international, peer-reviewed journal which is published by Rafet Kayış Engineering Faculty of Alanya Alaaddin Keykubat University in all areas of engineering and basic science. ALKU Journal of Science is a triannually published open access journal operating an online submission and peer review system which allows authors to submit articles online and track their progress. No charges are required from the authors in all of the publication steps.

Dizinler ve Platformlar / I*ndexing and Platforms*: Google Scholar, Cosmos Impact Factor, ResearchBip, Bielefeld Academic Search Engine (BASE), Asos Index, International Innovative Journal Impact Factor(IIJIF), Scientific Indexing Services(SIS)

Web Adresi/ *Web address* : https://dergipark.org.tr/tr/pub/alku

Yayınlayan Kuruluş / *Publisher* : Alanya Alaaddin Keykubat Üniversitesi / Alanya Alaaddin Keykubat University

Makale gönderim ve takip sistemi / *Article submission and tracking system*: ULAKBİM Dergi Sistemleri, https://dergipark.org.tr/tr/pub/alku

Web barındırma ve teknik destek / *Web hosting and technical support*: Dergipark Akademik http://dergipark.gov.tr/
İletişim / *Contact*: Alanya Alaaddin Keykubat Üniversitesi, Rafet Kayış Mühendislik Fakültesi, Alanya, Antalya. E-mail: alkufbd@alanya.edu.tr Tel/Phone: 0242 5106060 (2545)

Doç. Dr. Üyesi Emrah Irmak, Alanya Alaaddin Keykubat Üniversitesi, Rafet Kayış Mühendislik Fakültesi, Elektrik Elektronik Mühendisliği Bölümü. Alanya, Antalya
Subject: Electrical-Electronical Engineering
Alan: Elektrik-Elektronik Mühendisliği

Doç. Dr. Murat Aksel, Alanya Alaaddin Keykubat Üniversitesi, Rafet Kayış Mühendislik Fakültesi, İnşaat Mühendisliği Bölümü Alanya, Antalya
Subject: Civil Engineering
Alan: İnşaat Mühendisliği

Dr. Öğr. Üyesi Fatma Aydın Ünal, Alanya Alaaddin Keykubat Üniversitesi, Rafet Kayış Mühendislik Fakültesi, Metalurji ve Malzeme Mühendisliği Bölümü. Alanya, Antalya
Subject: Metallurgical and Materials Engineering
Alan: Metalurji ve Malzeme Mühendisliği

Dr. Öğr. Üyesi Atıl Kurt, Alanya Alaaddin Keykubat Üniversitesi, Rafet Kayış Mühendislik Fakültesi, Endüstri Mühendisliği. Alanya, Antalya
Subject: Industrial Engineering
Alan: Endüstri Mühendisliği

Dr. Öğr. Üyesi Özgür Öztürk, Alanya Alaaddin Keykubat Üniversitesi, Rafet Kayış Mühendislik Fakültesi, Genetik ve Biyomühendislik Bölümü. Alanya, Antalya
Subject: Genetics and Bioengineering
Alan: Genetik ve Biyomühendislik

Dr. Öğr. Üyesi Korhan Ökten, Amasya Üniversitesi, Mühendislik Fakültesi, Makine Mühendisliği Bölümü, Amasya
Subject: Mechanical Engineering
Alan: Makine Mühendisliği

Dr. Öğr. Üyesi Mehmet Masum Tümçay, Marmara Üniversitesi, Mühendislik Fakültesi, Metalurji ve Malzeme Mühendisliği Bölümü, İstanbul
Subject: Metallurgical And Material Engineering
Alan: Metalurji ve Malzeme Mühendisliği Bölümü

Dr. Öğr. Üyesi Ahmad Reshad Noori, İstanbul Gelişim Üniversitesi, Mühendislik ve Mimarlık Fakültesi, İnşaat Mühendisliği Bölümü, İstanbul
Subject: Civil Engineering
Alan: İnşaat Mühendisliği

Dr. Öğr. Üyesi Derya Dinler, Hacettepe Üniversitesi, Mühendislik Fakültesi, Endüstri Mühendisliği Bölümü, Ankara
Subject: Industrial Engineering
Alan: Endüstri Mühendisliği

YAYIN, DİL ve TEKNİK EDİTÖRLERİ / PUBLISHING, LANGUAGE AND TECHNICAL EDITORS

ALKÜ FEN BİLİMLERİ DERGİSİ 2025:7(1)

ALKU JOURNAL OF SCIENCE 2025:7(1)

İçindekiler / Contents

ALKU Journal of Science 2025, Sayı 7(1): 1-14
e-ISSN: 2667-7814

Original Article

Measurement of Acoustic Parameters of the Multipurpose Alev Alatlı Conference Hall

Akın Oktav[1,2*], Mehmet Şahin[2]
[1]Department of Mechanical Engineering, Alanya Alaaddin Keykubat University, Antalya, Türkiye.
[2]Vibration and Acoustics Laboratory, Alanya Alaaddin Keykubat University, Antalya, Türkiye
**akin.oktav@alanya.edu.tr*

Abstract

Multi-purpose halls are used for a wide range of activities, from conferences to concerts, theatre performances to sporting events. The acoustic performance of such halls can vary greatly depending on the type of event, temperature variations, and occupancy of the hall. Therefore, determining the acoustic characteristics of a multi-purpose hall is critical to ensure that the venue can provide the best acoustic performance in every usage scenario. A measurement survey is conducted in a multipurpose conference hall through 2 different stimuli and at 2 different temperatures. The response of the hall is recorded at 10 receiver locations using omnidirectional microphones and a dummy head. The reverberation time, early decay time, bass ratio, center time, clarity, definition, rapid speech transmission index, and inter aural cross-correlation are extracted from the raw data. The results are compared to the relevant standards and the literature to evaluate the acoustic performance.

Keywords: Multipurpose hall acoustics, room acoustic parameters, room impulse response, acoustical performance.

Çok Amaçlı Alev Alatlı Konferans Salonunun Akustik Parametrelerinin Ölçülmesi

Özet

Çok amaçlı salonlar, konferanslardan konserlere, tiyatro gösterilerinden spor etkinliklerine kadar çok çeşitli etkinlikler için kullanılmaktadır. Bu tür salonların akustik performansı, etkinliğin türüne, sıcaklık değişimlerine ve salonun doluluk oranına bağlı olarak büyük ölçüde değişebilir. Bu nedenle, çok amaçlı bir salonun akustik özelliklerinin belirlenmesi, mekânın her kullanım senaryosunda en iyi akustik performansı sağlayabilmesini sağlamak için kritik öneme sahiptir. Çok amaçlı bir konferans salonunda 2 farklı uyaran ve 2 farklı sıcaklıkta bir ölçüm araştırması gerçekleştirilmiştir. Salonun tepkisi, çok yönlü mikrofonlar ve bir yapay kafa kullanılarak 10 alıcı konumunda kaydedilmiştir. Ham veri işlenerek yankılanma süresi, erken sönümlenme süresi, bas oranı, merkez süresi, netlik, tanımlama, hızlı konuşma iletim indeksi ve işitsel çapraz korelasyon elde edilmiştir. Akustik performansı değerlendirmek için sonuçlar ilgili standartlar ve literatürle karşılaştırılmıştır.

Anahtar Kelimeler: Çok amaçlı salon akustiği, oda akustik parametreleri, oda dürtü yanıtı, akustik performans.

Geliş/Received: 8 Eylül/8 September 2024
Kabul Ediliş/Accepted: 10 Aralık/10 December 2024

1. INTRODUCTION

The acoustic requirements of the spaces are different, and these requirements are determined according to the intended use. If a space is to be designed as a theatre hall, the targeted room acoustic parameters will be different, for example, if the same space is used as a concert hall, the result may not satisfy the audience. Nevertheless, there is a demand for the same space to be used for different purposes. In this case, it may be preferable to compromise on the ideal values for each requirement, not to have ideal acoustic properties for any event, but still to be able to meet all requirements to some extent. Another way to meet this demand is to use movable panels, directional diffusers, and sound curtains and to adjust these components according to the types of activities. According to Holden [1], this demand dates to the 1920s.

Single-purpose halls are rare due to their high construction costs and operational expenses. Nevertheless, people want to organize a large number and variety of activities and come together. For example, in universities, different activities are constantly organized for students to develop and have a good time. In addition, events such as commemorations and celebrations take place frequently. These events are usually organized in conference halls. In these organizations, speeches are given from the lectern, and from time to time there are also trio and quartet concerts. In some activities, solo and choral singing can be performed. In addition, presentations can be made on the screen and sound recordings can be played. All these activities point to the need to pay attention to more parameters than the intelligibility of the speech for the acoustic performance of the space.

In this study, a multi-purpose conference hall is considered and the adequacy of its acoustic performance in terms of different activities is investigated. For the research, impulse response was measured with a dodecahedron sound source in the hall, and 2 different types of microphones were used: omnidirectional and dummy head. The impulse responses are usually measured using either Maximum Length Sequence (MLS) or Exponential Sine Sweep (ESS) signals. Both signals were used to measure the objective room acoustic parameters, and the results were compared. Another concern is changes in room temperature during these activities. Although the temperature in the halls is tried to be kept constant with air conditioning systems, the room temperature may increase during the performance due to the presence of the audience. Measurements were made at two different temperatures, 25°C and 30°C, and the changes caused by the temperature difference on the room acoustic parameters were investigated.

2. DATA AND METHODS

2.1 Stimuli

In acoustic measurements, the impulse response (IR) and linear transfer function of the system are characterized. The most used technique for IR measurement is the MLS. The MLS signal is comparable to white noise, which is non-periodic and random in nature. The measurement requires long measurement time averaging to ensure that it accurately estimates its spectrum. It is a pseudo-random noise sequence that can be seen as a long sequence of perfect impulses with a perfect white spectrum. In practice, such a signal consists of a distributed sequence of identical positive and negative pulses of the same amplitude, so that it is symmetric around 0 [2]. The pseudo-random MLS signal has a full frequency spectrum, and the sound of MLS signals is less disturbing compared to the intrusive sound produced by sweep signals. When using this technique, it is assumed that the system behaves linearly and does not change over time. When these assumptions are not fully met, problems may arise in measurements.

It is possible to simultaneously solve the linear IR of the system and separate IRs for each harmonic distortion order by using a sine signal whose frequency varies exponentially. This method, known as exponential sine sweeps (ESS), is recommended because it separates harmonic distortion and gives higher impulse–noise ratios (INR) under usual test conditions [3-5]. Farina [6] showed that by using a sine signal whose frequency varies exponentially, it is possible to simultaneously resolve the linear impulse response of the system and separate impulse responses for each order of harmonic distortion. The use of exponential sine sweep (ESS) for impulse stimulation was adopted in relevant works [7-10].

To compare the MLS and ESS signals, the researchers made measurements in a concert hall [4]. In the 500 Hz octave band, the energy/decay plot of the ESS measurement showed that a longer valid decay interval is needed for RT calculation compared to MLS. They showed that under ideal measurement conditions without any disturbing noise, the differences in the RT calculation from a measurement with MLS and ESS are very small. Antoniadou et al. [5] generated artificial background noise and investigated how this noise changes the acoustic parameters for MLS and ESS measurements. The researchers report that MLS methods give better results for white, narrowband, and tonal high background noise, but in the case of impulsive noise, the ESS method performs well [11].

To evaluate the results in a multipurpose conference hall both stimuli, MLS and ESS are used, and raw data are collected in the current work.

2.2 Effect of the Temperature

Even though the halls are assumed to be linear time invariant (LTI) systems, they are exposed to some dynamic changes which alter their characteristics like room acoustic parameters. Temperature and relative humidity changes are some of these dynamic changes. Temperature and relative humidity are constantly changing in halls, especially during performances, with the presence of the audience and the operation of HVAC systems. As stated in a recent work, these changes alter the reverberation time (RT), and this variation is frequency-dependent [12]. The variance in RT also affects the other acoustic parameters like speech transmission index (STI) and clarity (C80) [13-15]. Recent studies show that RT at high frequencies increases and STI decreases when temperature and humidity increase [16]. It was observed that temperature and relative humidity changes were more effective on C80 and T30 parameters, while D50 and EDT were less affected by these changes.

For comparison, the measurements are repeated in two different temperatures, 25°C and 30°C in the current work.

2.3 Descriptors of Room Acoustics

The following descriptors of room acoustics are extracted from the raw data: reverberation time (RT), early decay time (EDT), bass ratio (BR), center time (Ts), clarity (C80), definition (D50), rapid speech transmission index (RASTI), and inter aural cross-correlation (IACC) [17, 18].

RT is the time required for the sound energy in the space to decrease by 60 dB after the source emission has ceased. This change means a reduction in sound intensity to one part per million (10 log 1,000,000 = 60 dB) or a reduction in sound pressure level to one part per thousand (20 log 1,000,000 = 60 dB).

EDT is the time required for a 10 dB reduction of the field-averaged sound energy after the source emission is stopped. It is multiplied by 6 to make it comparable to RT. The abbreviations RT10 and T10 are also used in the literature for EDT. The EDT is a variable that considers especially the earlier and louder parts of the room acoustics. It is therefore related to the masking threshold of reflections, which partially mask the direct sound, causing ambiguity and incomprehensibility. Also, like the reverberation impression, the EDT can vary between different locations in the room.

BR is defined as the ratio of RT at low frequencies to those at mid frequencies in full auditoriums. It is calculated as the sum of the RT values at 125 and 250 Hz divided by the sum of the RT values at 500 and 1,000 Hz. BR with a value of unity indicates a balance between low and mid frequencies in the response of the space. However, high BR values are not desired for speech intelligibility.

$$BR = \frac{RT_{125} + RT_{250}}{RT_{500} + RT_{1,000}} \qquad (1)$$

Ts is defined as the variable that gives the center of gravity of the damped sound field with respect to the time axis. It has an inverse correlation with D50 and C80. Low values mean that the definition and clarity are good. Depending on the type of music, a value range of 70-150 ms is considered ideal. In Equation (2) $g(\tau)$ is impulse response.

$$T_s = \frac{\int_0^\infty \tau g^2(\tau) d\tau}{\int_0^\infty g^2(\tau) d\tau} \tag{2}$$

C80 is defined as the difference between the sound energy in the first 80 ms and the late reverberation energy after the first 80 ms. Used as an indicator of the clarity of music, C80 defines the degree to which the details of simultaneous (vertical) and consecutive (horizontal) sounds can be perceived distinctly. Early reflections are integrated directly into the sound by the auditory system and therefore have an amplifying effect. Reverberation has a masking effect and therefore reduces clarity. Therefore, a compromise between reverberation and clarity is desirable. Since it varies with frequency, it needs to be weighted. For this purpose, the average of the C80 values in the frequency octave bands centred at 500 Hz, 1,000 Hz, and 2,000 Hz is commonly used. This average is expressed by the abbreviation C80(3). Depending on the type of music, a C80 value of -3.2 dB to 0.2 dB is considered ideal.

$$C_{80} = 10 \log_{10} \left(\frac{\int_0^{80\text{ms}} g^2(\tau) d\tau}{\int_{80\text{ms}}^\infty g^2(\tau) d\tau} \right) \tag{3}$$

D50 is a measure of how well the vocal is intelligible in a space. It is defined as the ratio of sound energy arriving early (0-50 ms after direct sound arrival) to the total received energy. The values of different frequency bands need to be weighted to obtain a single number. The ISO 3382-1 [19] standard recommends that the single D50 number be obtained from the average of the 500 and 1,000 Hz octave bands. The first acoustic reflections arriving very soon after the direct sound have a positive effect on the audience's ability to recognise the vocal, whereas reflections arriving 50 ms or more after the direct sound have a negative effect.

$$D_{50} = \frac{\int_0^{50ms} g^2(\tau) d\tau}{\int_0^\infty g^2(\tau) d\tau} \leq 1 \tag{4}$$

Spatial information is obtained by utilizing binaural hearing and the differences between the sound heard by the two ears. It is about the perception of the spaciousness of the space i.e., listener envelopment. IACC is the maximum absolute value of the interaural cross-correlation function (IACF), and it is an objective descriptor of the perception of the spaciousness of the space.

$$IACF\,(t) = \frac{\int_{t_{min}}^{t_{max}} g_r(\tau) g_l(\tau + t) d\tau}{\left(\int_{t_{min}}^{t_{max}} g_l^2(\tau) d\tau \int_{t_{min}}^{t_{max}} g_r^2(\tau) d\tau \right)^{1/2}} \tag{5}$$

The impulse responses, $g_{l,}$ and g_r, can be measured through the left and right microphones built into a dummy head. IACC is given as

$$IACC = \max\{|IACF(t)|\} \tag{6}$$

Since the difference between STI and rapid speech transmission index (RASTI) is often small, RASTI is used instead of STI as an objective descriptor of speech intelligibility. RASTI is defined as [20]

$$RASTI = \frac{\text{ave}\{SNR(\Omega)\} + 15\text{dB}}{30\text{dB}} \tag{7}$$

where averaging is done over all modulation frequencies (Ω), and SNR is the signal-to-noise ratio.

2.4 Alev Alatlı Hall

Measurements were made in a multipurpose conference hall located at Alanya Alaaddin Keykubat University. Opened in 2023, the 264-seat hall is used for conferences, trio or quartet concerts, and various events. The length of the hall is 19.80 m, width 15.90 m, average height 3.46 m, and volume 1,077 cubic meters. The dimensions of the space are tabulated in Table 1.

In the hall, the stage floor is covered with parquet, and the rest of the floor is covered with tufted pile carpet. As can be seen in Figure 1, a certain part of the walls and ceiling are covered with fabric and the remaining area is painted plaster surface. The audience seats in the hall are covered with heavily upholstered fabric. The side view of the hall is shown in Figure 2 where the dimensions are also depicted.

Table 1. The dimensions of the hall

Volume (V)	1,077 m^3
Surface area	314.82 m^2
Number of seats (N)	264
Stage area	52.53 m^2
V/N	4.08

Figure 1. Alev Alatlı hall located at Alanya Alaaddin Keykubat University, Antalya, TR

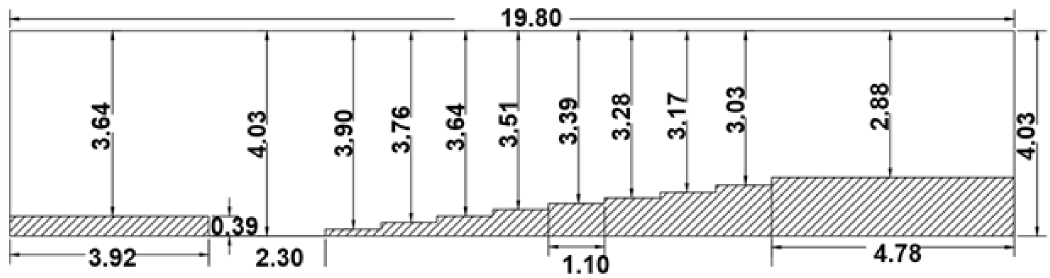

Figure 2. The side view of the hall, and the dimensions are all in meters

2.5 Data acquisition

A dodecahedral sound source Sinus QS-12 which can produce sound suitable for measuring between 50 Hz and 16,000 Hz with a level of 122 dB in the smooth broadband spectrum is used. The required directivity meets the relevant standards, ISO 10140 [20] and ISO 16283 [21]. Stimulation was performed using MLS and ESS in six octave bands (125 Hz – 4,000 Hz). The RIR is recorded with Gras 46AE (omnidirectional), Neumann and Neumann KU 100 (dummy head) microphones. Measurements were performed according to ISO 3382-1. Microphone measurements are transferred to a computer via a Focusrite Scarlett audio interface. The recorded raw sound signals are processed using Dirac v7.1 software. The setup is introduced in Figure 3.

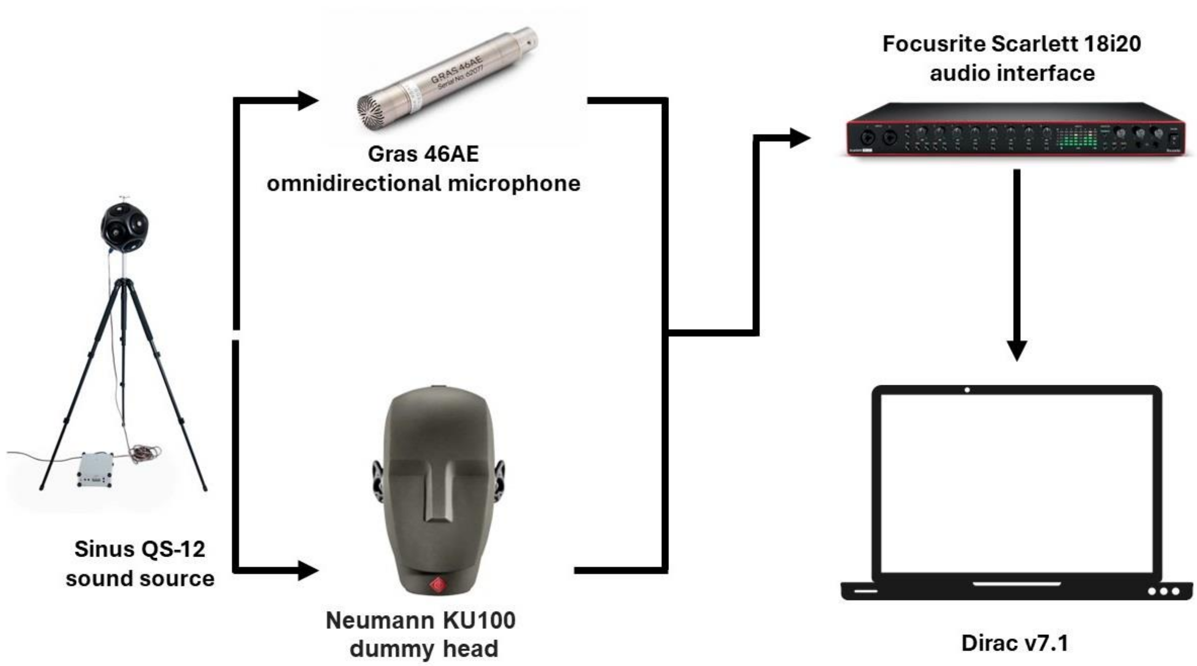

Figure 3. Setup for data acquisition

The measurements were performed on July 10th, 2024, during an 8-hour working period. During the measurements the hall was unoccupied and 2 average temperatures were set, 25ºC and 30ºC. The minimum, maximum and average values of temperature and relative humidity recorded during measurement are tabulated in Table 2. Air conditioning systems were used to maintain the appropriate temperature in the hall and were switched off during the measurements. The background noise level (BNL) of the environment was measured with a Gras 46AE omnidirectional microphone using Sinus Samurai software. During the measurement, the microphone was positioned at the geometric centre of the hall. The BNL of the space was measured as 35.9 dBA. Raw sound data was collected from a total of 10 locations. At 9 locations omnidirectional microphones are used and at 1 location a dummy head is used. The microphones and their locations are shown in Figure 4. For the measurement of the IACC parameter, the dummy head was positioned at the geometric center of the hall.

Table 2. Temperature and relative humidity values during the measurement survey

Temperature (Celsius)			Relative humidity (percent)		
Min	Max	Average	Min	Max	Average
24.08	26.72	25.28	44.72	52.37	47.15
26.72	32.66	30.08	41.12	47.02	44.49

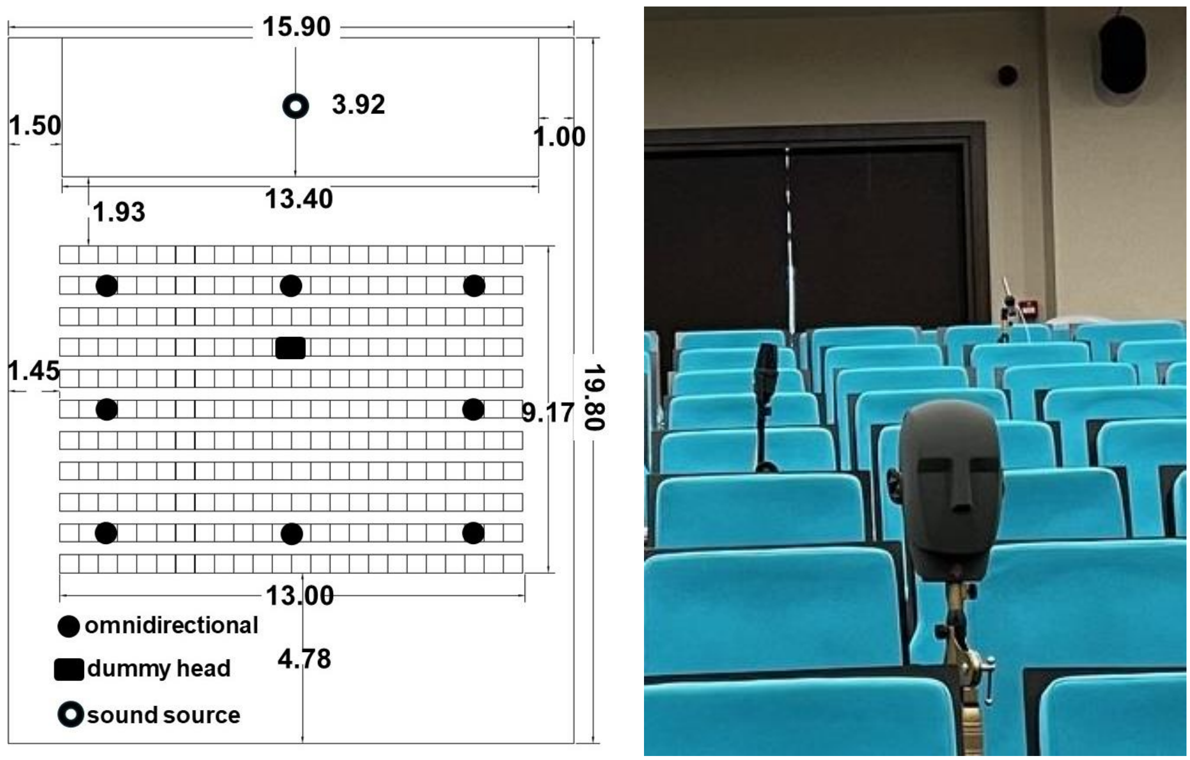

a) Measurement positions
b) Microphones

Figure 4. The floor plan of the space and the positions of the stimulus and the receivers (in meters)

3. RESULTS

The raw data is processed using Dirac v7.1, and acoustic parameters are derived. The parameters obtained through MLS stimulus are tabulated in Table 3 and Table 4 for 25ºC and 30ºC, respectively. For comparison, the parameters obtained through ESS stimulus are also tabulated in Table 5 and Table 6 for 25ºC and 30ºC, respectively.

The parameters RT, EDT, Ts, C80, and D50 are derived in 6 octave bands i.e. 125 Hz – 4,000 Hz. The other parameters, BR and RASTI, are given in Tables 3 to 6 according to their definitions, as they are derived as ratios or averages. The definitions are given in Equation 1 and Equation 7. The values of IACC parameter are measured only through the ESS stimulus and they are tabulated in Table 5 and Table 6 for two different temperatures.

Table 3. Acoustic parameters derived from MLS stimulus-response at 25ºC

Octave (Hz)		125	250	500	1,000	2,000	4,000
RT (s)		0.69	0.73	0.74	0.75	0.87	0.78
EDT (s)		0.51	0.55	0.54	0.60	0.66	0.68
Ts (ms)		51.73	42.41	38.45	39.93	41.41	41.58
C80 (dB)		8.82	8.39	8.84	7.61	7.29	7.10
D50		0.75	0.74	0.76	0.73	0.72	0.70
BR	0.87						
RASTI	0.67						

Table 4. Acoustic parameters derived from MLS stimulus-response at 30ºC

Octave (Hz)		125	250	500	1000	2000	4000
RT (s)		0.49	0.54	0.55	0.61	0.72	0.67
EDT (s)		0.43	0.50	0.61	0.56	0.59	0.64
Ts (ms)		46.60	43.05	39.53	34.98	37.37	39.30
C80 (dB)		10.20	8.78	8.17	8.80	8.19	7.59
D50		0.77	0.77	0.72	0.76	0.76	0.72
BR	0.90						
RASTI	0.68						

Table 5. Acoustic parameters derived from ESS stimulus response at 25ºC

Octave (Hz)		125	250	500	1,000	2,000	4,000
RT (s)		0.69	0.73	0.74	0.75	0.87	0.78
EDT (s)		0.53	0.57	0.56	0.67	0.74	0.72
Ts (ms)		53.44	43.01	38.66	40.43	41.19	42.04
C80 (dB)		8.39	8.37	8.86	7.52	7.35	7.08
D50		0.74	0.74	0.76	0.72	0.73	0.70
BR	0.95						
IACC		0.98	0.81	0.42	0.63	0.65	0.35
RASTI	0.71						

Table 6. Acoustic parameters derived from ESS stimulus response at 30ºC

Octave (Hz)		125	250	500	1,000	2,000	4,000
RT (s)		0.71	0.73	0.68	0.74	0.83	0.76
EDT (s)		0.47	0.57	0.59	0.59	0.68	0.68
Ts (ms)		51.81	43.70	38.88	37.55	39.01	41.43
C80 (dB)		9.09	8.41	8.62	8.52	7.68	7.28
D50		0.75	0.75	0.74	0.74	0.74	0.71
BR	1.02						
IACC		0.98	0.85	0.45	0.65	0.63	0.36
RASTI	0.71						

The optimum RT depends on the type of music and the number of musical instruments on the stage. The volume of the hall studied is 1,077 cubic metres. The optimum reverberation time for symphonic music in this volume is around 1.4 s. The derived RT values show that the hall is not suitable for performing symphonic music.

Sufficient early vocal energy is crucial for speech intelligibility and D50 is a suitable indicator to assess this. The expected value for D50 for good speech intelligibility is 0.5 and above. The other relevant descriptor is RASTI, which is expected to be 0.6 and above in a multipurpose conference room to ensure the quality of oral communication. It can be seen from Tables 3 to 6 that the values of D50 and RASTI are well above the quality thresholds, indicating that the investigated multipurpose hall is suitable for conferences. The optimum values for RT are between 0.7s and 1.2s for speech, which should be about 1s for a hall of 1,000 cubic metres. Although the measured RT value of the studied hall is not optimal, it is within the optimum range.

In what follows, how the derived acoustic parameters change according to the stimulus and temperature is analysed on a parameter basis.

RT, EDT, C80, D50 and Ts values measured in response to ESS and MLS stimuli are compared in Figure 5. It is observed that the differences between the response curves are significant for RT parameter, especially at low frequencies. The change in the temperature amplifies the difference: The average of differences in RT are 20.7% and 23.8% at 25ºC and 30ºC, respectively. For EDT parameter, which is a measure of early reflections, the difference in responses to 2 different stimuli is moderate. According to these results it can be deduced that the effect of stimulus is more dominant for late reflections.

C80, a sound energy parameter, is used as an indicator of the clarity of the music. The measured values are far from the ideal range of -3.2 dB to 0.2 dB. The C80 values measured in response to 2 different stimuli at 25ºC are close in all 6 octave bands, but the average difference increased from 1.5% to 7.2% when the temperature increased. The same is true for D50 and Ts parameters.

In Figure 6, average differences observed in RT, EDT, C80, D50, and Ts at 25ºC and 30ºC are compared. It is observed that the measured values tend to deviate more as the temperature increases. However, the differences are slightly more moderate when the hall is stimulated using ESS. In the MLS technique, it is assumed that the system (hall) behaves linearly and does not change over time. When these assumptions are not met due to temperature changes and similar reasons, problems may arise in measurements. The ESS method is recommended because it separates harmonic distortion and gives higher impulse-to-noise ratios (INR) under usual test conditions [3-6, 11].

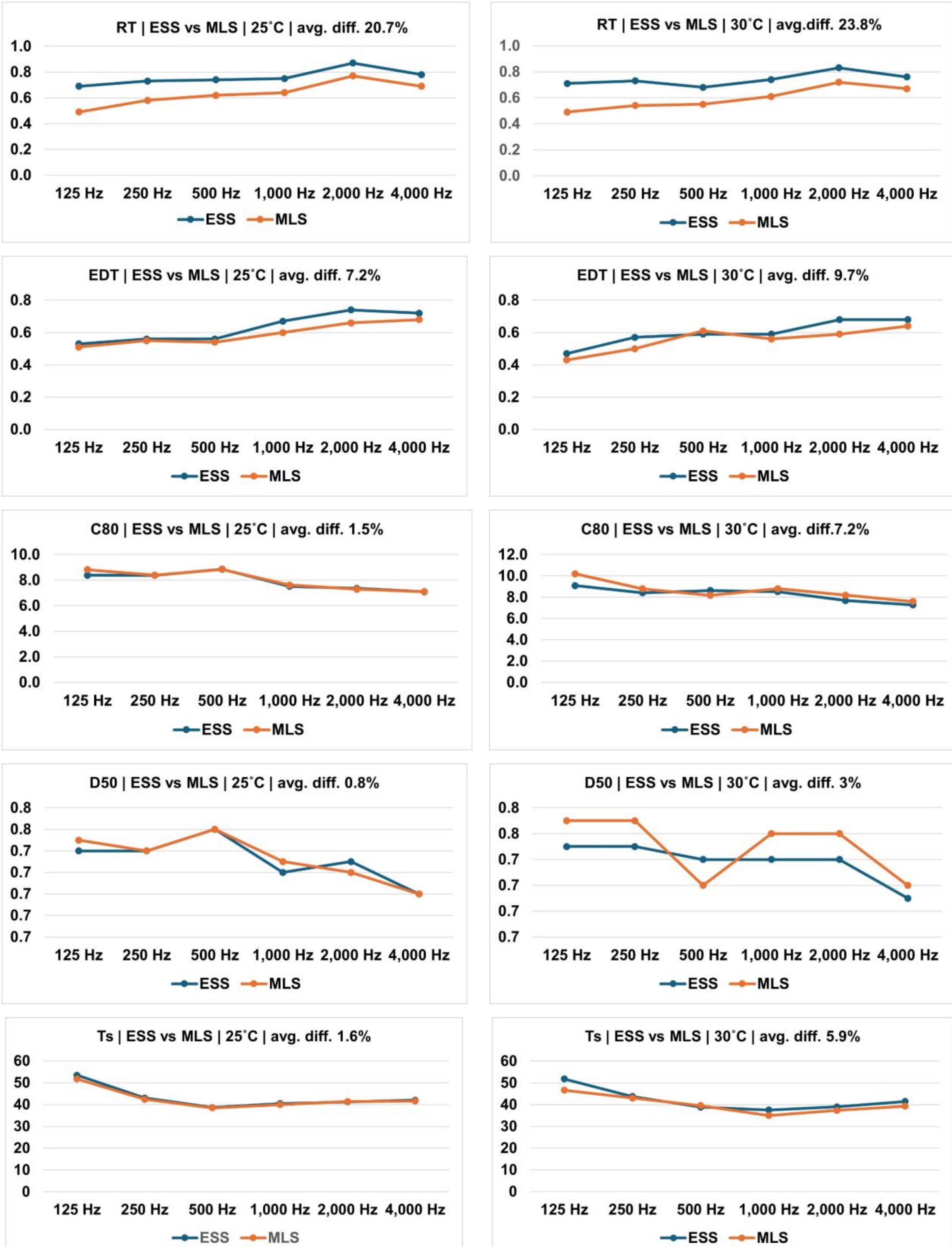

Figure 5. Average differences in RT, EDT, C80, D50, and Ts in response to ESS and MLS stimuli

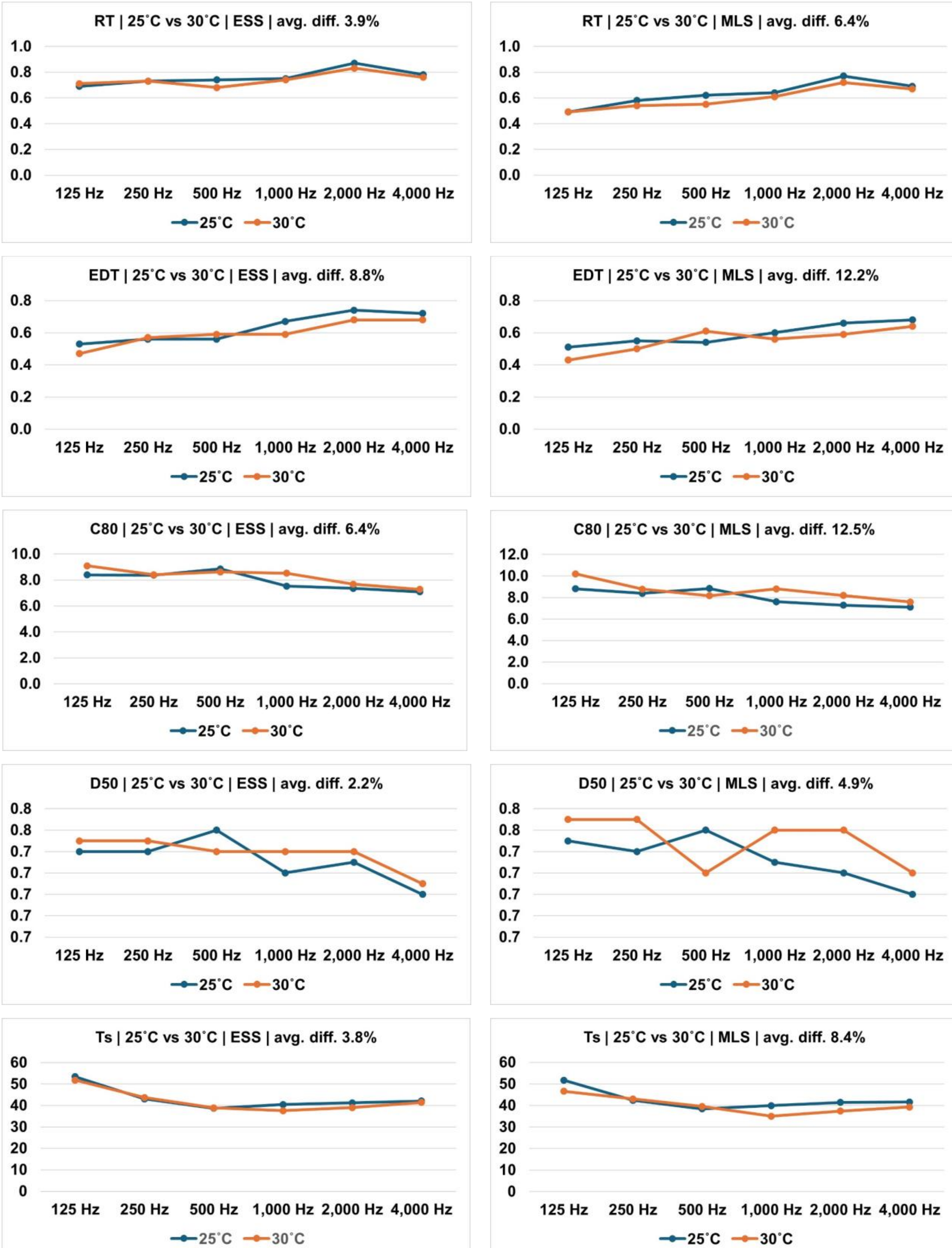

Figure 6. Average differences observed in RT, EDT, C80, D50, and Ts at 25ºC and 30ºC

The temperature differences also alter the IACC parameter which is a measure of binaural hearing. The measured results are compared in Figure 7.

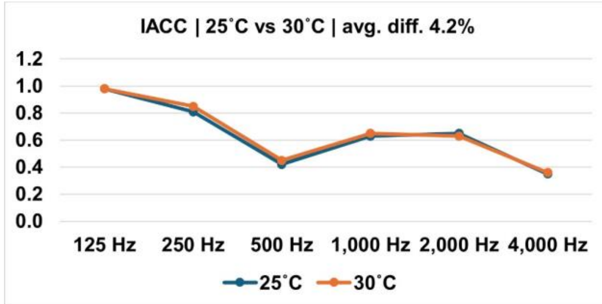

Figure 7. Average differences observed in IACC in response to ESS stimulus at 25ºC and 30ºC

It is desirable that BR, which is one of the important parameters for concert events, has a value of unity. When it is at the ideal value, it indicates that there is a balance between low and medium frequencies in the response of the venue. However, BR and RASTI parameters contradict each other. High BR values are not desirable for speech intelligibility. The BR and RASTI parameters, measured in response to ESS stimulus at 25ºC and 30ºC, are compared in Figure 8.

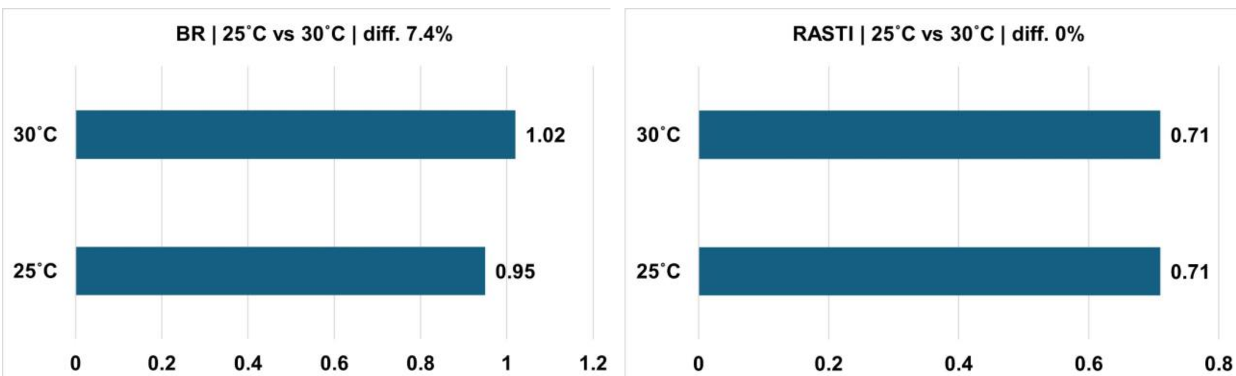

Figure 8. Differences observed in BR and RASTI in response to ESS stimulus at 25ºC and 30ºC

Temperature change increases the value of BR parameter. From this point of view, although the temperature increase seems to be positive, it is actually not. The reason is that it only increased BR; BR increased by 7.4%, while RASTI, an objective measure of speech intelligibility, did not change.

4. CONCLUSION

The results obtained showed that when dynamic variables such as temperature change are taken into consideration, it is more appropriate to make measurements with ESS excitation. This result is consistent with the related studies in the literature [3-5, 7-11].

The obtained results show that acoustic parameters are sensitive to temperature variations. In the initial design, it is generally assumed that the temperature value will remain constant. Considering that the acoustic performance may change negatively due to temperature changes, it is important to take every precaution to keep the temperature constant.

In the measurement survey, the reverberation time (RT), early decay time (EDT), clarity (C80), definition (D50), centre time (Ts), inter aural cross correlation (IACC), bass ratio (BR), and rapid speech transmission index (RASTI) are derived from the raw data. The acoustic performance is evaluated according to the raw data measured in response to exponential sine swept (ESS) stimulus at 25ºC. When the acoustic performance of the measured multipurpose Alev Alatlı Conference Hall is evaluated, the following conclusions can be drawn:

- The average value of RT is 0.76 s. This value is within the optimal range of 0.7 s-1.2 s defined for speech intelligibility. In this volume of 1.077 cubic metres, the optimal value defined for music is 1.4 s. Considering the measured value, it is understood that the volume will not provide an ideal experience for music performances.
- The average values of EDT and C80 are 0.63 s and 7.93 dB. EDT and C80 are more relevant for music performances and their impacts on speech intelligibility are very limited.
- The average value of D50 is 0.73 (or 73%). This value should be higher than 0.50 (or 50%) for a good speech intelligibility. It is well above the threshold. D50 is more concerned with speech intelligibility and its impact on musical performances is rather limited.
- The average value of Ts is 43.13 ms. For ideal speech intelligibility, this value should be below 100 ms. Since it is well below the defined threshold, it can be deduced that the hall is suitable for conference events. On the other hand, the measured value is not well suited for musical performances, where the expected Ts value is 100 ms-150 ms.
- The IACC (3) which refers to the early IACC calculated only the three middle octaves, 500 Hz, 1,000 Hz, and 2,000 Hz, is measured as 0.57. This parameter is more relevant for musical performances and is expected to be below 0.4.
- The BR value is measured as 0.95. It is desirable that the BR, which is an important parameter for musical performance, is between 1.1-1.4. On the other hand, values of 1 and above 1 reduce the intelligibility of speech.
- The RASTI value is measured as 0.71. The RASTI value is moderate between 0.45 and 0.59; good between 0.6 and 0.74; above 0.75 indicates excellent speech intelligibility.

When the measurement results are compared with the relevant standards and literature, it is evaluated that the multipurpose Alev Alatlı Conference Hall is quite sufficient for conference events, commemorations and celebrations, but not far from the sufficient level for musical performances.

5. ACKNOWLEDGEMENT

This study was supported by Scientific and Technological Research Council of Turkey (TUBITAK) under the Grant Number 123M884. The authors thank TUBITAK for their supports.

REFERENCES

[1] M. Holden, *Acoustics of Multi-Use Performing Arts Centers*, CRC Press, 2015.

[2] F. Policardi, "MLS and Sine-Sweep measurements," Università di Bologna, Italia *Elektrotehniški Vestnik,* vol. 78, no. 3, pp. 91-95, 2011.

[3] Q. Meng, D. Sen, S. Wang, and L. Hayes, "Impulse response measurement with sine sweeps and amplitude modulation schemes", *2nd Int. Conf. on Signal Processing and Communication Systems*, Gold Coast, QLD, Australia, 2008, pp. 1–5.

[4] P. Guidorzi, L. Barbaresi, D. D'Orazio and M. Garai, M, "Impulse responses measured with MLS or Swept–Sine signals applied to architectural acoustics: an in–depth analysis of the two methods and some case studies of measurements inside theatres," *Energy Procedia*, 2015, pp. 1611–1616.

[5] S. Antoniadou, N.M. Papadakis and G.E. Stavroulakis, “Measuring Acoustic Parameters with ESS and MLS methods: Effect of Artificially Varying Background Noise,” *Proc. of the Euronoise*, 2018, pp. 771–776.

[6] A. Farina, 2000, February. Simultaneous measurement of impulse response and distortion with a swept-sine technique. *In Audio Eng. Society Conv. 108. Audio Engineering Society*, Paris, 2000, Paper number 5903.

[7] L. Tronchin, F. Merli and M. Manfren, “On the acoustics of the Teatro 1763 in Bologna,”, *Appl. Acoust*, 172, 107598, 2021.

[8] A. Bevilacqua, S. Sukaj, G. Ciaburro, G. Iannace, I. Lombardi and A. Trematerra, “How a quartet of theatres play under an acoustic perspective: A comparison between horseshoe–shaped plans in Campania,” *Build. Acoust*, 351010X221080769, 2022.

[9] J.A. Almagro–Pastor, R. García–Quesada, J. Vida–Manzano, F.J. Martínez–Irureta and Á.F. Ramos–Ridao, “The Acoustics of the Palace of Charles V as a Cultural Heritage Concert Hall,” *Acoust*, vol.4, no.3, pp. 800–820, 2022.

[10] D. Alarcão, O. Inácio, “Determination of room acoustic parameters using spherical beamforming–The example of Lisbon’s Garrett Hall,”. *Appl. Acoust*, 192, 108734, 2022.

[11] N.M. Papadakis, S. Antoniadou and G.E. Stavroulakis, “Effects of varying levels of background noise on room acoustic parameters, measured with ESS and MLS methods,” *Acoust*, vol. 5, no. 2, pp. 563-574, 2023.

[12] A. Nowoświat, “Impact of temperature and relative humidity on reverberation time in a reverberation room,” *Build.*, vol. 12, no. 8, p. 1282, 2022.

[13] F. Leccese, M. Rocca and G. Salvadori, “Fast estimation of Speech Transmission Index using the Reverberation Time: Comparison between predictive equations for educational rooms of different sizes,” *Appl. Acoust*, vol. 140, pp. 143-149, 2018.

[14] N. Prodi, M. Pellegatti and C. Visentin, “Effects of type of early reflection, clarity of speech, reverberation, and diffuse noise on the spatial perception of a speech source and its intelligibility,” *J. Acoust. Soc. Am.*, vol. 151, no. 5, pp. 3522-3534, 2022.

[15] P. Götz, C. Tuna, A. Walther and E.A. Habets, “Online reverberation time and clarity estimation in dynamic acoustic conditions,” *J. Acoust. Soc. Am.*, vol. 153, no. 6, pp. 3532-3542, 2023.

[16] L. Tronchin, “Variability of room acoustic parameters with thermo-hygrometric conditions,” *Appl. Acoust*, vol. 177, p.107933, 2021.

[17] L.L. Beranek, *Concert Halls, and Opera Houses: Music, Acoustics, and Architecture*, Vol. 2. New York: Springer, 2004.

[18] H. Kuttruff, *Room Acoustics*, CRC Press, 2016.

[19] ISO 3382-1 “Acoustics – Measurement of room acoustic parameters – Part1: Performance spaces,” 2009.

[20] P. Larm and V. Hongisto, “Experimental comparison between speech transmission index, rapid speech transmission index, and speech intelligibility index,” *J. Acoust. Soc. Am.*, vol. 119, no. 2, pp.1106-1117, 2006.

[21] ISO 10140 “Acoustics – Laboratory measurement of sound insulation of building elements,” 2021.

[22] ISO 16283 “Acoustics – Field measurement of sound insulation in buildings and of building elements,” 2020.

ALKU Journal of Science 2025, Sayı 7(1): 15-24
e-ISSN: 2667-7814

Original Article

Eosin-Y Hassaslaştırılmış $Ba_2P_2O_7$ Katalizörlüğünde Sudan Fotokatalitik Hidrojen Üretimi

Gizem Yıldız[1*]
[1] *Biyokimya, Selçuk Üniversitesi, Konya, Türkiye*
[*] *gizemyanalak@gmail.com*

Özet

Bu çalışmada, Baryum pirofosfat ($Ba_2P_2O_7$) katalizörü Eosin-Y (EY) boyar maddesi ile hassaslaştırılarak sudan fotokatalitik hidrojen (H_2) üretimindeki aktivitesi incelenmiştir. Burada $Ba_2P_2O_7$ katalizörü, trietanolamin (TEOA) elektron vericisi varlığında ve görünür bölge ışığı altında 2.23 mmol g^{-1} H_2 üretimi göstermiştir. Bununla birlikte sistemin hidrojen üretim aktivitesini arttırmak için ortama kloroplatinik asit (H_2PtCl_6) ilave edildiğinde reaksiyon ortamında katalizör yüzeyinde fotodepozisyon yoluyla Pt yardımcı katalizörü oluşarak 8 saatte 18.47 mmol g^{-1} hidrojen üretim aktivitesine ulaşılmıştır. Bu sonuçlar, uyarılmış EY molekülleri ile $Ba_2P_2O_7$ arasında verimli elektron transferinin sağlandığını göstermektedir. EY'nin $Ba_2P_2O_7$ katalizörü üzerindeki adsorpsiyonu ile görünür bölge ışığı karşısında daha fazla fotouyarılmış elektronlar oluşturarak hidrojen aktivitesini teşvik etmektedir. Ayrıca Pt yardımcı katalizörü, fotouyarılmış yük ayrım verimini arttırarak hidrojen üretimini desteklemektedir.

Anahtar Kelimeler: Fotokataliz, hidrojen üretimi, $Ba_2P_2O_7$, Eosin-Y

Photocatalytic Hydrogen Production from Water Catalyzed by Eosin-Y Sensitized $Ba_2P_2O_7$

Abstract

In this study, the barium pyrophosphate ($Ba_2P_2O_7$) catalyst was sensitized with Eosin-Y (EY) dye, and its photocatalytic hydrogen (H_2) production activity was investigated from water. Here, the $Ba_2P_2O_7$ catalyst showed 2.23 mmol g^{-1} hydrogen production in the presence of triethanolamine (TEOA) electron donor and under visible light. However, when chloroplatinic acid (H_2PtCl_6) was added into the medium to increase the hydrogen production activity of the system, Pt, as a co-catalyst, was through photodeposition on the catalyst surface, and 18.47 mmol g^{-1} hydrogen activity was reached in 8 hours. These results show that efficient electron transfer is achieved between excited EY molecules and $Ba_2P_2O_7$. The adsorption of EY on the $Ba_2P_2O_7$ catalyst promotes hydrogen activity by creating more photoexcited electrons in response to visible light. Additionally, Pt co-catalyst supports hydrogen production by increasing the photoexcited charge separation efficiency.

Keywords: Photocatalysis, hydrogen evolution, $Ba_2P_2O_7$, Eosin-Y

Geliş/Received: 17 Mayıs/May 2024
Kabul Ediliş/Accepted: 23 Aralık/December 2024

1. GİRİŞ

Teknolojinin gelişmesiyle birlikte, dünyada küresel nüfus artışı yaşam standardının yükselmesine neden olmakta ve ülkelerin hızlı büyüme çabaları nedeniyle enerjiye olan talebi her geçen gün arttırmaktadır. Artan bu talep, mevcut kullanılan enerji kaynaklarının hızla tükenmesine neden olmakta ve ülkelerin enerji kaynaklarında dışa bağımlı olması gibi sorunları da beraberinde getirmektedir. Ayrıca, fosil yakıtların kullanımı, karbon monoksit (CO), karbondioksit (CO_2), azot monoksit (NO), azot dioksit (NO_2) gibi bazı sera gazlarının konsantrasyonunu yükseltmekte ve bu durum da önümüzdeki yüzyılda dünyanın 1-5°C ısınmasıyla ilgili endişelere yol açmaktadır [1]. Diğer yandan, güneş, jeotermal, biyokütle, rüzgar ve hidroenerji gibi fosil yakıtlara alternatif olarak sunulan yenilenebilir enerji kaynakları 1965 yılından beri kullanılmaktadır [2]. Burada güneş enerjisi, artan enerji talebini karşılamak için önde gelen bol, güvenli, temiz bir enerji kaynağı olarak kabul görmektedir. Güneş enerjisi kullanılarak yılda ~3×10^{24} J'lük bir enerji sağlanabilmektedir ve bu enerji değeri mevcut enerji ihtiyacından yaklaşık olarak 12.000 kat daha fazladır [3]. Bu nedenle, güneş enerjisi gelecekte sürdürülebilir bir enerji kaynağı olarak görülmektedir. Bugüne kadar, enerji taşıyıcısı olarak kabul gören hidrojen üretimi de güneş enerjisi yardımıyla üretildiğinde enerji krizini çözmek için geleneksel fosil yakıtların yerine geçebilecek, umut vaat eden bir teknik olarak kabul görmektedir.

1972'de Honda ve Fujishima tarafından gerçekleştirilen güneş ışığı yardımıyla fotoelektrokimyasal hidrojen (H_2) üretimine ilişkin yapılan ilk çalışmadan bu yana, fotokimyasal reaksiyonlarla suyun ayrıştırılmasından elde edilen H_2 üretimi, hem endüstriyel hem de akademik alanlarda oldukça ilgi toplayan bir alan haline gelmiştir [4]. Yapay fotosentez olarak da adlandırılan reaksiyon mekanizmasına bağlı olarak güneş ışığı yardımıyla fotokimyasal H_2 üretimi, (i) fotokatalitik (PC), (ii) fotoelektrokatalitik (PEC) ve (iii) fotovoltaik-elektrokatalitik (PV-EC) sistemler olmak üzere üç şekilde incelenebilir. Her sistemde de ışıkla uyarılmanın yanı sıra PEC sistemlerde, fotouyarılmış elektron-boşluk çiftinin tekrar birleşmesini (rekombinasyonunu) önlemek amacıyla ortamda bir membran ile ayrılan iki bölmede yer alan elektrot yüzeylerinde fotokatalizörler kullanılır ve sistem diğerlerine nazaran daha karmaşık olmaktadır [5]. PV-PEC sistemlerde ise, PEC sistemlerine kıyasla hidrojen üretimi için avantajlı olmakla birlikte maliyeti oldukça yüksektir. PC sistemlerde de, fotokatalizör çözelti ortamında dağılır ve bu nedenle fotouyarılmış yüklerin transfer yolu, diğer sistemlerdeki normal yük toplayıcılardan (bazen onlarca metre) önemli ölçüde daha kısa olmaktadır (birkaç mikrometre) [6]. Burada güneş ışığı yardımıyla elde edilen sudan fotokatalitik hidrojen üretimi, temiz enerji üretimindeki potansiyel uygulamaları nedeniyle büyük ilgi görmektedir. Sistem içerisinde kullanılan foto/katalizörlerin çoğu, uygun olmayan band aralığına sahip olması sebebiyle güneş ışığıyla uyarılma sonrası oluşan fotouyarılmış elektron-boşluk çiftlerinin rekombinasyona uğraması ile karşı karşıyadır. Bu dezavantajı önlemek için literatürde araştırmacılar, boyar madde ile hassaslaştırma [7], yüzey modifikasyonu [8], soy metal/metal katkılama [9, 10] veya yardımcı katalizör kullanımı [11] gibi verimli foto/katalizörlerin tasarımında çeşitli teknikler kullanmışlardır.

Son zamanlarda çevre dostu olması, kimyasal kararlılık ve yüksek verimlilik gibi avantajlara sahip pirofosfat tabanlı fosfor malzemeleri, bilim adamlarının oldukça dikkatini çekmektedir [12, 13]. Çeşitli formülasyon ve farklı stokiyometrilerde bulunabilen toprak alkali fosfatlar grubunda yer alan bu malzemeler, lityum bataryalar [14, 15], LED ışıklar [16], katalitik performans [17] gibi birçok alanda incelenmiştir. Ayrıca literatürde, lantanit katkılı pirofosfat yapıları ile uzun ömürlü fosforesans, güçlü mavi emisyon ve yakın kızılötesi bantta emisyon gibi kayda değer özelliklere sahip olduğu raporlanmıştır [18, 19]. Wulan ve ekibi tarafından gerçekleştirilen bir çalışmada amorf yapıdaki nikel pirofosfat (a-$Ni_2P_2O_7$) katalizörü, grafitik karbon nitrür (g-C_3N_4) ile modifiye edilerek hidrojen üretiminde incelenmiştir. TEOA electron vericisi varlığında elde edilen hidrojen üretim aktivitesi (207 μmol h^{-1} g^{-1}), c-$Ni_2P_2O_7$/g-C_3N_4 ve yalın g-C_3N_4'e göre sırasıyla 5 ve 37 kat daha yüksek olduğu raporlanmıştır [20]. Gao ve arkadaşları, $Cd_{0.5}Zn_{0.5}S$ modifiye edilmiş kobalt pirofosfat ($Cd_{0.5}Zn_{0.5}S$/CoPPi-M) hibrit fotokatalizörünü Na_2S/Na_2SO_3 elektron verici ortamında incelemişler ve CoPPi-M yapısını yardımcı katalizör görevinde kullanmışlardır. Elde edilen bulgularda sentezlenen hibrit yapının görünür bölge ışığı karşısında 6.87 mmol $g^{-1}h^{-1}$ hidrojen ürettiği bildirilmiştir. CoPPi-M ile $Cd_{0.5}Zn_{0.5}S$ arasındaki güçlü etkileşimin, fotokatalitik H_2 üretimini desteklemede belirgin bir rol oynayan etkin yük ayrımını sağladığı ve ayrıca CoPPi-M yardımcı katalizörünün $Cd_{0.5}Zn_{0.5}S$/CoPPi-M'nin yüzey hidrofilikliğini iyileştirmekle birlikte aynı zamanda kompozit fotokatalizörün aktif bölgelerin sayısını da arttırdığı belirtilmiştir [21]. Bu çalışmada ise, ticari $Ba_2P_2O_7$ yarı iletkeni katalizör görevinde fotokatalitik hidrojen üretiminde ilk kez incelenmiştir. EY boyar maddesi ile $Ba_2P_2O_7$ katalizörü hassaslaştırılarak TEOA elektron verici ortamında incelenmiştir. Çalışmalar Pt yardımcı katalizörü varlığında/yokluğunda 8 saatlik görünür bölge ışığı karşısında uyarıldığında, H_2 üretim aktiviteleri sırasıyla 18.47 mmolg^{-1} ve 2.23 mmol g^{-1} olarak raporlanmıştır. Burada artan hidrojen üretim aktivitesi EY'nin $Ba_2P_2O_7$ katalizörü üzerindeki adsorpsiyonu ile görünür bölge ışığı karşısında daha fazla fotouyarılmış elektronlar oluşturarak aktiviteyi arttırması ve Pt yardımcı katalizörünün de, fotouyarılmış yük ayrım verimini arttırarak hidrojen üretimini desteklemesine atfedilmektedir.

2. DENEYSEL ÇALIŞMALAR

Fotokatalitik hidrojen üretim çalışmalarında ticari $Ba_2P_2O_7$, EY (>% 95), TEOA (% 98), H_2PtCl_6 Sigma-Aldrich'ten, NaOH ve HCl (% 37.5) kimyasalları Merck'ten temin edilmiş olup, tüm kimyasallar hiçbir saflaştırma ve modifikasyona tabi tutulmadan kullanılmıştır. Fotokatalitik hidrojen üretiminde tüm deneyler kuvarstan yapılmış hücrelerde gerçekleştirilmiştir. TEOA elektron verici çözeltisi laboratuvar ortamında hazırlanarak, pH ayarı NaOH ve HCl kullanılarak yapılmış, ardından çözelti içerisinden azot gazı geçirilip çözünmüş oksijeni uzaklaştırıldıktan sonra glovebox içerisine alınmıştır. Ardından $Ba_2P_2O_7$ katalizörü (10 mg) tartılarak üzerine EY (0.33 mM) ve TEOA çözeltisi (20 mL, %5) ilave edilmiştir. Hücrenin ağzı kauçuk septumla kapatılarak, çözeltinin homojen dağılımı için sonikasyon işlemi uygulanmıştır. Son olarak çözelti içerikli hücre, görünür bölge ışığı (λ> 420 nm, 300W Xe lamba) karşısına yerleştirilerek manyetik karıştırıcı varlığında reaksiyon başlatılmıştır. Her saat hücrenin üzerinden şırınga ile numune alınarak gaz kromatografisinde analiz edilmiş ve kalibrasyon grafiği yardımıyla üretilen hidrojen üretim miktarları hesaplanmıştır.

2.1 STH hesaplama

Fotokatalitik hidrojen üretim çalışmalarında oluşturulan sistemin performansı, güneş-hidrojen dönüşümlülük verimi (Solar-to-hydrogen conversion efficiency, STH) ile hesaplanabilmektedir. Kullanılan foto/katalizörlerin hidrojen üretim miktarlarından STH verimi aşağıdaki formüle göre hesaplanmıştır;

$$STH = \frac{\Delta G^{o}\ x\ R_{H^2}}{P\ x\ A} \tag{1}$$

Burada, suyun ayrışmasına dair standart serbest enerji değişimi ΔG^o, hidrojen miktarı R_{H2} (mol s^{-1}), ışık şiddeti P (mW cm^{-2}), alan ise A (cm^2) olarak belirtilmiştir.

3. SONUÇLAR VE TARTIŞMA

3.1 Karakterizasyon

Öncelikle ticari $Ba_2P_2O_7$ bileşiğinin faz yapısını ve saflığını doğrulamak amacıyla X-Işını Kırınım yöntemi (XRD) analizi gerçekleştirilmiştir [22]. Yapıda her bir fosfor atomu 6 oksijen atomuyla bağlanırken, her baryum atomu da O ile 10 bağ yapmaktadır. Şekil 1a, $Ba_2P_2O_7$ tozlarının XRD desenlerini göstermektedir. XRD sonuçları tüm kırınım tepe noktalarının düzgün ve yoğun olduğunu göstermektedir. Ayrıca yapının XRD pikleri σ-dibarium pyrophosphate fazına ait olmakla birlikte $Ba_2P_2O_7$ mikroyapısı hekzagonal kristal yapıya sahiptir (Tablo 1) [23, 24].

Tablo 1. $Ba_2P_2O_7$ yapısının hkl, FWHM, 2θ ve I/Io değerleri

Numune Adı	Düzlem (hkl)	FWHM (º)	2θ (º)	I/Io
$Ba_2P_2O_7$	(111)	0.1000	22.86	1000.00
	(002)	0.1800	25.39	143.03
	(112)	0.1200	31.76	281.77
	(300)	0.1200	33.13	181.47
	(212)	0.1600	38.90	91.92
	(221)	0.0800	40.54	93.41
	(302)	0.1000	42.06	112.19
	(113)	0.1200	43.11	60.98

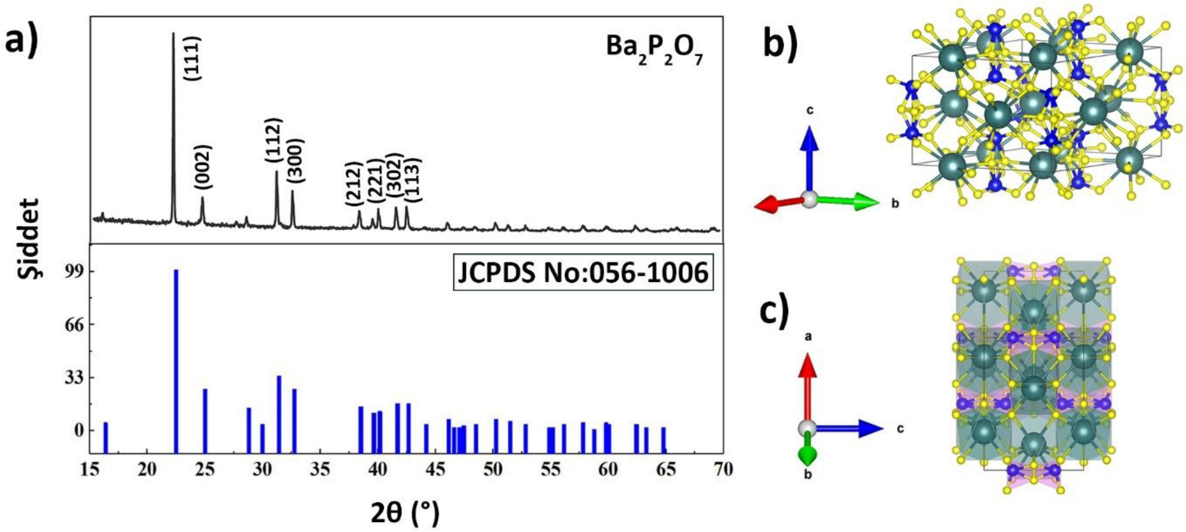

Şekil 1. $Ba_2P_2O_7$ yapısına ait a**)** XRD deseni, b**)**, c**)** 3D kristal formları

$Ba_2P_2O_7$ katalizörünün SEM görüntüleri Şekil 2'de verilmiştir. SEM görüntülerinde $Ba_2P_2O_7$ mikropartiküllerinin matris içinde büyük oranda dağıldığını göstermektedir. Burada $Ba_2P_2O_7$ mikropartikülleri kümelenme eğiliminde olduğu görülmektedir [25].

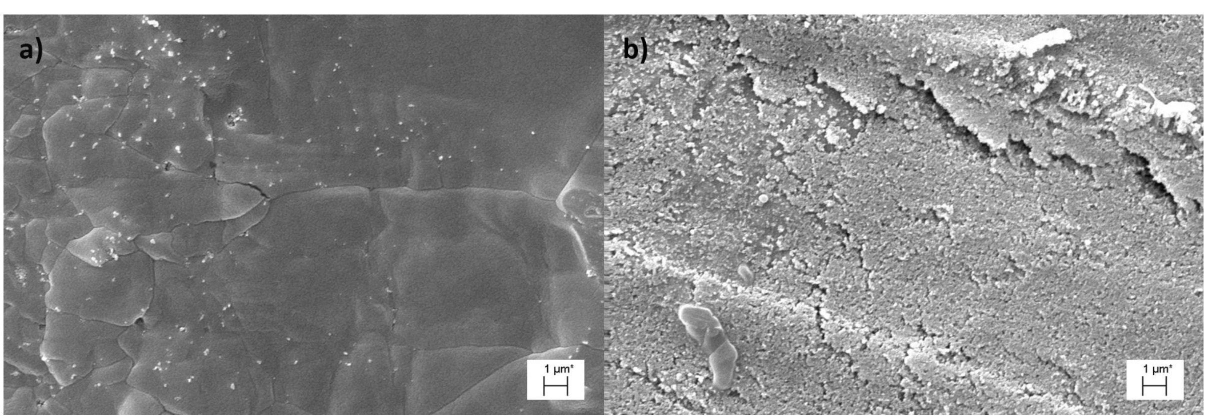

Şekil 2. $Ba_2P_2O_7$ yapısının taramalı elektron mikroskobu (SEM) görüntüleri

$Ba_2P_2O_7$ katalizörünün optik özelliklerini araştırmak için UV-Vis spektroskopisi ölçümleri gerçekleştirilmiştir. Bant aralığı enerji hesaplaması, Tauc grafiği kullanılarak gerçekleştirilmiştir ve $Ba_2P_2O_7$ bileşiği Şekil 3'te görüldüğü gibi direk enerji bant aralığına sahiptir. Grafiğin doğrusal kısmının ekstrapole edilmesiyle, saf $Ba_2P_2O_7$ yapısının bant aralığı enerjisinin 4.46 eV civarında olduğu bulunmuştur.

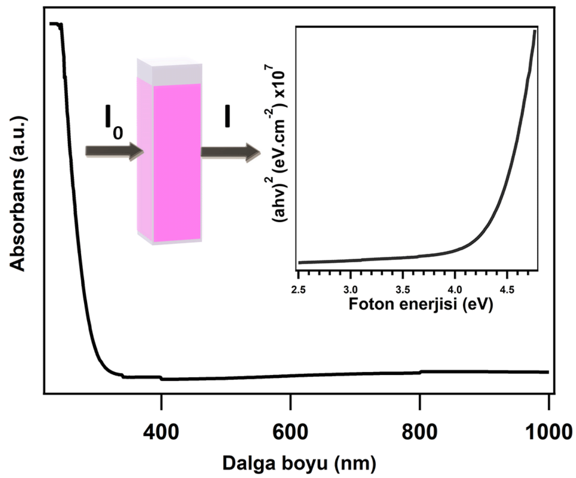

Şekil 3. $Ba_2P_2O_7$ yapısına ait UV-Vis spektrumu ve Tauc grafiği.

3.2 Fotokatalitik Hidrojen Üretimi

Fotokatalitik H_2 üretim deneylerinde ticari $Ba_2P_2O_7$ katalizörü, Eosin-Y (EY) boyar maddesi ve TEOA elektron vericisi varlığında incelenmiş, çalışmalar görünür bölge ışığı karşısında (λ>420 nm) Şekil 4a'da gösterildiği gibi gerçekleştirilmiştir. EY boyar maddesi ve TEOA elekron vericisi yokluğunda ve yalnız $Ba_2P_2O_7$ katalizörü varlığında hidrojen üretimi gözlenmemiştir. Öncelikle TEOA elektron verici çözeltisi önceki çalışmalarımızda elde edilen optimum pH 9'da hazırlanarak çalışılmıştır [26-28]. Sistemde pH 9'dan daha düşük pH değerlerinde çözeltinin hazırlanması durumunda TEOA elektron vericisi çözelti içerisinde protonlanarak etkinliğini yitirmektedir. Daha yüksek pH değerlerinde çalışıldığında ise ortamdaki protonların azalmasına bağlı olarak hidrojen üretiminde azalma görülmektedir [29]. pH ayarlanmasının ardından EY boyar maddesi ile hassaslaştırılmış $Ba_2P_2O_7$ katalizörü TEOA çözelti ortamında görünür bölge ışığı (λ>420 nm) karşısında çalışılmıştır. EY/$Ba_2P_2O_7$ katalizörlüğündeki fotokatalitik hidrojen üretim reaksiyonu (HER) çalışmaları, 8 saatlik uyarılma sonrasında 2.23 mmol g^{-1} olarak belirlenirken; Pt yardımcı katalizörü varlığında 8 saatte 18.47 mmolg^{-1} hidrojen üretimi gözlenmiştir. EY/$Ba_2P_2O_7$-Pt katalizörlüğünde elde edilen yüksek hidrojen üretim aktivitesi, yük ayrımını büyük miktarda hızlandıran ve fotodepozisyon sonucu oluşan Pt^0 türünün varlığına atfedile bilinir [30]. Ayrıca Tablo 2'de verilen fotokatalitik hidrojen üretim sonuçları, yardımcı katalizör varlığında ve yokluğunda karşılaştırıldığında, Eşitlik 2.4'e göre hesaplanan STH verimleri, hidrojen üretim sonuçlarıyla paralel elde edilmiştir.

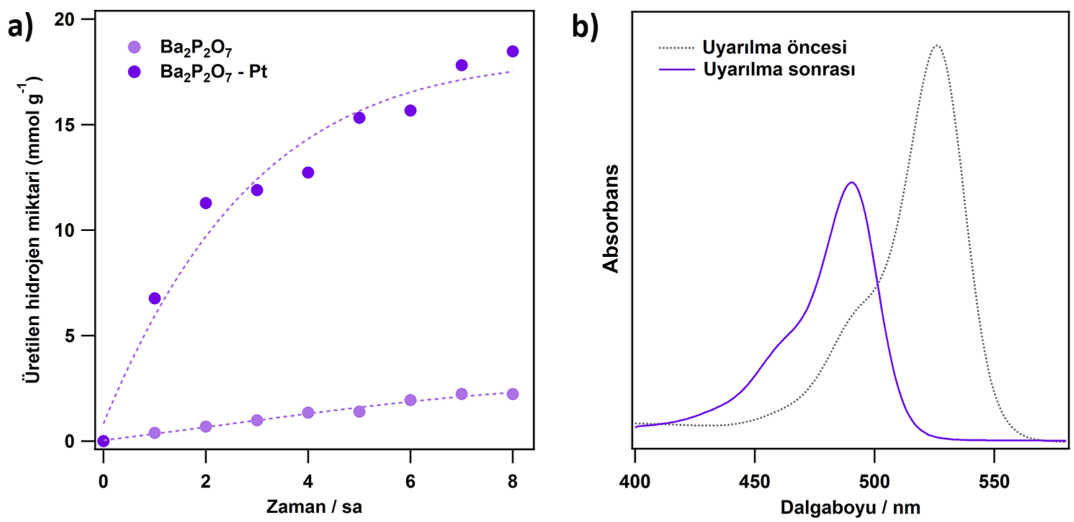

Şekil 4. a) EY boyar maddesi ile hassaslaştırılmış $Ba_2P_2O_7$ katalizörlüğünde Pt yardımcı katalizörü varlığında ve yokluğunda elde edilen fotokatalitik H_2 üretim sonuçları, b) $Ba_2P_2O_7$ katalizörü varlığında EY boyar maddesinin uyarılma öncesi ve sonrası UV grafikleri

Ayrıca Şekil 4b'de EY hassaslaştırılmış $Ba_2P_2O_7$ katalizörünün görünür bölge ışığı ile uyarılma öncesi/sonrası UV-Vis absorbans sonuçları incelenmiştir. Burada oluşturulan sistemin kararlılığı, boyar maddenin konsantrasyonu ile ilişkilidir. 8 saatlik görünür bölge ışığı ile uyarılma öncesi ve sonrasında EY boyar maddesinin UV-Vis spektrumları mukayese edildiğinde, 520 nm'deki EY'nin absorbans piki uyarılma sonrasında 490 nm'ye kaydığı görülmüştür. Gözlenen maviye kayma (hipsokromik etki) durumu, EY boyar maddesinin yapısında bulunan brom gruplarının molekülden ayrılarak floresein bir yapıya dönüşmesine atfedilebilir [30, 32].

Tablo 2. EY hassaslaştırılmış $Ba_2P_2O_7$ ve $Ba_2P_2O_7$/Pt katalizörlerinin H_2 üretim miktarları ve STH hesaplamaları

Katalizör	Üretilen H_2 miktarı (mmol g^{-1})		STH verimi (%)
	1 sa	8 sa	
$Ba_2P_2O_7$	0.28	2.23	0.72
$Ba_2P_2O_7$/Pt	2.31	18.47	5.96

3.3 Mekanizma

Görünür bölge ışığı karşısında EY hassaslaştırılmış $Ba_2P_2O_7$ katalizörü sudan fotokatalitik hidrojen üretim mekanizması incelendiğinde (Şekil 5), EY boyar maddesi üzerine gönderilen ışınları absorplayarak HOMO seviyesinde fotouyarılmış elektron (e^-) ve boşlukları (h^+) oluşturur. Ardından fotouyarılmış e^-'lar LUMO seviyesine aktarılır ve oradan da adsorplanan $Ba_2P_2O_7$ katalizörünün iletkenlik bandına (İB) aktarılır. Burada, EY boyar maddesi uyarılma sonrasında EY^{1*} geçiş durumunu oluşturur, ardından sistemler arası geçiş (ISC, inter system crossing) ile üçlü uyarılmış durum olarak EY^{3*} üretilir. Son olarak EY^{3*}, elektron verici olarak kullanılan TEOA tarafından $EY^{-\bullet}$'yi meydana getirerek reaksiyonun sirkülasyonu sağlanır [33, 34]. $Ba_2P_2O_7$ katalizörünün İB bandına aktarılan fotouyarılmış e^-'lar ise Pt yardımcı katalizörünün yüzeyine göç ederek çözelti ortamındaki protonlarla reaksiyona girerek hidrojen üretimini gerçekleştirmektedirler. Pt yardımcı katalizörünün eklenmesi, EY/$Ba_2P_2O_7$'tan aktarılan fotouyarılmış yük taşıyıcılarının transfer verimliliğini arttırmasının yanı sıra yüklerin ayrılmasını da desteklemiştir [35]. Sistemin hidrojen üretim süreci ise aşağıdaki (2-7) reaksiyonlarla açıklanabilir:

$$EY + h\nu \rightarrow EY^{*} \quad (2)$$

$$EY^{*} + Ba_2P_2O_7 \rightarrow (EY^{+} + e_{LUMO}^{-}) + Ba_2P_2O_7^{*} \quad (3)$$

$$(EY^{+} + e_{LUMO}^{-}) + Ba_2P_2O_7^{*} \rightarrow EY^{+} + Ba_2P_2O_7^{*}(e_{İB}^{-}) \quad (4)$$

$$Ba_2P_2O_7^{*}(e_{İB}^{-}) + Pt \rightarrow Ba_2P_2O_7^{+} + Pt^{*}(e_{İB}^{-}) \quad (5)$$

$$Pt^{*}(e_{İB}^{-}) + H_2O \rightarrow \tfrac{1}{2} H_2 + HO^{-} + Pt^{+} \quad (6)$$

$$EY^{+} + TEOA \rightarrow EY + TEOA^{+} \quad (7)$$

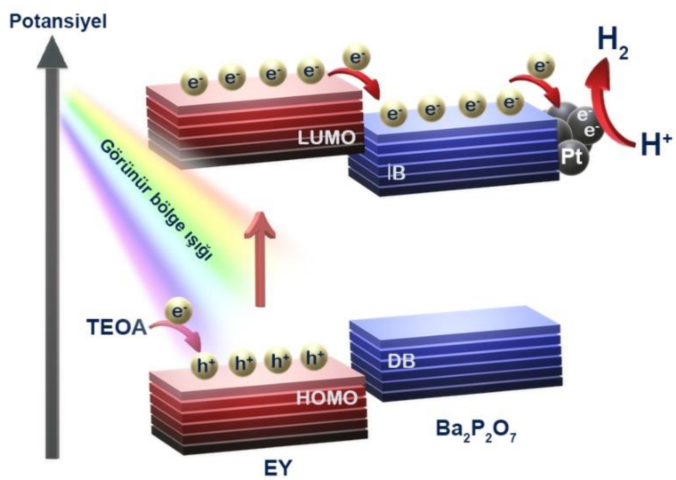

Şekil 5. $Ba_2P_2O_7$-Pt katalizörü, TEOA elektron vericisi (pH9) ve EY boyar maddesi varlığında önerilen sudan fotokatalitik hidrojen üretiminin mekanizması

4. SONUÇ

Yapılan bu çalışmada, ticari $Ba_2P_2O_7$ katalizörü EY boyar maddesi ile hassaslaştırılarak Pt yardımcı katalizörü varlığında fotokatalitik H_2 üretim aktivitesi incelenmiştir. $Ba_2P_2O_7$ katalizörünün yapısı SEM ve XRD çalışmaları ile yapısı aydınlatılmıştır. Elde edilen EY/$Ba_2P_2O_7$-Pt katalizörünün fotokatalitik suyun ayrıştırma yoluyla hidrojen üretimi için TEOA elektron verici ortamında 8 saatlik görünür ışık altında aktivitesi incelenmiştir. Pt yardımcı katalizörü varlığında en yüksek hidrojen oluşumu 18.47 mmol g^{-1} ve %5.96 STH verimi olarak raporlanmıştır. Burada elde edilen hidrojen üretim miktarı Pt yardımcı katalizörü varlığında yalın haldeki $Ba_2P_2O_7$ katalizörüne oranla yaklaşık 8.3 kat daha fazla olduğu gözlenmiştir. Bu durum $Ba_2P_2O_7$ yarı iletkeni ile Pt arasındaki etkileşimin daha kuvvetli olmasından kaynaklı olup, fotouyarılmış elektronların yarı iletkenden yardımcı katalizöre daha iyi elektron transferi sağlamasına atfedilmektedir. Özetle, yüksek aktiviteye sahip fotokatalizörlerin oluşturulmasında $Ba_2P_2O_7$ yanında Pt etkin bir şekilde rol oynamakla birlikte EY boyar maddesi, geniş bant aralıklı olan $Ba_2P_2O_7$ katalizörünün görünür bölge ışığı altındaki absorbsiyon yeteneğini geliştirmiştir. Bu çalışma ile $Ba_2P_2O_7$ tabanlı katalizörlerin fotokatalitik çalışmalarda malzeme tasarımı ve uygulama yönünden mevcut ve gelecekteki araştırmaların önünü açacağı öngörülmektedir.

5. TEŞEKKÜR BÖLÜMÜ

Değerli katkılarından dolayı ve laboratuvar cihazlarının kullanımı konusunda destekleri için Karamanoğlu Mehmetbey Üniversitesi'nden öğretim üyesi Doç. Dr. Adem SARILMAZ ve Prof. Dr. Faruk ÖZEL'e ve Selçuk Üniversitesi'nden öğretim üyesi Prof. Dr. İmren HATAY PATIR'a teşekkürlerimi sunarım.

REFERANSLAR

[1] D. J. Wuebbles and A. K. Jain, "Concerns about climate change and the role of fossil fuel use," *Fuel Processing Technology*, vol. 71, no. 1, pp. 99-119, June 2001, doi: https://doi.org/10.1016/S0378-3820(01)00139-4.

[2] S. Kılıç Depren, M. T. Kartal, N. Çoban Çelikdemir, and Ö. Depren, "Energy consumption and environmental degradation nexus: A systematic review and meta-analysis of fossil fuel and renewable energy consumption," *Ecological Informatics*, vol. 70, p. 101747, Sep 2022, doi: https://doi.org/10.1016/j.ecoinf.2022.101747.

[3] Y. Zhang *et al.*, "Photocatalytic Hydrogen Evolution via Water Splitting: A Short Review," *Catalysts*, vol. 8, no. 12, p. 655, Oct. 2018, doi: https://doi.org/10.3390/catal8120655.

[4] A. Fujishima and K. Honda, "Electrochemical photolysis of water at a semiconductor electrode," *Nature*, vol. 238, no. 5358, pp. 37-38, July 1972.

[5] W. Zhao et al., "Recent advances in photocatalytic hydrogen evolution with high-performance catalysts without precious metals," *Renewable and Sustainable Energy Reviews*, vol. 132, p. 110040, Oct. 2020, doi: https://doi.org/10.1016/j.rser.2020.110040.

[6] J. H. Kim, D. Hansora, P. Sharma, J.-W. Jang, and J. S. Lee, "Toward practical solar hydrogen production–an artificial photosynthetic leaf-to-farm challenge," *Chemical Society Reviews*, vol. 48, no. 7, pp. 1908-1971, Mar. 2019, doi: https://doi.org/10.1039/C8CS00699G

[7] Y. Sun et al., "Eosin Y-sensitized partially oxidized Ti_3C_2 MXene for photocatalytic hydrogen evolution," *Catalysis Science & Technology*, vol. 9, no. 2, pp. 310-315, Nov. 2019, doi: https://doi.org/10.1039/C8CY02240B.

[8] A. T. Montoya and E. G. Gillan, "Enhanced photocatalytic hydrogen evolution from transition-metal surface-modified TiO_2," *ACS Omega*, vol. 3, no. 3, pp. 2947-2955, Mar. 2018, doi: https://doi.org/10.1021/acsomega.7b02021.

[9] A. H. Jawhari, N. Hasan, I. A. Radini, K. Narasimharao, and M. A. Malik, "Noble Metals Deposited $LaMnO_3$ Nanocomposites for Photocatalytic H_2 Production," *Nanomaterials*, vol. 12, no. 17, p. 2985, Aug. 2022. doi: https://www.mdpi.com/2079-4991/12/17/2985.

[10] D. Wang and X.-Q. Gong, "Function-oriented design of robust metal cocatalyst for photocatalytic hydrogen evolution on metal/titania composites," *Nature Communications*, vol. 12, no. 1, p. 158, Jan. 2021, doi: https://doi.org/10.1038/s41467-020-20464-x.

[11] Q. Zhu, Z. Xu, B. Qiu, M. Xing, and J. Zhang, "Emerging Cocatalysts on g-C_3N_4 for Photocatalytic Hydrogen Evolution," *Small*, vol. 17, no. 40, p. 2101070, July 2021, doi: https://doi.org/10.1002/smll.202101070.

[12] L. Wang, M. Xu, R. Sheng, L. Liu, and D. Jia, "Microwave assisted co-precipitation synthesis and photoluminescence characterization of spherical $Sr_2P_2O_7$:Ce^{3+}, Tb^{3+} phosphors," *Journal of Alloys and Compounds*, vol. 579, pp. 343-347, Dec. 2013, doi: https://doi.org/10.1016/j.jallcom.2013.06.085.

[13] B. Wang, Q. Ren, O. Hai, and X. Wu, "Luminescence properties and energy transfer in Tb^{3+} and Eu^{3+} co-doped $Ba_2P_2O_7$ phosphors," *RSC Advances*, vol. 7, no. 25, pp. 15222-15227, Mar. 2017, doi: 10.1039/C6RA28122B.

[14] Y. Xiao, J. Lee, A. Yu, and Z. Liu, "Electrochemical Performance of Amorphous and Crystalline $Sn_2P_2O_7$ Anodes in Secondary Lithium Batteries," *Journal of the Electrochemical Society*, vol. 146, no. 10, p. 3623, 1999, doi: 10.1149/1.1392524.

[15] Y. Uebou, S. Okada, M. Egashira, and J.-I. Yamaki, "Cathode properties of pyrophosphates for rechargeable lithium batteries," *Solid State Ionics*, vol. 148, no. 3-4, pp. 323-328, June 2002, doi: https://doi.org/10.1016/S0167-2738(02)00069-3.

[16] T. Zhao, M. Yan, Y. Pu, and D. Zhu, "Preparation and luminescence properties of $Ba_2P_2O_7$:Dy^{3+}, Ce^{3+} phosphors," *Spectrochimica Acta Part A: Molecular and Biomolecular Spectroscopy*, vol. 299, p. 122874, Oct. 2023, doi: https://doi.org/10.1016/j.saa.2023.122874.

[17] X. Li et al., "Sustainable Production of 2,3-Pentanedione: Catalytic Performance of $Ba_2P_2O_7$ Doped with Cs for Vapor-Phase Condensation of Lactic Acid," *Industrial & Engineering Chemistry Research*, vol. 56, no. 49, pp. 14437-14446, Dec. 2017, doi: 10.1021/acs.iecr.7b03595.

[18] C. Rosticher, B. Viana, T. Maldiney, C. Richard, and C. Chanéac, "Persistent luminescence of Eu, Mn, Dy doped calcium phosphates for in-vivo optical imaging," *Journal of Luminescence*, vol. 170, pp. 460-466, Feb. 2016, doi: https://doi.org/10.1016/j.jlumin.2015.07.024.

[19] R. Pang, C. Li, S. Zhang, and Q. Su, "Luminescent properties of a new blue long-lasting phosphor $Ca_2P_2O_7$: Eu^{2+}, Y^{3+}," *Materials Chemistry and Physics*, vol. 113, no. 1, pp. 215-218, Jan. 2009, doi: https://doi.org/10.1016/j.matchemphys.2008.07.061.

[20] B. Wulan, S. Yi, S. Li, Y. Duan, J. Yan and Q. Jiang, "Amorphous nickel pyrophosphate modified graphitic carbon nitride: an efficient photocatalyst for hydrogen generation from water splitting," *Applied Catalysis B: Environmental*, vol. 231, 43-50, Sep. 2018, doi: https://doi.org/10.1016/j.apcatb.2018.02.045.

[21] L. Gao, C. Weng, Y. Wang, X. Lv, J. Ren, Z. Yuan, "Defect-rich cobalt pyrophosphate hybrids decorated $Cd_{0.5}Zn_{0.5}S$ for efficient photocatalytic hydrogen evolution: Defect and interface engineering," *Journal of Colloid and Interface Science*, vol. 606, 544-555, Jan. 2022, doi: https://doi.org/10.1016/j.jcis.2021.08.041.

[22] Ö. Sevgili, F. Özel, A. Ruşen, E. Yiğit, and İ. Orak, "The surface and electrical properties of the Al/$Ba_2P_2O_7$/p-Si heterojunctions in wide range of temperature and frequency," *Surfaces and Interfaces*, vol. 28, p. 101637, Feb. 2022, doi: https://doi.org/10.1016/j.surfin.2021.101637.

[23] A. A. ElBelghitti, A. Elmarzouki, A. Boukhari and E. M. Holt, "σ-Dibarium Pyrophosphate," *Acta Crystallographica Section C*, vol. C51, p. 1478-1480, Aug. 1995, doi: https://doi.org/10.1107/S0108270195001739.

[24] T. Zhao, M. Yan, Y. Pu, D. Zhu, "Preparation and luminescence properties of $Ba_2P_2O_7$:Dy^{3+}, Ce^{3+} phosphors," *Spectrochimica Acta Part A: Molecular and Biomolecular Spectroscopy*, vol. 299, Oct. 2023, doi: https://doi.org/10.1016/j.saa.2023.122874

[25] F. Ozel et al., "Production of microstructured $BaZrO_3$ and $Ba_2P_2O_7$-based polymer shields for protection against ionizing photons," *Journal of Physics and Chemistry of Solids*, vol. 158, p. 110238, Nov. 2021, doi: https://doi.org/10.1016/j.jpcs.2021.110238.

[26] G. Yanalak et al., "Ternary nanocomposites of mesoporous graphitic carbon nitride/black phosphorus/gold nanoparticles (mpg-CN/BP-Au) for photocatalytic hydrogen evolution and electrochemical sensing of paracetamol," *Applied Surface Science*, vol. 557, p. 149755, Aug. 2021, doi: https://doi.org/10.1016/j.apsusc.2021.149755.

[27] I. Sargin, G. Yanalak, G. Arslan, and I. H. Patir, "Green synthesized carbon quantum dots as TiO2 sensitizers for photocatalytic hydrogen evolution," *International Journal of Hydrogen Energy*, vol. 44, no. 39, pp. 21781-21789,Aug. 2019, doi: https://doi.org/10.1016/j.ijhydene.2019.06.168.

[28] S. Altinişik and S. Koyuncu, "A Novel Viologen-Derived Covalent Organic Framework Based Metal Free Catalyst for Nitrophenol Reduction," *ChemCatChem*, vol. 15, no. 4, Jan. 2023, https://doi.org/10.1002/cctc.202201418.

[29] M. K. Gonce et al., "Photocatalytic hydrogen evolution based on Cu_2ZnSnS_4, $Cu_2ZnSnSe_4$ and $Cu_2ZnSnSe_{4-x}S_x$ nanofibers," *RSC Advances*, vol. 5, no. 114, pp. 94025-94028, Oct. 2015, doi: https://doi.org/10.1039/C5RA18877F.

[30] J. Wu et al., "Boosting photocatalytic hydrogen evolution via regulating Pt chemical states," *Chemical Engineering Journal*, vol. 442, p. 136334, Aug. 2022, doi: https://doi.org/10.1016/j.cej.2022.136334.

[31] K. Kimura, T. Miwa, and M. Imamura, "The radiolysis and photolysis of methanolic solutions of Eosin. I. The γ-radiolysis of neutral and alkaline solutions," *Bulletin of the Chemical Society of Japan*, vol. 43, no. 5, pp. 1329-1336, May 1970, doi: https://doi.org/10.1246/bcsj.43.1329.

[32] R. Abe, K. Hara, K. Sayama, K. Domen, and H. Arakawa, "Steady hydrogen evolution from water on Eosin Y-fixed TiO_2 photocatalyst using a silane-coupling reagent under visible light irradiation," *Journal of Photochemistry and Photobiology A: Chemistry*, vol. 137, no. 1, pp. 63-69, Oct. 2000, doi: https://doi.org/10.1016/S1010-6030(00)00351-8.

[33] C. Kong, S. Min, and G. Lu, "A novel amorphous $CoSn_xO_y$ decorated graphene nanohybrid photocatalyst for highly efficient photocatalytic hydrogen evolution," *Chemical Communications*, vol. 50, no. 39, pp. 5037-5039, Mar. 2014, doi: 10.1039/C4CC00547C.

[34] C. Kong, S. Min, and G. Lu, "Robust Pt–Sn alloy decorated graphene nanohybrid cocatalyst for photocatalytic hydrogen evolution," *Chemical Communications*, vol. 50, no. 66, pp. 9281-9283, June 2014, doi: 10.1039/C4CC03711A.

[35] G. Zhou et al., "Remarkably enhanced hydrogen evolution of g-C3N4 nanosheet under simulated sunlight via AgPt alloy co-catalyst with low amount of Pt," *Journal of Cleaner Production*, vol. 434, p. 139950, Jan.2024, doi: https://doi.org/10.1016/j.jclepro.2023.139950.

ALKU Journal of Science 2025, Sayı 7(1): 25-42
e-ISSN: 2667-7814

Review Article

Review of GPS and IMU System Performance in Unmanned Aerial Vehicles (UAVs)

Muammer Erbaş[1*], Gülşah Demirhan Aydin[2]
[1] *Turkish Standards Institution, Electrotechnical Laboratory, Ankara 06170, Türkiye.*
[2] *Department of Electrical & Electronics Engineering, Baskent University, Ankara 06790, Türkiye.*
**erbasmuammer@hotmail.com*

Abstract

This paper reviews the pivotal role of Global Positioning System and Inertial Measurement Unit technologies in the navigation and control of Unmanned Aerial Vehicles. The Global Positioning System offers precise global positioning, while the Inertial Measurement Unit provides high-frequency motion and orientation data. However, Global Positioning System signal interruptions and Inertial Measurement Unit drift pose challenges, particularly in dynamic or Global Positioning system-denied environments. This review explores the integration of the Global Positioning System and low-cost Inertial Measurement Unit systems through advanced sensor fusion techniques, such as Kalman filtering and machine learning, to enhance navigation reliability. Future directions, including advancements in hardware, adaptive algorithms, and swarm navigation, are discussed to address operational challenges and unlock the potential of Unmanned Aerial Vehicles in diverse applications.

Keywords: UAVs, GPS, MEMS-based IMU, sensor fusion, positioning accuracy, system performance, navigation

İnsansız Hava Araçlarında (İHA) GPS ve IMU Sistem Performansının İncelenmesi

Özet

Bu makale, İnsansız Hava Araçlarının navigasyon ve kontrolünde Küresel Konumlama Sistemi ve Ataletsel Ölçüm Birimi teknolojilerinin kritik rolünü incelemektedir. Küresel Konumlama Sistemi, hassas küresel konumlama sağlarken, Ataletsel Ölçüm Birimi yüksek frekanslı hareket ve yönelim verileri sunar. Ancak, Küresel Konumlama Sistemi sinyal kesintileri ve Ataletsel Ölçüm Birimi kayması, özellikle dinamik görevlerde veya Küresel Konumlama Sistemi erişiminin olmadığı ortamlarda zorluklar yaratmaktadır. Bu inceleme, navigasyon güvenilirliğini artırmak için Kalman filtresi ve makine öğrenimi gibi ileri seviye sensör füzyon teknikleri kullanılarak Küresel Konumlama Sistemi ve düşük maliyetli Ataletsel Ölçüm Birimi sistemlerinin entegrasyonunu ele almaktadır. Çalışmada ayrıca donanım gelişmeleri, uyarlanabilir algoritmalar ve sürü navigasyonu gibi gelecekteki yönelimler ele alınarak operasyonel zorlukların üstesinden gelinmesi ve İnsansız Hava Araçlarının çeşitli uygulamalardaki potansiyelinin açığa çıkarılması hedeflenmektedir.

Anahtar Kelimeler: İnsansız hava araçları, GPS, MEMS tabanlı IMU, sensör füzyonu, konum doğruluğu, sistem performansı, navigasyon

Geliş/Received: 29 Ocak/January 2025
Kabul Ediliş/Accepted: 7 Nisan/April 2025

1. INTRODUCTION

Unmanned Aerial Vehicles (UAVs) are utilized in diverse fields such as military, agriculture, logistics, surveillance, and disaster management, where precise navigation and stable orientation control are essential. For UAVs to operate effectively, they rely heavily on accurate positioning and orientation data. This is achieved by integrating a Global Positioning System (GPS) and an Inertial Measurement Unit (IMU), each serving a complementary role in tracking a UAV's position and orientation [1, 2].

However, GPS performance is often hindered by environmental factors, such as signal multipath and satellite obstructions, which can lead to latency or inaccuracies [3]. On the other hand, the IMU system provides high-frequency orientation and motion data but is susceptible to long-term drift, which degrades positional accuracy over time [4]. To address these challenges, sensor fusion techniques have emerged as a popular approach for integrating GPS and IMU data, allowing UAVs to leverage the strengths of each system while mitigating their respective weaknesses [5].

To establish a strong foundation for this study, a thorough literature review was conducted using various academic platforms (e.g., Google Scholar, Web of Science, ScholarOne, ScienceDirect) to analyze existing research on GPS and IMU systems in UAVs. A total of 67 sources, including books and articles, were examined, out of which 42 were deemed relevant and cited in this paper. This review focuses on identifying key methodologies, advancements, and issues related to the integration of GPS and IMU systems and their performance enhancement. By examining various studies, the paper aims to provide a comprehensive understanding of current trends and future research directions in GPS/IMU sensor fusion. The key terms associated with this study include but are not limited to, UAV navigation, GPS accuracy, GPS spoofing, IMU drift, GPS advantages, IMU sensor advantages, sensor fusion, Kalman Filter, machine learning approaches in UAV navigation, and positioning algorithms.

This paper provides a detailed analysis of the GPS and IMU systems used in UAVs, examining the individual characteristics of each system, their benefits, limitations, and the potential of sensor fusion to enhance UAV performance. This review paper is structured as follows: section 2 provides a technical background about GPS and IMU systems in UAVs, section 3 presents an integration of GPS and IMU systems, section 4 explores sensor fusion techniques in UAVs, section 5 discusses open challenges in GPS/IMU integration, section 6 highlights future directions, and section 7 gives concluding points about the topic.

2. TECHNICAL BACKGROUND: GPS AND IMU SYSTEMS IN UAVS

2.1 Overview of GPS and IMU Systems in UAVs

UAVs rely heavily on GPS and IMU systems for accurate navigation, stability, and control. Each system contributes uniquely.

GPS provides absolute positional data by triangulating signals from satellites, offering global coverage and high accuracy, especially in open environments. Its precision can be further enhanced by techniques like Real-Time Kinematic (RTK) positioning and Differential GPS (DGPS). However, its performance is hindered by environmental factors such as multipath errors, signal obstructions, and susceptibility to jamming and spoofing, which can compromise its reliability.

IMU measures orientation, velocity, and acceleration through sensors like accelerometers and gyroscopes, providing high-frequency data essential for motion tracking. While it offers valuable measurements, it faces challenges such as drift over time and sensitivity to environmental noise, which can affect accuracy over extended periods.

Figure 1 illustrates the complementary roles of GPS and IMU in UAV navigation, highlighting their combined strengths.

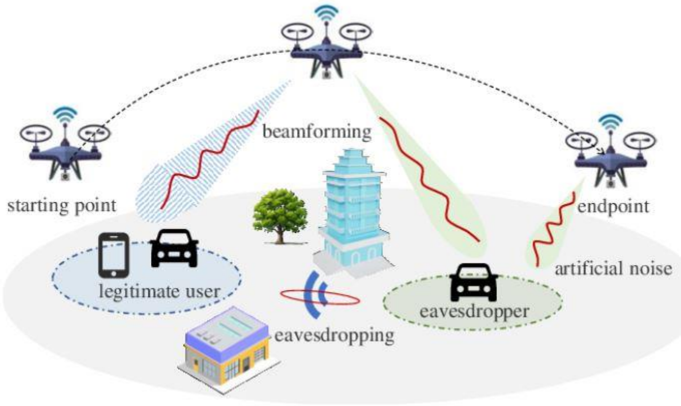

Figure 1. UAV-enabled secure communication networks [6]

This section provides a detailed exploration of the features, advantages, and limitations of GPS and IMU technologies as applied to UAVs, supported by recent studies and technical resources.

GPS technology for UAVs relies on a constellation of satellites that transmit signals to GPS receivers on the UAV. These receivers calculate their position by measuring the time delay from multiple satellite signals and triangulating their location. This system plays a critical role in ensuring reliable and precise navigation for UAVs. GPS enables real-time positioning, allowing UAVs to determine their exact coordinates, which is essential for navigation and following predefined flight paths [7]. Its global coverage ensures accessibility in diverse and remote environments where terrestrial navigation may not be available [8]. Additionally, GPS data helps determine both altitude and speed, which are critical for stable flight control. This is particularly valuable in applications that demand accurate altitude management, like surveying or mapping [7, 9].

Advanced GPS options such as DGPS and RTK positioning enhance precision by providing real-time corrections. These methods are particularly valuable in operations where even small positioning errors could impact results, such as aerial inspections and precision agriculture [7-9]. The integration of GPS in UAVs provides a wide array of benefits, making it an indispensable tool for both commercial and research applications. These advantages significantly enhance the performance and usability of UAVs in various fields such as agriculture, surveying, infrastructure inspection, and environmental monitoring.GPS also contributes to enhanced autonomy, enabling UAVs to follow predefined flight paths independently with high accuracy and efficiency. This capability is especially useful in applications like land surveying, precision agriculture, and infrastructure assessment, where repeated and precise flights are necessary. Autonomous navigation reduces the need for manual intervention and increases the potential for large-scale data collection [10, 11].

Another key advantage of GPS is cost efficiency. GPS receivers are relatively affordable and can be integrated into small UAV systems without significantly increasing the overall cost. This makes GPS a cost-effective solution for UAVs, particularly for commercial applications where minimizing operational costs is a priority. With the availability of low-cost GPS receivers that provide accurate positioning, UAV systems can deliver precise navigation without the need for expensive alternatives like ground-based systems [10, 12]. Finally, GPS enables real-time monitoring and control, allowing UAV operators to continuously track the UAV's location, which is essential for mission control and safety. This capability is crucial in applications where continuous monitoring of UAVs is required, such as in disaster response scenarios or during long-distance flights. The real-time data allows for in-flight adjustments, ensuring the UAV stays on course and responds to dynamic environmental conditions or unexpected obstacles, thus enhancing mission safety and success [10, 11].

Despite its widespread use and critical role in UAV navigation, GPS technology has certain limitations that can impact UAV performance, particularly under specific environmental and operational conditions. One such limitation is signal interference and multipath errors, where GPS signals can be blocked, reflected, or attenuated by obstacles like buildings, trees, and mountains. These multipath errors can reduce GPS accuracy, especially in urban or forested areas where signal reflections may mislead the receiver. In these environments, UAVs can experience significant positioning errors due to these distorted signals [11].

Another limitation arises from low accuracy in dynamic conditions, where rapid movement during high-speed UAV flight can introduce errors in GPS measurements due to Doppler shifts. Furthermore, GPS receivers may struggle to update positions quickly enough, leading to inaccuracies. This issue is particularly noticeable in fast-moving UAVs, such as those used in aerial photography or surveying, where precise real-time positioning is critical. Additionally, environmental factors like ionospheric and tropospheric delays can interfere with GPS signal transmission, reducing the accuracy and reliability of GPS readings. These atmospheric effects are especially relevant for UAVs operating at high altitudes or in extreme weather conditions, where signal degradation may occur more frequently.

GPS performance is also dependent on the availability and visibility of satellite constellations. In regions with limited satellite visibility, such as polar areas or dense urban landscapes, GPS performance can degrade significantly, leading to less reliable positioning data for UAVs operating in these challenging environments. Lastly, GPS signals are vulnerable to intentional jamming and spoofing, which poses a significant security risk for UAV operations, especially in applications requiring high reliability, such as military or critical commercial operations. The risk of signal interference can jeopardize mission success and UAV safety in sensitive or hostile environments [11, 13]. Figure 2 illustrates a spoofing scenario.

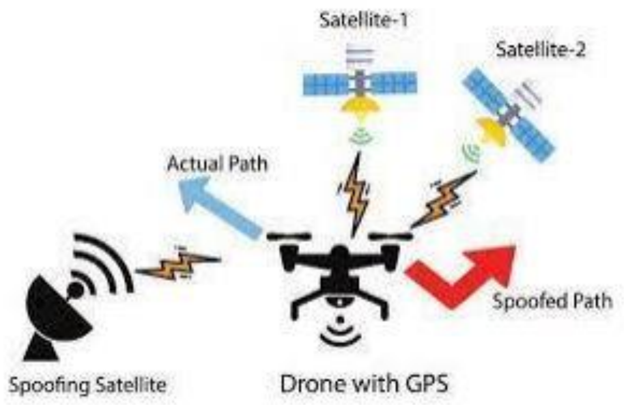

Figure 2. Spoofer tries to deviate UAV from the main trajectory [14]

To mitigate some of the limitations of GPS, various enhancements and complementary technologies are being employed in UAVs to improve accuracy and reliability, especially in challenging environments. These advancements help address the issues of signal interference, multipath errors, and limited accuracy. One such enhancement is RTK GPS, which improves the precision of GPS data by using ground-based reference stations to provide real-time corrections. This method achieves centimeter-level accuracy, making it crucial for precision tasks such as surveying and agriculture, where high positional accuracy is paramount. RTK GPS has become a standard for tasks that require extreme precision, as it can correct errors in real-time, reducing the dependency on satellite visibility [15].

Another approach is DGPS, which enhances GPS accuracy by using ground stations that transmit correction signals. DGPS is widely used in applications where sub-meter accuracy is required. By correcting signal errors and reducing positional drift, DGPS ensures that UAVs can maintain accurate positioning even over long-duration flights. This technology has been applied in fields such as precision farming and infrastructure inspection, where minor positional errors can lead to significant operational consequences. Additionally, UAVs sometimes use augmented GPS systems such as Wide Area Augmentation System (WAAS) or European Geostationary Navigation Overlay Service (EGNOS) to enhance the accuracy, integrity, and availability of GPS signals. These systems provide corrections that improve GPS performance, particularly in regions with limited satellite coverage. By reducing the impact of atmospheric and signal-related errors, these augmentation systems make GPS navigation more reliable in remote or challenging environments [8].

GPS technology plays a critical role in UAV performance, providing essential data for autonomous navigation and real-time location tracking. Despite its limitations, particularly in terms of signal reliability and susceptibility to environmental interference, advancements in GPS technology—coupled with the integration of systems like IMUs—are enhancing UAV capabilities across a broad spectrum of applications. Future improvements in GPS technology, along with the development of robust sensor fusion methods, are expected to further expand the operational effectiveness of UAVs in complex environments [3,8].

IMU systems are crucial in UAVs for ensuring stable navigation, orientation, and flight control. By providing real-time data on acceleration and angular velocity, IMUs enable UAVs to maintain stability and correct for disturbances autonomously. MEMS, which stands for Micro Electromechanical Systems, enables the integration of microelectronic circuits and mechanical structures on a single chip, facilitating monolithic integration. This technology has revolutionized sensor design, making it possible to sense the physical and chemical aspects of the external environment with high precision. Over recent decades, MEMS has become a leading choice in sensor development, particularly for applications in UAVs, where IMU sensors play a critical role. MEMS-based IMUs offer several advantages over traditional sensors, including smaller size and lower cost, enhanced sensitivity, and the ability to be batch-fabricated on wafers with integrated circuits. These attributes make MEMS ideal for UAV applications, where weight, space, and power efficiency are crucial, allowing for improved navigation, control, and stability [16, 17].

An IMU is a sensor module that measures an object's velocity, orientation, and gravitational forces. Most UAV IMUs consist of an accelerometer, a gyroscope, and sometimes a magnetometer. Each component of the IMU contributes uniquely to flight control and stability, which are mentioned below in detail; respectively.

An accelerometer in a UAV's IMU measures linear acceleration across three axes (x, y, and z). It detects the rate of velocity change due to forces such as gravity, allowing the UAV to assess tilt, altitude shifts, and motion. This data is critical for stabilizing the UAV, particularly when hovering or performing controlled maneuvers. MEMS (Micro-Electro-Mechanical Systems) technology is commonly used in UAV accelerometers due to its small size, low weight, and high sensitivity, which is ideal for compact UAV designs. By continuously analyzing acceleration data, the accelerometer assists in maintaining a stable flight path [17]. Accelerometers offer specific advantages, such as high-frequency stability data, which helps the flight controller quickly adjust for minor shifts, maintaining flight stability. They also provide continuous data on the UAV's tilt and altitude, which is crucial for operations that require precision, like mapping or surveying. However, accelerometers can be susceptible to issues such as noise and drift over time, which may impact long-duration flights. Techniques like Kalman filtering are often used to mitigate these issues, especially when accelerometer data is fused with gyroscope and GPS inputs to enhance accuracy [12, 17].

The gyroscope measures the UAV's angular velocity along three rotational axes: roll, pitch, and yaw. By detecting rotational movement, the gyroscope plays a critical role in maintaining orientation, allowing the UAV to make real-time corrections during dynamic maneuvers. This is particularly essential in environments with strong wind or when the UAV performs quick directional changes. In UAVs, MEMS-based gyroscopes are widely used, as they are compact, responsive, and integrate well with accelerometer data for precise movement tracking [17]. Gyroscopes play a critical role in maintaining the UAV's fixed orientation, ensuring stabilized video capture and smooth flight transitions. Additionally, they enable the flight controller to make rapid adjustments during sudden environmental changes or high-speed operations, enhancing overall flight performance and reliability. The main limitation of gyroscopes is their potential for drift, especially over long flights. Integrating gyroscope data with accelerometer and magnetometer readings in sensor fusion algorithms reduces this drift, allowing for improved reliability and accuracy in UAV navigation systems [12, 17].

Magnetometer measures magnetic field strength and direction, often used to provide heading information when GPS signals are weak or unavailable. This feature is particularly valuable for UAVs flying in dense urban areas or remote locations with limited satellite visibility. Magnetometers help maintain heading information, especially when GPS data is unreliable or obstructed by tall structures or dense foliage [17].

Figure 3 shows the classical configuration of IMU sensors.

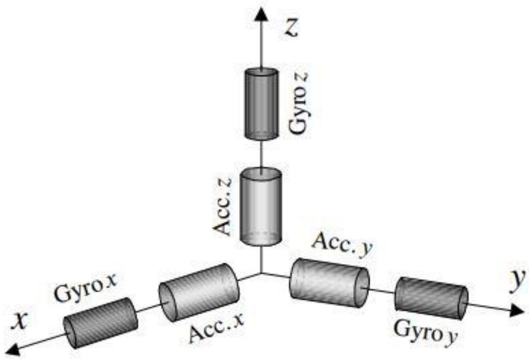

Figure 3. Classical configuration of IMU sensors [18]

Together, these sensors enable UAVs to detect and respond to dynamic changes in flight conditions. When combined with GPS data, IMU data allows UAVs to navigate smoothly and avoid obstacles even in environments with poor GPS signal quality. The integration of IMU sensors helps ensure that UAVs can perform in areas where GPS signals are intermittent, making the system more robust in challenging environments [12, 18, 19].

In UAVs, stability and control are paramount for ensuring reliable operation under varying flight conditions. IMUs, which typically combine accelerometers, gyroscopes, and sometimes magnetometers, are critical for enhancing the stability and control of UAVs by providing real-time measurements of the vehicle's orientation and motion. The integration of IMUs with other navigation systems, such as GPS, significantly improves UAV performance, particularly in environments with weak or unreliable GPS signals, such as urban canyons or dense forests.

IMUs provide high-frequency data that is essential for maintaining the UAV's attitude (pitch, roll, and yaw) and velocity (acceleration and angular velocity). These measurements enable the flight control system to make rapid adjustments to stabilize the UAV in response to external disturbances or aerodynamic forces. The accelerometer in an IMU measures linear acceleration, while the gyroscope records angular velocity, allowing the UAV to maintain its desired orientation with high precision. This capability is especially critical in applications such as aerial mapping, surveillance, and search-and-rescue missions, where precise control and stability are crucial for mission success.

When GPS data is lost or degraded, the IMU continues to provide continuous measurements of the UAV's position and orientation, ensuring uninterrupted operation. Studies have shown that IMU-based systems can significantly enhance UAV performance by compensating for GPS signal loss or interference, which is particularly important in precision applications such as surveying and infrastructure inspection [8].

Additionally, the small size and low weight of MEMS-based IMUs make them ideal for UAV applications, where minimizing payload is critical. These advantages, combined with the ability to integrate IMU systems with GPS, result in improved UAV stability, reliability, and control, enabling successful operations across a wide range of demanding tasks [8, 20].

While IMUs offer significant advantages in UAVs, such as providing high-frequency data on motion and orientation, they also have several limitations that must be addressed for optimal performance in various UAV applications. These limitations stem from factors such as sensor drift, bias accumulation, and sensitivity to environmental conditions.

One of the primary limitations of IMU systems is the inherent drift that occurs over time due to sensor inaccuracies. Gyroscopes, which measure angular velocity, are prone to drift, meaning that small errors in the measurement can accumulate, leading to larger deviations in the UAV's estimated position and orientation. Over time, this drift can result in significant errors in navigation and control, particularly in long-duration flights where frequent corrections are required [21].

Another limitation of IMUs is the sensitivity of accelerometers and gyroscopes to temperature fluctuations and other environmental factors. These sensors can experience varying degrees of error under different temperature conditions, which can lead to biases in the measurements. As MEMS-based sensors are more compact and cost-effective, they tend to be more susceptible to environmental variations compared to larger, more precise sensors [16]. This challenge can be particularly problematic in UAV applications that operate in harsh or rapidly changing environments, where temperature variations are common.

Additionally, while the integration of IMU and GPS data via sensor fusion techniques such as Kalman filtering has been shown to improve accuracy, the reliability of the GPS signal itself can be a limiting factor. IMUs can maintain accurate orientation and motion data when GPS signals are unavailable, but they cannot provide the positional accuracy required for many UAV tasks, such as surveying or mapping, without the aid of external navigation systems. This issue emphasizes the importance of robust sensor fusion techniques that combine IMU data with reliable positioning systems to enhance overall UAV performance.

Despite these limitations, advancements in IMU technology and sensor fusion methods continue to improve the performance of UAV systems. Ongoing research focuses on reducing the impact of drift, enhancing temperature stability, and optimizing sensor fusion algorithms to further improve the accuracy and reliability of IMU-based navigation systems for UAVs.

IMU systems have become an integral part of UAV navigation due to their ability to provide real-time data on orientation, velocity, and acceleration. However, the performance of IMUs can be limited by factors such as sensor drift, noise, and sensitivity to environmental conditions. Recent advancements in IMU technology have addressed these limitations, improving the accuracy, reliability, and overall performance of UAV systems.

One significant enhancement is the integration of advanced sensor fusion algorithms, such as Kalman filtering, which combines IMU data with other navigational sensors like GPS and magnetometers. This fusion allows UAVs to compensate for the drift and bias that are inherent in standalone IMU systems. The combination of GPS and IMU data can significantly reduce errors in UAV positioning and orientation, even in GPS-denied environments, improving system stability and precision for tasks such as surveying and agriculture [8].

Another key enhancement in IMU systems is the use of high-precision MEMS sensors. MEMS-based accelerometers and gyroscopes offer smaller sizes, lower costs, and better integration with other systems, which is particularly advantageous for UAV applications where payload weight and space are critical. These sensors can now achieve higher accuracy and stability compared to earlier MEMS models, making them more suitable for precise control in UAV flight dynamics. Additionally, MEMS sensors are often designed to be more resilient to environmental factors, such as temperature and humidity, thus enhancing their performance in varying conditions [16].

Furthermore, the development of error correction techniques has greatly improved the performance of IMU systems in UAVs. Recent advancements in bias correction, drift compensation, and noise filtering are essential for extending the operational time of IMUs without significant performance degradation. These error correction techniques can significantly mitigate the impact of environmental noise and sensor imperfections, ensuring that UAVs can maintain high accuracy during extended flights [22].

The fusion of IMU data with external reference systems, such as RTK GPS or DGPS, has become another essential enhancement. RTK and DGPS systems provide real-time corrections to GPS data, achieving centimeter-level accuracy, and when combined with IMU data, they allow for even more precise UAV navigation, particularly in critical applications such as surveying, infrastructure inspection, and precision farming [3, 8].

These enhancements in IMU technology and integration with other systems have made UAVs more robust, accurate, and reliable, enabling their use in a wide range of applications, from autonomous delivery to disaster response. Figure 4 depicts sample IMU sensor placement and orientation of the quadrotor.

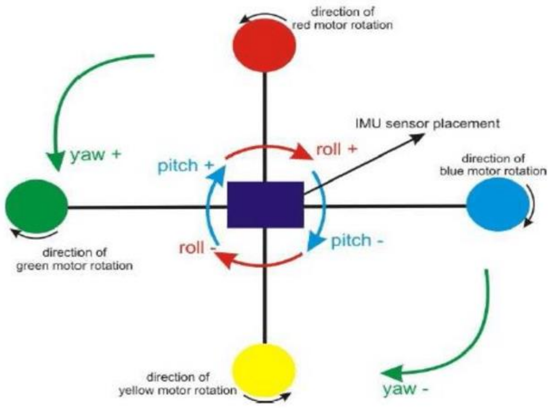

Figure 4. IMU sensor placement and orientation of the quadrotor [23]

2.2 Comparative Analysis of GPS and IMU Systems

GPS and IMU systems are critical for UAV navigation, providing complementary capabilities. GPS offers long-term positional accuracy, global coverage, and support for real-time corrections via methods such as RTK and DGPS, making it indispensable for tasks like surveying, mapping, and waypoint navigation. IMU, on the other hand, provides high-frequency orientation and motion data, enabling stability and control in dynamic environments. Its independence from external signals allows reliable performance in GPS-denied areas like urban canyons or dense forests.

However, both systems also have their limitations. GPS is susceptible to signal loss or degradation due to environmental obstructions such as buildings and trees, as well as atmospheric interference. Additionally, it is vulnerable to intentional disruptions like jamming and spoofing. IMU, meanwhile, experiences drift over time due to sensor biases and noise, leading to reduced accuracy during extended operations. It is also sensitive to environmental conditions such as temperature changes.

So, integrating these two systems has its benefits. Combining GPS and IMU mitigates individual limitations, ensuring both absolute and relative accuracy. GPS corrects IMU drift, while IMU compensates for temporary GPS outages, enabling robust navigation even in challenging environments.

3. INTEGRATION of GPS and IMU SYSTEMS

The integration of GPS and IMU systems enhances UAV navigation by addressing the limitations of each. GPS corrects long-term drift in IMUs, while IMUs provide continuous data during GPS signal loss. Advanced fusion algorithms, such as Kalman filtering, ensure seamless integration, enabling UAVs to navigate accurately even in challenging environments.

GPS provides highly accurate absolute positioning but is susceptible to signal interruptions or degradation due to environmental factors such as buildings, trees, or poor satellite geometry. IMUs, on the other hand, are not affected by external factors and provide continuous measurements of orientation and relative movement. Integration of the two systems helps mitigate GPS signal loss or errors, significantly improving overall accuracy and reliability. This is particularly beneficial in GPS-denied environments or when GPS signals are weak or unavailable, such as urban canyons or indoors [17, 24].

IMUs, particularly MEMS-based units, offer real-time orientation data that can fill in gaps during GPS outages, such as when passing through tunnels or dense urban environments. IMUs track motion continuously, making it possible to maintain a stable and continuous navigation solution, even in the absence of GPS. This is crucial for applications requiring uninterrupted movement tracking, such as autonomous vehicles and robotics [25].

While IMUs excel in providing short-term stability, they suffer from drift over time due to sensor biases and noise. GPS, when available, provides a reliable external reference to correct this drift. By applying sensor fusion algorithms, such as Kalman filters, GPS and IMU data can be combined to minimize drift and improve long-term positioning accuracy. The correction of IMU drift through GPS significantly enhances system performance over extended periods [21, 26]

GPS signals can be weak or unavailable in certain environments, such as indoors or in GPS-denied areas. IMUs, however, are independent of external signals and can operate in these conditions, providing continuous navigation data. The fusion of IMU data with GPS ensures that, even when GPS signals are temporarily lost, the system continues to function effectively by relying on the IMU's motion data. This combination enhances the versatility of navigation systems across a variety of challenging environments, as noted in several studies [10, 26].

The integration of GPS and IMU enhances the resilience of navigation systems. When GPS is available, it provides accurate absolute positioning, while IMU data can fill in when GPS is unavailable, maintaining continuous and reliable navigation. This redundancy is particularly beneficial for autonomous driving, UAVs, and robotics, where safe and accurate operation is essential. Robustness to system failures and signal degradation is a key advantage of GPS/IMU integration [24].

While high-end GPS systems can be costly, MEMS IMUs offer a more affordable solution for orientation and motion tracking. Integrating low-cost IMUs with GPS provides a scalable and economical approach to improve system performance without the need for expensive equipment. This makes GPS/IMU integration accessible for a wide range of applications, from consumer-grade UAVs to industrial autonomous systems [16, 19].

In summary, the integration of GPS and IMU systems offers a versatile, accurate, and cost-effective solution that overcomes the limitations of each technology. By complementing each other's strengths and compensating for weaknesses, the combination of GPS and IMU is essential for reliable and continuous navigation in dynamic and GPS-challenged environments [10, 27, 28].

Each of the GPS and IMU systems has significant limitations. GPS provides high accuracy in open areas, but its signal can be lost or degraded in challenging environments such as urban canyons or mountainous regions. On the other hand, IMU sensors offer internal data when GPS signals are unavailable, but they suffer from drift over time, leading to reduced accuracy. Both systems, when used individually, have limited reliability and precision. To overcome these standalone limitations, UAVs often use GPS-IMU sensor fusion techniques, such as Kalman filtering, which combines the strengths of both systems. This integration allows UAVs to maintain accurate, real-time navigation data, compensating for GPS signal loss and IMU drift, especially in challenging environments.

4. SENSOR FUSION TECHNIQUES in UAVs

Sensor fusion in UAVs involves combining data from multiple sensors, primarily GPS and IMU, to enhance navigation accuracy, reliability, and performance. This process mitigates the limitations of standalone systems by leveraging their complementary strengths. Under sub-headings 4.1 to 4.3, the following topics will be discussed in order: Kalman filter-based fusion (4.1), complementary filtering (4.2), and machine learning approaches (4.3).

4.1 Kalman Filter-Based Fusion

The Kalman Filter (KF) has been extensively used in GPS/IMU integration due to its ability to combine measurements from multiple sensors in a statistically optimal manner. This algorithm operates by predicting the state of a system and then updating this prediction based on new measurements, minimizing the influence of noise and uncertainties. For GPS and IMU systems, the Kalman Filter has historically proven effective in addressing their complementary strengths and weaknesses. The filter enables the fusion of GPS and IMU data, allowing GPS to correct IMU drift and IMU to interpolate GPS measurements during signal loss [29, 30]. Mathematically, the Kalman Filter follows a recursive estimation process consisting of two main steps: prediction and update [31]. In the prediction step, the system's state is estimated using the process model, defined as in (1):

$$\hat{X}_{k|k-1} = F_k\, \hat{x}_{k-1|k-1} + B_k u_k + w_k \quad (1)$$

where $\hat{X}_{k|k-1}$ is the predicted state vector at time k, F_k is the state transition matrix, B_k is the matrix representing the effect of control input on the system, u_k is the external control input, and w_k represents the process noise.

The corresponding error covariance is updated as in (2):

$$P_{k|k-1} = F_k P_{k-1|k-1} F_k^T + Q_k \quad (2)$$

where $P_{k|k-1}$ is the predicted error covariance, $P_{k\_1|k-1}$ is the updated error covariance from the previous step, Q_k is the process noise covariance matrix, which accounts for uncertainties in the system model.

During the update step, the Kalman Gain is computed as in (3):

$$K_k = P_{k|k-1} H_k^T (H_k P_{k|k-1} H_k^T + R_k)^{-1} \quad (3)$$

where K_k is the Kalman Gain, which determines how much the measurement should influence the state estimate, H_k is the measurement matrix that maps the system state to the observed measurements, and R_k is the measurement noise covariance matrix, representing uncertainties in sensor measurements.

The state estimate is then corrected as in (4):

$$\hat{x}_{k|k} = \hat{x}_{k|k-1} + K_k (z_k - H_k \hat{x}_{k|k-1}) \quad (4)$$

where z_k is the actual measurement at time k, and the term $(z_k - H_k \hat{x}_{k|k-1})$ represents the measurement residual (innovation), which quantifies the difference between the predicted and observed values.

Finally, the updated error covariance is computed as in (5):

$$P_{k|k} = (I - K_k H_k) P_{k|k-1} \quad (5)$$

where I is the identity matrix. This equation ensures that the uncertainty in the estimated state is minimized as new data is processed.

In earlier applications, Kalman Filter-based fusion methods predominantly relied on the Standard Kalman Filter (SKF) for linear systems. However, as UAV navigation evolved to involve increasingly complex and nonlinear dynamics, the Extended Kalman Filter (EKF) emerged as the preferred approach. The EKF linearizes nonlinear functions around the current state estimate, offering a highly effective solution for UAV applications. Additionally, adaptive variants of the Kalman Filter were developed to manage time-varying noise levels, addressing challenges caused by environmental factors or changes in UAV velocity. Unlike the standard KF, the EKF can handle nonlinearities by linearizing the system dynamics around the current estimate using a first-order Taylor expansion. The nonlinear state-space model is given in (6) and (7):

$$x_k = f(x_{k-1}, u_k) + w_k \quad (6)$$

$$z_k = h(x_k) + v_k \quad (7)$$

where $f\,and\,h$ are nonlinear functions describing the system dynamics and measurements, respectively. The EKF approximates these equations by computing the Jacobians of *f(x)* and *h(x),* which are used in place of F_k and H_k in the standard Kalman equations. This approach allows the filter to handle complex UAV motion models, including those involving attitude estimation and high-speed maneuvers.

In addition to improving accuracy, Kalman Filter-based fusion demonstrated resilience in GPS-denied environments. For instance, during temporary GPS outages, the filter's predictive step relied solely on IMU measurements to estimate the UAV’s position. Though prone to increased drift during prolonged outages, this approach significantly improved operational reliability in challenging conditions such as urban canyons or under dense foliage [32]. In Figure 5, advanced work illustrated how tightly coupled GPS/IMU integration, leveraging Kalman Filtering, could further mitigate the limitations of standalone systems by processing raw satellite signals and IMU data simultaneously, rather than relying on processed GPS outputs [10].

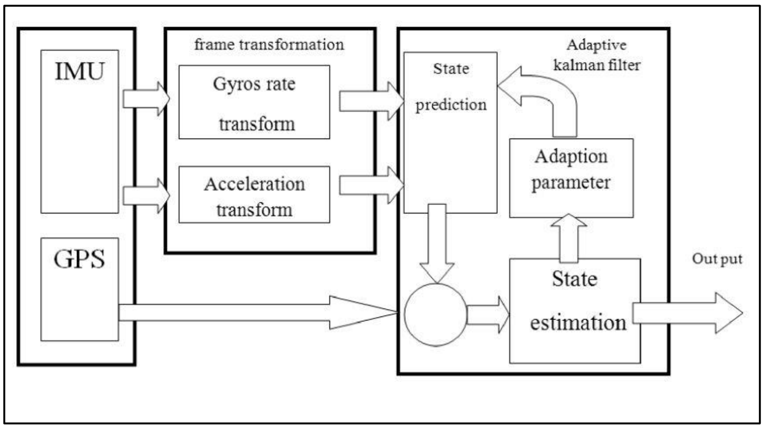

Figure 5. System implementation diagram [33]

Despite these advantages, the Kalman Filter has limitations. Its performance depended on accurate modeling of system dynamics and noise covariance matrices, which often required manual tuning. This tuning process was time-consuming and sensitive to sensor quality, particularly in low-cost UAV applications. Modern advancements have shifted focus toward machine learning-based fusion methods, but the Kalman Filter remains a benchmark in sensor fusion, particularly for its computational efficiency and real-time applicability in resource-constrained UAV platforms.

4.2 Complementary Filtering

Complementary Filtering has been widely used as a lightweight and effective method for fusing GPS and IMU data, especially in resource-constrained UAV systems. Unlike the computationally intensive Kalman Filter, the Complementary Filter operates on a straightforward principle, combining high-frequency data from IMUs with low-frequency, long-term accurate data from GPS to produce a reliable and stable navigation solution. This method assumes that the errors in each data source are complementary short-term inaccuracies in GPS data are corrected by IMU measurements, while long-term drift in IMU data is mitigated using GPS corrections [11].

Historically, Complementary Filters have been applied in scenarios where computational simplicity and low power consumption were critical. For UAVs, these filters proved particularly useful for attitude estimation, where gyroscope data from the IMU provided rapid orientation changes, and accelerometer or GPS measurements ensured long-term stability. Complementary Filters were well-suited for small UAVs due to their ease of implementation and low demand on processing resources [10].

The mathematical foundation of Complementary Filtering lies in the use of frequency-domain filtering. High-pass filters are applied to IMU gyroscope data to capture rapid changes, while low-pass filters smooth GPS position data to remove high-frequency noise. These filtered components are then combined to produce an accurate and stable estimate of the UAV's state. This simple structure made Complementary Filters particularly attractive for earlier UAV applications where high-cost or high-performance processing units were unavailable.

However, the performance of Complementary Filters depends on the accurate tuning of the filter gains, which balance the contributions of GPS and IMU data. Early implementations often relied on fixed gain values, which could lead to suboptimal performance in dynamic environments where noise characteristics varied over time. Recent advancements have addressed this limitation by introducing adaptive gain mechanisms that adjust filter parameters based on the operating conditions. For example, adaptive filters have been used to dynamically weigh GPS input more heavily in stable conditions and rely on IMU data during GPS outages.

Despite these advancements, Complementary Filters are not without limitations. Unlike Kalman Filters, they do not provide probabilistic estimates of uncertainty, making them less robust in situations with highly variable noise or extreme sensor errors. Moreover, they cannot handle the intricate coupling of sensor states in tightly integrated navigation systems. As UAV applications demand increasingly complex maneuvers and higher levels of precision, Complementary Filtering is often used in tandem with more advanced algorithms, such as Extended Kalman Filters, to enhance overall performance [24].

Nevertheless, Complementary Filters remain a popular choice for low-cost UAVs and other systems where computational efficiency and simplicity outweigh the need for more sophisticated data fusion techniques. Their continued relevance lies in their adaptability and effectiveness for lightweight sensor fusion, particularly in emerging applications where basic yet reliable navigation solutions are required.

4.3 Machine Learning Approaches

Machine learning (ML) has emerged as a transformative approach for sensor fusion in GPS/IMU integration, offering innovative solutions to address challenges in UAV navigation. Unlike traditional methods such as Kalman or Complementary Filtering, ML-based approaches can learn complex patterns and nonlinear relationships directly from data, enabling adaptive and robust performance even in highly dynamic environments. This capability has made ML increasingly popular in scenarios where traditional algorithms struggle, such as GPS-denied environments, abrupt maneuvers, or varying sensor noise characteristics [34, 35].

Machine learning techniques applied to GPS/IMU integration typically fall into two categories: supervised learning and reinforcement learning. Supervised learning involves training models on labeled datasets to predict navigation states, such as position, orientation, or velocity. For example, neural networks have been utilized to estimate position and correct IMU drift based on historical GPS/IMU data. Reinforcement learning, on the other hand, can optimize decision-making by learning from interactions with the environment, making it useful for dynamic or GPS-denied scenarios.

Deep learning models, such as Long Short-Term Memory (LSTM) networks, have been shown to effectively capture temporal dependencies in sensor data, outperforming traditional algorithms in dynamic conditions [36]. Other architectures, such as Convolutional Neural Networks (CNNs), Recurrent Neural Networks (RNNs), and Gated Recurrent Units (GRUs) have also demonstrated strong performance in capturing spatial and temporal patterns in sensor data, depending on the specific characteristics of the data and the application.

LSTM networks are especially effective when working with time-series data, where long-range temporal dependencies are crucial. For instance, in applications like UAV attitude estimation, LSTMs can model the sequential nature of sensor measurements and predict future sensor states with higher accuracy, even in the presence of noise or complex environmental conditions. The ability of LSTMs to maintain the memory of past data points through their gating mechanisms allows them to outperform traditional methods, such as Kalman filters, in dynamic and non-linear scenarios [37, 38].

On the other hand, CNNs are typically applied to problems involving spatial data, such as images or video frames. CNNs are capable of identifying hierarchical spatial features in sensor data, making them particularly useful in multi-modal sensor fusion, where data from sources like cameras, LiDAR, or thermal sensors must be combined [39]. When paired with temporal models like LSTMs, CNNs can extract both spatial and temporal features, which is beneficial for tasks such as object detection, scene recognition, and path planning in autonomous systems.

RNNs, along with their more efficient variants, GRUs, are another powerful class of models for sequential data processing. Unlike traditional feedforward networks, RNNs and GRUs maintain an internal state that helps capture the temporal dependencies between data points in sequences. GRUs are particularly effective in reducing computational complexity compared to LSTMs while still handling sequential data well. These models are well-suited for continuous data streams, such as those generated by IMU or GPS sensors, where real-time processing is essential [40].

One of the key advantages of ML approaches is their ability to incorporate a wide variety of input features beyond GPS and IMU data, such as barometric altitude, magnetometer readings, and environmental context (e.g., visual data from cameras). This multimodal integration allows for richer and more accurate navigation solutions. Additionally, ML models can adapt to sensor degradation or failures, making them particularly valuable for long-term UAV operations [35].

Despite their advantages, ML-based methods face challenges, particularly in the context of UAV navigation. First, the reliance on large-labeled datasets for training can be a barrier, as collecting and annotating high-quality GPS/IMU data under various environmental conditions is resource-intensive. Second, the computational demands of ML models, especially deep learning, can strain the limited processing power and battery life of UAVs [41, 42]. Researchers have explored lightweight ML architectures and edge computing solutions to address these constraints. Lastly, the generalization of ML models across different UAV platforms and environments remains a challenge, as models trained in one scenario may perform poorly in others. Techniques such as domain adaptation and online learning have been proposed to improve robustness [21, 34, 41].

Looking ahead, the integration of ML with traditional methods, such as hybrid models combining neural networks with Kalman Filters, offers promising directions for UAV navigation. These hybrid systems leverage the strengths of both approaches, using ML to capture complex dynamics and traditional methods to ensure reliability and interpretability. As UAV applications expand, ML-based approaches are expected to play an increasingly critical role in achieving autonomous, efficient, and adaptive navigation.

To help readers compare the various sensor fusion methods discussed in this section, Table 1 provides a concise overview of their advantages and limitations. It summarizes the key characteristics of each method, highlighting factors such as computational efficiency, adaptability, and suitability for different UAV navigation scenarios.

Table 1. Comparison of sensor fusion methods for GPS/IMU integration

Method	Advantages	Limitations
Kalman Filter	Provides optimal estimation by modeling probabilistic uncertainty. Works well in sensor fusion.	Requires accurate system modeling and fine-tuning of noise covariance. Sensitive to poor system models.
Extended Kalman Filter (EKF)	Effectively addresses nonlinearities by linearizing the system based on the current state.	Computationally expensive and performance degrades with large nonlinearities in the system model.
Complementary Filter	Simple and computationally efficient, making it suitable for lightweight UAVs and real-time applications.	Struggles with highly dynamic conditions, especially with rapid changes in motion or acceleration. Does not provide uncertainty estimates.
Machine Learning (ML)	Can adapt to complex and dynamic environments, effectively incorporating multiple data sources.	Requires large-labeled datasets, is computationally intensive, and may not generalize well across platforms.
Deep Learning (LSTM, CNN, RNN, GRU)	Adapts to dynamic and complex environments, efficiently combining multiple data sources.	Requires large datasets, high computational power, and may have difficulty with real-time processing due to slow inference times.

5. OPEN CHALLENGES in GPS/IMU INTEGRATION

One of the most significant challenges in UAV navigation is mitigating the impact of GPS signal loss or degradation. UAVs frequently operate in environments where GPS signals are obstructed, such as urban canyons, dense forests, or underwater. Intentional interference, including jamming and spoofing, further exacerbates GPS reliability issues [13]. While IMU systems can temporarily compensate during GPS outages, their drift errors accumulate over time, reducing navigational accuracy. Addressing these issues requires advancements in anti-jamming capabilities, the adoption of alternative positioning systems such as GLONASS or Galileo, and the development of enhanced sensor fusion techniques to ensure uninterrupted navigation [7, 13, 27].

Low-cost IMUs, commonly used in consumer UAVs, present additional challenges due to significant errors stemming from sensor noise and temperature sensitivity. These limitations hinder precise navigation during extended GPS outages. Advanced calibration methods, high-performance MEMS-based IMUs, and machine learning models that predict and correct sensor-specific errors could mitigate long-term drift and improve reliability [12, 19].

The computational demands of GPS/IMU integration, particularly with advanced techniques like Extended Kalman Filters or machine learning-based fusion methods, strain the limited processing power of UAV platforms. This issue is especially pronounced in small UAVs where weight and power efficiency are critical. Optimized algorithms that balance computational efficiency with navigational accuracy, such as lightweight neural networks and adaptive filters, are essential to enable real-time processing in resource-constrained systems [7, 9, 34].

UAVs also face dynamic and unpredictable environments, such as disaster zones or crowded airspaces, which require navigation systems capable of adapting to rapid changes in motion, obstacles, and environmental conditions. Adaptive frameworks that adjust parameters in real-time based on operational contexts are critical for ensuring reliability under such conditions [2,15]. Swarm operations introduce further complexity, necessitating precise relative positioning among UAVs. GPS inaccuracies and IMU drift pose challenges to synchronized swarm behaviors, making decentralized fusion algorithms and robust inter-UAV communication protocols essential [14].

Integrating GPS/IMU systems with emerging technologies such as Light Detection and Ranging (LiDAR), cameras, and 5G-based positioning systems holds great promise for enhancing UAV navigation. However, incorporating additional sensors increases the complexity of data fusion, requiring advanced algorithms capable of managing diverse data streams with varying levels of uncertainty and frequency. Developing hybrid techniques that integrate these modalities seamlessly without imposing significant computational overhead will be crucial [24, 27].

Energy constraints represent another significant hurdle, particularly for long-duration UAV missions. The continuous operation of GPS and IMU sensors, combined with real-time processing requirements, places a heavy burden on battery life. Innovations in low-power hardware design and energy-efficient computational techniques are critical to extending operational endurance [7, 40].

As UAV operations expand, GPS/IMU integration systems must also align with evolving regulatory and safety requirements. Reliable performance in GPS-denied conditions and robust fail-safe mechanisms will be essential for compliance and the safe integration of UAVs into shared airspace, particularly in urban and commercial settings [13, 23].

6. FUTURE DIRECTIONS

Future research in GPS/IMU integration will likely focus on developing hybrid sensor fusion frameworks that combine traditional methods with machine learning techniques. These frameworks could provide greater adaptability to diverse operating environments by leveraging the strengths of deterministic models like Kalman Filters and data-driven approaches to improve robustness and accuracy.

Advancements in hardware, particularly in low-power, high-precision MEMS-based IMUs, will play a pivotal role. Emerging IMUs with higher sensitivity and reduced drift, coupled with miniaturized multiconstellation GNSS receivers, could significantly enhance UAV navigation reliability. Additionally, novel positioning technologies such as 5G and visual odometry may further improve performance, especially in GPS-degraded or denied environments.

The increasing demand for UAV swarm operations will drive innovations in decentralized navigation systems. Real-time inter-UAV communication and collaborative sensor fusion will be critical for precise relative positioning and coordinated flight paths, enabling applications ranging from disaster response to large-scale agricultural monitoring.

Computational and energy efficiency will remain key areas of focus. Lightweight algorithms, edge computing, and energy-efficient hardware are essential for extending UAV operational durations without compromising accuracy. Future systems may also incorporate self-learning capabilities, allowing UAVs to adapt to new environments and sensor degradation over time.

By addressing these challenges and pursuing these advancements, GPS/IMU integration will continue to evolve, supporting the growing complexity and demands of modern UAV applications while unlocking new possibilities in navigation and autonomous operation.

7. CONCLUSION

This review highlighted the essential roles, advantages, and limitations of GPS and IMU systems in UAV navigation. The complementary nature of GPS and IMU systems has led to the development of sensor fusion techniques that significantly enhance the accuracy and reliability of UAV navigation. While GPS provides long-term absolute positioning, IMUs offer high-frequency orientation data, allowing UAVs to navigate effectively. However, challenges such as IMU drift, GPS signal loss, sensor fusion complexity, and environmental sensitivity can affect the overall performance of these systems. Sensor fusion techniques, including Kalman Filtering, Complementary Filtering, and machine learning-based methods, offer promising solutions to address the limitations of standalone GPS and IMU systems. Advances in AI and sensor technology are expected to drive further improvements in UAV navigation systems, making them more resilient to environmental factors and adaptable to a broader range of applications.

REFERENCES

[1] N. Tuśnio and W. Wróblewski, "The efficiency of drones usage for safety and rescue operations in an open area: A case from Poland," *Sustainability,* 2022, 14, 327, doi: https://doi.org/10.3390/su14010327.

[2] E. Choi and S. Chang, “A consumer tracking estimator for vehicles in GPS-free environments,” *IEEE Trans. Consum. Electron.*, vol. 63, no. 4, pp. 450–458, Jan. 2018, doi: https://doi.org/10.1109/TCE.2017.015064.

[3] S. H. Oh and D.-H. Hwang, "Low-cost and high performance ultra-tightly coupled GPS/INS integrated navigation method," *Advances in Space Research*., Dec. 2017, doi: https://doi.org/10.1016/j.asr.2017.06.007.

[4] P. A. C. Widagdo, H. -H. Lee and C. -H. Kuo, "Limb motion tracking with inertial measurement units," 2017 *IEEE International Conference on Systems, Man, and Cybernetics (SMC), Banff, AB, Canada*, 2017, pp. 582-587, doi: https://doi.org/10.1109/SMC.2017.8122669.

[5] F. Caron, E. Duflos, D. Pomorski, and P. Vanheeghe, "GPS/IMU data fusion using multisensor Kalman filtering: Introduction of contextual aspects," *Information Fusion*, vol. 7, no. 2, pp. 221-230, Jun. 2006, doi: https://doi.org/10.1016/j.inffus.2004.07.002.

[6] Z. Li, C. Su, Z. Su, H. Peng, Y. Wang, W. Chen, and Q. Wu, "Model Predictive Control Enabled UAV Trajectory Optimization and Secure Resource Allocation," *Researchgate*, Nov. 2024, doi: https://doi.org/10.48550/arXiv.2411.04423.

[7] M. S. Grewal, A. P. Andrews, C. G. Bartone “Global Navigation Satellite Systems, Inertial Navigation, and Integration”, *John Wiley & Sons Inc*, 2020.

[8] A. Leick, L. Rapoport, and D. Tatarnikov, "GPS Satellite Surveying", 4th ed. Hoboken, NJ, USA: *John Wiley & Sons Inc*, 2015.

[9] A. Waegli and J. Skaloud, "Optimization of two GPS/MEMS-IMU integration strategies with application to sports," *GPS Solutions*, *Springer-Verlag*, vol. 13, pp. 315-326, Apr. 2009, doi: https://doi.org/10.1007/s10291-009-0124-5.

[10] P. D. Groves, "Principles of GNSS, inertial, and multi-sensor integrated navigation systems" *2nd ed-Artech House*, 2013.

[11] B. Yun, K. Peng and B. M. Chen, "Enhancement of GPS Signals for Automatic Control of a UAV Helicopter System," *IEEE International Conference on Control and Automation*, Nov. 2007, pp. 1185-1189, doi: https://doi.org/10.1109/ICCA.2007.4376547.

[12] I. A. Faisal, T. W. Purboyo, and A. S. R. Ansori, "A Review of Accelerometer Sensor and Gyroscope Sensor in IMU Sensors on Motion Capture," *Journal of Engineering and Applied Sciences*, vol. 15, no. 3, pp. 826–829, Nov. 2020, doi: https://doi.org/10.36478/jeasci.2020.826.829.

[13] E. Shafiee, M. R. Mosavi, and M. Moazedi, "A Modified Imperialist Competitive Algorithm for Spoofing Attack Detection in Single-Frequency GPS Receivers,", *Wireless Personal Communications*, vol. 119, pp. 919-940, Feb. 2021, doi: https://doi.org/10.1007/s11277-021-08244-2.

[14] S. S. Naik and A. M. Achar, "Unmanned Aerial Vehicle Communication for Autonomous Operations," *ResearchGate*, Mar. 2024, doi: https://doi.org/10.13140/RG.2.2.14050.13769.

[15] G.V. Hristov, P. Z. Zahariev, and I. H. Beloev, "A review of the characteristics of modern unmanned aerial vehicles," *Acta Technologica Agriculturae*, vol. 19, no. 2, pp. 33-38, Jun. 2016, doi: https://doi.org/10.1515/ata-2016-0008.

[16] G. D. Aydin and S. Ozer, "Infrared Detection Technologies in Smart Agriculture: A Review," *International Aegean Conference on Electrical Machines and Power Electronics (ACEMP) & 2023 International Conference on Optimization of Electrical and Electronic Equipment (OPTIM), Istanbul, Turkiye*, 2023, pp. 1-8, doi: https://doi.org/10.1109/ACEMP-OPTIM57845.2023.10287033.

[17] D. Titterton and J. Weston, "Strapdown Inertial Navigation Technology," 2nd ed., *The Institution of Electrical Engineers*, 2004.

[18] T. L. Grigorie and R. M. Botez, "Miniaturized Inertial Sensors' Noise Reduction by Using Redundant Linear Configurations," *The 19th IASTED International Conference on Applied Simulation and ModelingAt: Crete, Greece*, pp. 74-81, Jun. 2011, doi: https://doi.org/10.2316/P.2011.715-051.

[19] M. S. Amin, M. B. I. Reaz, S. S. Nasir, and M. A. S. Bhuiyan, "Low Cost GPS/IMU Integrated Accident Detection and Location System," *Indian Journal of Science and Technology*, vol. 9, no. 10, pp. 1-9, Mar. 2016, doi: https://doi.org/10.17485/ijst/2016/v9i10/80221.

[20] G. D. Aydin, "A Wafer Level Vacuum Packaging Technology For MEMS-Based Long-Wave İnfrared Sensors", Aug. 2022.

[21] R. C. Avram, X. Zhang, J. Campbell, and J. Muse, "IMU Sensor Fault Diagnosis And Estimation For UAVs", *International Federation of Automatic Control*, vol. 48, no. 21, pp. 380–385, 2015, doi: https://doi.org/10.1016/j.ifacol.2015.09.556.

[22] L. L. Arnold and P. A. Zandbergen, "Positional accuracy of the Wide Area Augmentation System in consumer-grade GPS units," *Computers & Geosciences*, vol. 37, no. 7, pp. 883-892, Jul. 2011, doi: https://doi.org/10.1016/j.cageo.2010.12.011.

[23] A. Sathyan, S. Kukreti, S. Sridhar, and E. Kivelevitch, "Location Determination of an Unmanned Aerial Vehicle in a GPS-Denied, Hazard-Cluttered Indoor Environment," *AIAA Infotech @ Aerospace Conference*, Jan. 2015, doi: https://doi.org/10.2514/6.2015-2028.

[24] Y. Zhao, "GPS/IMU integrated system for land vehicle navigation based on MEMS," *Royal Institute of Technology (KTH)*, Sep. 2011.

[25] Y. Wang, J. Mangnus, D. Kostić, H. Nijmeijer, and S. T. H. Jansen, "Vehicle state estimation using GPS/IMU integration,", *SENSORS, 2011 IEEE, Limerick, Ireland*, 2011, pp. 1815-1818, doi: https://doi.org/10.1109/ICSENS.2011.6127142.

[26] T. S. Bruggemann, D. G. Greer, and R. A. Walker, "GPS fault detection with IMU and aircraft dynamics," *IEEE Transactions on Aerospace and Electronic Systems*, vol. 47, no. 1, pp. 305-316, Jan. 2011, doi: https://doi.org/10.1109/TAES.2011.5705677.

[27] E. D. Kaplan and C. J. Hegarty, “Understanding GPS/GNSS: Principles and Applications,” 3rd ed., Artech House, 2017.

[28] M. Mostafa, J. Hutton, B. Raid, and R. Hill "GPS/IMU products - the Applanix approach,", Dec. 2003.

[29] F. Caron., E. Duflos, D. Pomorski, P. Vanheeghe, “GPS/IMU data fusion using multisensor Kalman filtering: Introduction of contextual aspects,” *Information Fusion*, vol. 7, no. 2, pp. 221-230, Jun. 2006, doi: https://doi.org/10.1016/j.inffus.2004.07.002.

[30] J. Meyer-Hilberg, T. Jacob, “High accuracy navigation and landing system using GPS/IMU system integration,” *Proceedings of 1994 IEEE Position, Location and Navigation Symposium - PLANS'94, Las Vegas, NV, USA*, 1994, pp. 298-305, doi: https://doi.org/10.1109/PLANS.1994.303327.

[31] Y. Kim, H. Bang, “Introduction to Kalman Filter and Its Applications”, Researchgate, Nov. 2018, doi: https://doi.org/10.5772/intechopen.80600.

[32] K. Gamagedara, T. Lee and M. Snyder, "Quadrotor State Estimation With IMU and Delayed Real-Time Kinematic GPS," *in IEEE Transactions on Aerospace and Electronic Systems*, vol. 57, no. 5, pp. 2661-2673, Oct. 2021, doi: https://doi.org/10.1109/TAES.2021.3061795.

[33] A. Fakharian, T. Gustafsson, and M. Mehrfam, "Adaptive Kalman Filtering Based Navigation: An IMU/GPS Integration Approach," *IEEE International Conference on Networking, Sensing and Control*, 2011, pp. 181-185, doi: https://doi.org/10.1109/ICNSC.2011.5874871.

[34] A. Carron, M. Todescato, R. Carli, L. Schenato, and G. Pillonetto, "Machine Learning Meets Kalman Filtering," *IEEE 55th Conference on Decision and Control (CDC)*, 2016, pp. 4594-4599, doi: https://doi.org/10.1109/CDC.2016.7798968.

[35] S. Mahfouz, F. Mourad-Chehade, P. Honeine, J. Farah, and H. Snoussi, "Target Tracking Using Machine Learning and Kalman Filter in Wireless Sensor Networks," *IEEE Sensors Journal*, vol. 14, no. 10, pp. 3715-3725, Oct. 2014, doi: https://doi.org/10.1109/JSEN.2014.2332098.

[36] C. Chen and X. Pan, "Deep Learning for Inertial Positioning: A Survey," *IEEE Transactions on Intelligent Transportation Systems*, vol. 25, no. 9, pp. 10506-10523, Sept. 2024, doi: https://doi.org/10.1109/TITS.2024.3381161.

[37] P. Narkhede, R. Walambe, S. Poddar, K. Kotecha. 2021.” Incremental learning of LSTM framework for sensor fusion in attitude estimation,” *PeerJ Computer Science*, doi: https://doi.org/10.7717/peerj-cs.662.

[38] Y. Wang, J. Li, P. Zou, Z. Guo, and W. Li, "Research on UAV Path Planning based on LSTM," *2023 International Conference on Integrated Intelligence and Communication Systems (ICIICS),* Kalaburagi, India, 2023, pp. 1-6, doi: https://doi.org/10.1109/ICIICS59993.2023.10421651.

[39] A. Elamin, A. El-Rabbany, UAV-Based Multi-Sensor Data Fusion for Urban Land Cover Mapping Using a Deep Convolutional Neural Network. *Remote Sens*., 2022, 14, 4298., doi: https://doi.org/10.3390/rs14174298.

[40] Q. Feng, J. Yang, Y. Liu, C. Ou, D. Zhu, B. Niu, J. Liu, and B. Li, "Multi-Temporal Unmanned Aerial Vehicle Remote Sensing for Vegetable Mapping Using an Attention-Based Recurrent Convolutional Neural Network," *Remote Sens*., vol. 12, no. 10, pp. 1668, 2020, doi: https://doi.org/10.3390/rs12101668.

[41] Y. Chang, Y. Cheng, U. Manzoor, and J. Murray, "A review of UAV autonomous navigation in GPS-denied environments," Robotics and Autonomous Systems, vol. 170, Dec. 2023, Art. no. 104533, doi: https://doi.org/10.1016/j.robot.2023.104533.

[42] S. Fei, M. A. Hassan, Y. Xiao, X. Su, Z. Chen, Q. Cheng, F. Duan, R. Chen, and Y. Ma, "UAV-based multi-sensor data fusion and machine learning algorithm for yield prediction in wheat," *Precision Agriculture*, 2022, vol. 24, pp. 187-212, doi: https://doi.org/10.1007/s11119-022-09938-8.

ALKU Journal of Science 2025, Sayı 7(1): 43-54
e-ISSN: 2667-7814

Review Article

An Overview of Non-Destructive Testing for Composites Materials

Mete Han Boztepe[1*]
[1]*Department of Mechanical Engineering, Sırnak University, Sırnak, Türkiye.*
**metehanboztepe@sirnak.edu.tr*

Abstract

Non-Destructive Testing (NDT) methods are essential for assessing the integrity and reliability of composite materials without causing damage. Composite materials are widely used in industries such as aerospace, automotive, and civil engineering. Therefore, the demand for advanced inspection techniques has increased. This study aims to compare the effectiveness of existing Non-Destructive testing (NDT) methods on composite materials and determine the most suitable techniques. Also, this article provides an overview of various NDT methods, including Visual Testing (VT) and Visual Inspection (VI), ultrasonic testing (UT), infrared thermography (IRT), and acoustic emission (AE). The advantages, limitations, and applications of these techniques are discussed. Their role in detecting defects such as delaminations, porosity, and fiber breakage observed in composite structures is highlighted.

Keywords: Composite materials, non-destructive testing, ultrasonic test, infrared thermography, acoustic emission.

Kompozit Malzemeler için Tahribatsız Muayeneye Genel Bakış

Özet

Tahribatsız Muayene (NDT) yöntemleri, hasara neden olmadan kompozit malzemelerin bütünlüğünü ve güvenilirliğini değerlendirmek için gereklidir. Kompozit malzemeler havacılık, otomotiv ve inşaat mühendisliği gibi endüstrilerde yaygın olarak kullanılmaktadır. Bu nedenle, gelişmiş muayene tekniklerine olan talep artmıştır. Bu çalışma, kompozit malzemeler üzerinde mevcut tahribatsız muayene (NDT) yöntemlerinin etkinliğini karşılaştırmayı ve en uygun teknikleri belirlemeyi amaçlamaktadır. Ayrıca bu makale, Görsel Muayene (VT) ve Görsel Muayene (VI), ultrasonik test (UT), kızılötesi termografi (IRT) ve akustik emisyon (AE) dahil olmak üzere çeşitli NDT yöntemlerine genel bir bakış sunmaktadır. Bu tekniklerin avantajları, sınırlamaları ve uygulamaları tartışılmaktadır. Kompozit yapılarda gözlemlenen delaminasyonlar, gözeneklilik ve lif kırılması gibi kusurları tespit etmedeki rolleri vurgulanmaktadır.

Anahtar Kelimeler: Kompozit malzemeler, tahribatsız muayene, ultrasonik test, kızılötesi termografi, akustik emisyon.

Geliş/Received: 1 Mart/1 March 2025
Kabul Ediliş/Accepted: 25 Mart/25 March 2025

1. INTRODUCTION

Composite materials are made up of two or more different materials, each of which adds superior properties to the final product. Composite materials are basically composed of a matrix and reinforcement. The matrix, a polymer, usually holds the fibers together to enhance the overall mechanical performance of the composite. This allows composites to outperform their components. Thanks to their high strength with low weight, they are used in many fields. Composite materials/structures have product efficiency, cost-effectiveness, and the development of unique specific properties (strength and modulus). It is widely used in aerospace, wind turbines, transportation, automotive, medical equipment and similar fields [1-4]. In the production of composite materials, unwanted materials or random porosity may occur. These unwanted defects adversely affect the structure and mechanical properties. These defects need to be uncovered to check the integrity of the composite. Various techniques can be used to detect such defects [5, 6].

Non-destructive testing (NDT) of composite materials can detect defects without affecting the integrity and mechanical properties of the materials. Various NDT methods have been developed to detect defects such as delaminations, voids, and fiber breakage, which are critical to ensure the reliability of composite structures used in aerospace, automotive, and civil engineering applications [4, 7]. Numerous techniques are used in non-destructive testing (NDT) of composite materials, including ultrasonic testing (UT), thermographic test (TT), infrared thermography test (IRT), radiographic test (RT), visual test (VT) or visual inspection (VI), acoustic emission test (AE), acoustic-ultrasonic (AU), shearography testing (ST), optical testing (OT), electromagnetic testing (ET), liquid penetrant testing (LPT), and magnetic particle testing (MPT) [8].

NDT is used to detect defects in nanocomposites. With this method, defects can be detected without affecting the performance of the inspected objects. The NDT technique can determine the shape, size, direction, and distribution of defects using various physical and chemical phenomena [9].

One of the most widely used NDT techniques is ultrasonic testing, which uses high-frequency sound waves to detect internal defects in composite materials. Ciecieląg et al. (2022) showed that ultrasonic testing in combination with repetition analysis effectively detects real defects in polymer composites. Furthermore, non-destructive testing allows the evaluation of the effect of moisture absorption on the mechanical properties of glass fiber-reinforced plastics [10]. Similarly, Acanfora et al. (2022) emphasized the importance of NDT methods for damage detection in composite materials. They stated that NDT methods are preferred due to the high costs of destructive testing [11].

The NDT technique may have limitations in some cases. Composite parts are frequently used in the aviation sector. They have extremely high aspect ratios such as aircraft wings and tails. Therefore, the NDT technique used must be able to examine large surfaces. NDT inspections of composite parts with complex geometries are difficult [12].

Infrared thermography (IRT) is another important NDT method widely applied to composite materials. This technique enables visualization of subsurface defects by capturing thermal radiation emitted from the surface of the composite. Liu et al. (2019) noted that IRT is particularly advantageous due to its fast inspection capabilities and ease of setup, making it suitable for large-area inspections [13]. Bale et al. (2014)used thermography to monitor damage propagation in glass fiber/epoxy composites by analyzing temperature changes on the material surface [14]. To test this method, Świderski & Pracht (2021) inserted artificial defects into a helmet made of aramid composite. The results confirmed the effectiveness of the NDT method used in these tests [15].

In addition to ultrasonic testing and thermography, shearography is another NDT method used for composite materials. This method provides full-field, non-contact measurements and can detect various defects, including delaminations and fiber breakage. This method is particularly used in thick composite structures [16]. Furthermore, the microwave non-destructive evaluation method (MWNDE) is a new technique that works in the electromagnetic spectrum to inspect dielectric structures and is used for composite inspection [17].

This study discusses some of the NDT methods used in composite materials. It categorizes them, discusses their advantages and limitations, and describes the NDT methods of composite materials.

2. CATEGORIZATION OF NDT TECHNIQUES

Composite materials are used in many engineering fields due to their high strength and low weight properties. Based on examinations of NDT methods, they can be categorized in different ways according to the applications and conditions of the test. NDT methods basically include contact and non-contact methods. Both methods have their specific applications in the testing and evaluation of composites. Most NDT techniques require good contact between the sensor and the composite surface under test to obtain reliable data. Contact methods include conventional ultrasonic testing, eddy current testing, magnetic testing, electromagnetic testing, and penetrant testing. Another way to speed up the data collection process is to eliminate the need for physical contact between the sensor and the structure under test. Non-contact methods include thermography, shearography, transmission ultrasonic, radiography testing, and visual inspection. Optical methods (e.g. thermography, holography, or shearography) are mostly non-contact. Table 1 shows contact and non-contact NDT methods [8].

Table 1. NDT methods for contact and non-contact categories

Contact Methods	**Non-Contact Methods**
Traditional ultrasonic testing	Through Transmission Ultrasonic
Eddy current testing	Radiography Testing
Magnetic testing	Thermography
Electromagnetic	Infrared Testing
Penetrant testing	Holography
Liquid penetrant	Shearography
-	Visual inspection

There are various methods of NDT technology. Their use depends on the structure, material, cost, and type of damage to be inspected. Each method has advantages and disadvantages. The classification of NDT methods according to defect types is given in Figure 1. For example, X-ray NDT is generally not suitable for detecting delamination defects, but delamination can be detected using ultrasonic or acoustic emission methods [18].

				METHODS			
Defects	**X-ray**	**Ultrasonic**	**Penetrant**	**Magnetic Particle**	**Eddy Current**	**Thermography**	**Acoustic Emission**
Porosity or Voids	✓	✓	⊙	⊙	⊙	⊙	✓
Delamination	⊙	✓	⊙	X	X	⊙	✓
Debonding	✓	✓	⊙	X	X	⊙	✓
Foreign Bodies	✓	✓	⊙	⊙	⊙	⊙	✓
Cracks	⊙	✓	⊙	✓	✓	⊙	✓
Surface	X	⊙	✓	✓	✓	✓	✓
Internal	✓	✓	X	⊙	⊙	⊙	✓
Limit	Orientation-dependent	Dead zone effect	Only open to surface defects	Ferromagnetic materials only	Conductive materials only	Small thickness	Lack of size and shape
Advantage	Inspection process is simple	Portable and good depth resolution	Suitable for mass-manufactured products	Rapid for complex surfaces	Suitable for hard-to-reach areas	Useful for quick response	Effective for active defects

Applicability→ suitable (✓); weak (X); limited (⊙).

Figure 1. The classification of NDT methods according to the defect

2.1 Visual Testing (VT) and Visual Inspection (VI)

Visual Testing (VT) and Visual Inspection (VI) are the most basic NDT methods used in many situations. This is because it can save both time and money by reducing the amount of other tests. One of the important advantages of visual inspection is that it is fast. Visual inspection does not require equipment, but this method has its disadvantages [8]. Inspection by visual method is highly dependent on the experience of the expert and the light conditions. Therefore, a more efficient and effective NDT method is highly demanded [19].

VT is an NDT method performed with professional equipment in accordance with certain standards. The VI technique is used for situations where simple visual inspection is sufficient and does not require detailed testing procedures. If critical defects in composite components need to be detected, VT is used. However, VI may be sufficient for general surface controls.

Visual Inspection (VI) is mainly used to detect superficial defects such as surface cracks and delaminations. However, it is not an effective method for detecting internal defects that may not be visible on the surface. For example, low-speed impacts can cause internal damage that is not easily detected by conventional visual methods [20]. Despite these limitations, more than 80% of inspections on large transport aircraft are performed using this method [21]

Visual inspection is one of the simple techniques often used in pipelines. The method is low-cost and fast. It sometimes provides enough information for decision-making. It is informative enough to eliminate the need for other advanced NDT methods. It is suitable for visual inspection, on-site inspection, in-service, and accessible pipelines. It is often used to diagnose visually obvious macro-scale defects such as leaks, surface cracks, and misaligned joints. Visual inspection is a contact-based technique that requires access to the pipeline itself and is only suitable for external defects such as cracks and porosity. During the process, site preparation is performed (such as pitting, target surface cleaning, etc.). A liquid paint (or paint spray) is then applied to the target pipe surface. The specialist can detect defects on the pipe surface with the naked eye or using an endoscope [22].

Various NDT techniques have been developed to overcome the disadvantages of VI. Infrared Thermography (IRT) and Electronic Speckle Pattern Interferometry (ESPI) are other methods used to detect defects in composite materials [23]. These techniques can identify subsurface defects that VI may miss. In addition, ultrasonic testing is used to detect impact damage in composite laminates and to measure the location and size of defects [24, 25].

Advanced techniques such as 3D scanning and digital image correlation (DIC) are being investigated to enhance visual inspection. These techniques allow real-time monitoring of composite structures, facilitating the detection of defects during manufacturing [26, 27]. Recent advances in artificial intelligence (AI) and machine learning have been applied to visual inspection techniques. AI-based algorithms can automate parts of visual inspection, increasing efficiency and accuracy while reducing the time and cost of manual inspections [28].

2.2 Ultrasonic Testing (UT)

Another most preferred method is ultrasonic testing. This is a form of inspection that uses the propagation of ultrasound waves inside materials, Figure 2. The analysis of reflections due to abnormalities in the internal structure allows the measurement of properties such as thickness or the depth of any defect. Although advanced ultrasonic tools provide 3D C-scan and cross-sectional B-scan to obtain sufficient information about a structure, quantifying and locating defects can be challenging and multiple tests may be necessary [18].

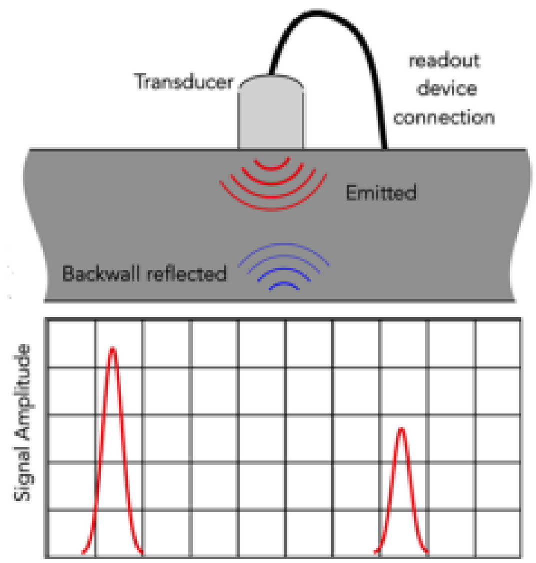

Figure 2. Schematic representation of the ultrasonic test method

Ultrasonic Testing (UT) is an important NDT method used especially in the aerospace industry. The basic principle of UT is to detect internal defects such as delaminations and disbonds that could compromise structural integrity. For this, it transmits high-frequency sound waves into the material [29, 30]. The accuracy and reliability of UT in sandwich composite materials are higher than other NDT methods such as X-ray or penetrant testing [31, 32].

Composite materials, including carbon fiber-reinforced plastics (CFRPs) and glass fiber-reinforced plastics (GFRPs), are susceptible to various defects throughout their production and service life. These defects can significantly affect the mechanical properties and overall performance of the materials [10, 33]. Therefore, these materials need to be continuously monitored and evaluated. It plays an important role, especially in sectors where safety is at the forefront of applications such as the aerospace and automotive industries [34]. Advances in ultrasonic techniques improve detection capabilities by increasing resolution and imaging quality. This facilitates the identification of defects that might otherwise go unnoticed [35].

The Ultrasonic Testing (UT) method consists of a transmitter and receiver circuit, a transducer tool, and imaging devices. By looking at the information carried by the signal, flaw size, orientation, and crack location can be determined. The advantages of ultrasonic testing include flaw detection capabilities, scanning speed, and good resolution. This makes it suitable for use in the field. The disadvantages are the skill required to scan the part accurately and the difficulty of setup. There are two different ultrasonic NDT methods used in different applications; the pulse echo and transmission approach. Both methods use high-frequency sound waves in the range of 1-50 MHz to detect defects within the material. In this method, testing is performed in three modes: transmission, reflection, and backscattering. Each of these uses a range of transducers, coupling agents, and frequencies [8].

Recent studies have shown that ultrasonic testing is applied in combination with thermography to provide a more comprehensive and reliable evaluation of composite materials. Thermography is another NDT technique. For example, the use of ultrasonic techniques with infrared thermography enables the effective detection of subsurface defects by visualizing the thermal responses associated with material anomalies [15]. Furthermore, the development of sophisticated signal processing techniques for ultrasonic data analysis has further enhanced the capabilities of UT in composite materials. These developments enable better interpretation of ultrasonic signals, allowing for more precise detection and localization of defects [35].

2.3 Infrared Thermography Testing (IRT)

The first studies on IRT were done on metal test specimens. It was not a suitable method for testing composite materials. However, nowadays it can detect many defects in composite materials including impact damage, delamination, rupture, etc. [5]. Thermography testing is a thermal imaging method. The thermal conductivity of a material can vary depending on the depth and size of the defect in it. Thermography inspection is often effective in the handling of thin parts. This is because it produces fewer heat fluctuations if the defects present are far below the surface of a part. Usually, deeper and smaller defects cannot be detected. A defect in the material, such as delamination or impact damage, causes a change in the thermal radiation of the area [8]. Infrared thermography (IRT) is one of the NDT methods and was developed to reveal defects in materials. This method is used to detect delaminations, cracks, and other subsurface defects that can compromise structural integrity. It uses thermal radiation emitted from the surface of materials to do this. The advantages of IRT include rapid inspection and the ability to examine large areas without direct contact with the material being tested [13].

Infrared Thermography uses a heat source and causes short thermal stress on the material. Thermal waves propagate on the surface of the sample. When these waves hit a different surface, the propagation is distorted and a thermal gradient is created. In this way, different emissivity coefficients are created and these are captured by an IR sensor. An InfraRed camera used in the setup allows the emissivity coefficient to be converted to temperature. Thermal two-dimensional mapping is created and inhomogeneous regions are detected [5]. When thermal energy diffuses through a material and reaches a crack, delamination, or pore, a thermal gradient is generated due to the different emissivity coefficients that can be used to interpret the damage. An infrared camera detects the heat emitted from the material, and this information is used to create a map showing the temperature differences on the surface of the structure, Figure 3. Infrared thermography can be used to find defects in composite materials, especially those with different thermal properties. NASA has been using this method to inspect spacecraft for years. Researchers are also using it to quickly inspect parts, engines, and turbines of aircraft and spacecraft. Research is still ongoing on thermography techniques that use automated scanning with robots to inspect large composite structures [12].

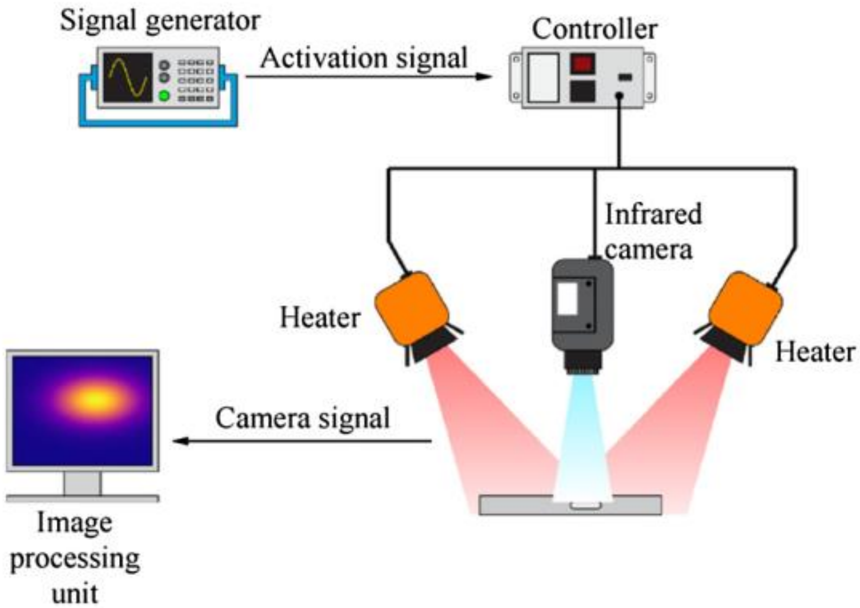

Figure 3. Schematic illustration of IRT

Infrared thermal imaging examination techniques are classified as active or passive. If an external energy source is used for imaging, it is called active IRT. If no external energy source or stimulus is used, it is called passive IRT [36]. Active infrared thermography, which uses an external heat source to excite the material, is effective at identifying various types of defects in composite materials. For instance, studies have shown that active IRT can successfully detect flat bottom holes (FBHs) and delaminations in carbon fiber-reinforced polymers (CFRP) [9, 37]. The effectiveness of the technique is further enhanced by advanced post-processing techniques that improve defect visualization and characterization [37]. The passive IRT technique can perform in situ analysis using the natural thermal emissions of the material. For example, this technique can be used to examine wind turbine blades without an external heating source [9].

The IRT technique is also used to detect complex defects and monitor the structural integrity of composite materials under various loading conditions. For example, studies have shown that IRT can detect fatigue damage and crack propagation in ceramic matrix composites. It can also provide insight into the remaining life of materials subjected to cyclic loads [38, 39]. This predictive capability is vital for industries such as aerospace, where the integrity of composite components is critical for safety and performance [39].

Moreover, the integration of IRT with other NDT methods such as acoustic emission (AE) has been investigated to improve detection capabilities. This new technique allows for a more comprehensive assessment of damage mechanisms in composite materials [39]. The versatility of IRT is used to monitor structural integrity and detect defects in critical components, so it is used in a variety of fields including civil engineering, aerospace, and automotive industries [40, 41].

2.4 Acoustic Emission (AE)

Acoustic Emission (AE) technology is an NDT method used to detect the integrity and damage mechanisms of composite materials. This technique is particularly used to detect internal damages that occur during mechanical loading, such as matrix cracking, fiber breakage, and delamination [42-44]. The AE method detects transient elastic waves generated by the rapid release of energy from localized sources within the material, allowing for continuous monitoring of damage progression [45].

One of the major challenges in applying AE to composite materials is their anisotropic nature, which makes the interpretation of AE signals difficult. To address this, Modal Acoustic Emission (MAE) was developed, which treats AE signals as mechanical waves propagating in the composite in various modes. This allows for more comprehensive insights into damage mechanisms. This approach improves the qualitative and quantitative analysis of AE data, making it particularly useful for thin composite structures under tensile stress [46]. Acoustic emission (AE) tests are not exactly repeatable due to the nature of the signal source. Each AE event is a different stress wave. For example, a slow crack growth will produce a weak AE signal, while a fast crack growth of the same size will produce a transient signal [12]. In the Acoustic Emission (AE) method, mechanical vibration is generated by material defects such as fiber-matrix separation, local delamination, or matrix microcracking in the material. The resulting stress waves propagate through the material and are detected by the sensitive piezoelectric [8].

Acoustic emission (AE) can be used to evaluate the burst pressure of composite pressure vessels. Wang et al. (2021) investigated the relationship between the damage behavior (matrix cracking, fiber/matrix separation, fiber breakage) of hydrogen storage pressure vessels using AE signals during hydrostatic burst tests with multi-stage loading. The burst test using acoustic and optical sensors can be used to obtain the actual burst pressure and damage behavior of composite vessels [47, 48]. The AE method is a reliable and real-time technique for early detection of transient stress waves in materials. Although this technique is quite sensitive to small changes in dynamic defects, it may not be as sensitive to static defects. AE is more suitable for electrical defects rather than mechanical defects. It may also have deviations in the size and orientation of the defects within the material [18].

The application of AE technology is also used in various types of composites, including carbon fiber reinforced polymers (CFRP) and glass fiber composites. Studies have shown that AE can effectively detect damage under different loading conditions, including low-velocity impacts and quasi-static tension tests [43, 44, 49]. For example, Mahdian et al. (2016) highlighted that the AE technique can detect multiple failure modes in laminated composites subjected to impact [44]. Similarly, the study by Fotouhi et al. (2015) highlighted the effectiveness of AE in detecting delamination growth in sandwich composites, demonstrating its superiority over conventional NDT methods [50].

The integration of advanced signal processing techniques, such as Fast Fourier Transform (FFT) and wavelet analysis, has further enhanced the capability of AE in identifying and characterizing damage mechanisms [51]. These methods allow for more detailed analysis of acoustic signals and facilitate the identification of specific failure modes, thereby increasing the reliability of the testing technique [52].

3. CONCLUSIONS

Composite materials are widely used in aerospace, automotive, and civil engineering industries. Therefore, NDT methods are an important testing technique in ensuring the reliability and structural integrity of composite materials. NDT testing techniques are performed without damaging the material. In this study, the most commonly used Visual Testing (VT) and Visual Inspection (VI), ultrasonic inspection (UT), infrared thermography (IRT), and acoustic emission (AE) methods are included.

Visual Inspection (VT) and Visual Inspection (VI): Visual Inspection (VT/VI) is a basic and cost-effective technique for detecting surface defects such as cracks and imperfections. However, the disadvantage of the method is that it cannot detect subsurface or internal defects, making it inadequate for comprehensive material evaluation.

Ultrasonic Testing (UT): To overcome the limitations of the visual inspection (VT/VI) technique, Ultrasonic Testing (UT) is used. This method is one of the most widely used techniques to detect internal defects such as delaminations and fiber breakage. The high sensitivity of UT makes it an important method for assessing the structural integrity of composite materials. However, the efficiency of this method depends on the acoustic properties of the material. Also, complex geometries are another limitation of this method.

Infrared Thermography (IRT): It is a non-contact inspection technique that is particularly suitable for detecting surface and near-surface defects. IRT detects inconsistencies in material structures by analyzing thermal gradients. However, its ability to penetrate deeply is limited, and external factors such as ambient temperature can affect its accuracy.

Acoustic Emission (AE): Acoustic Emission (AE) is a dynamic technique that allows real-time monitoring of damage progression. It is particularly useful for assessing the response of a material under load, making it suitable for detecting active damage mechanisms. However, AE requires advanced signal processing, interpretation, and experience, which can make its application difficult.

Each NDT technique has its advantages and limitations. The method chosen should be determined by the material properties and inspection requirements. Combining multiple NDT techniques with advances in artificial intelligence (AI) and automated inspection systems can increase defect detection accuracy and efficiency. Future research can enhance the capabilities of NDT technologies through the development of hybrid techniques, improved data analysis methods, and real-time monitoring solutions.

Consequently, NDT methods for composite materials are important for defect detection and the detection of structural changes. Various NDT techniques, such as ultrasonic testing, infrared thermography, acoustic emission, and visual inspection, are frequently used to test the integrity and reliability of composite structures.

REFERENCES

[1] P. H. Chen *et al.*, "Thickness Measurement of Composite Material Using Eddy Current Testing," *Advanced Materials Research*, vol. 79–82, pp. 1995–1998, 2009.

[2] Y. A. Fakhrudi, K. N. Faidzin, and R. M. Bisono, "Effect of Composite Composition on Mechanical Properties of Banana Fiber Composites With Epoxy Matrix for Functional Materials," *International Journal of Science Engineering and Information Technology*, vol. 6, no. 2, pp. 303–306, 2022.

[3] M. H. Boztepe, "Effect of surface treatments and stacking sequences on the mechanical properties of fiber metal laminates," M.S. thesis, Dept. Mechanical Engineering, Cukurova University, 2022.

[4] B. Wang *et al.*, "Non-destructive testing and evaluation of composite materials/structures: A state-of-the-art review," *Advances in Mechanical Engineering*, vol. 12, no. 4, p. 1687814020913761, 2014.

[5] C. Garnier *et al.*, "The detection of aeronautical defects in situ on composite structures using Non Destructive Testing," *Composite Structures*, vol. 93, no. 5, pp. 1328–1336, 2011.

[6] W. Zhou *et al.*, "Review on the performance improvements and non-destructive testing of patches repaired composites," *Composite Structures*, vol. 263, p. 113659, 2021.

[7] N. Saha, P. Roy, and P. Topdar, "Damage detection in composites using non-destructive testing aided by ANN technique: A review," *Journal of Thermoplastic Composite Materials*, vol. 36, no. 12, pp. 4997–5033, 2023.

[8] S. Gholizadeh, "A review of non-destructive testing methods of composite materials," *Procedia Structural Integrity*, vol. 1, pp. 50–57, 2016.

[9] C. Galleguillos *et al.*, "Thermographic Non-Destructive Inspection of Wind Turbine Blades Using Unmanned Aerial Systems," *Plastics Rubber and Composites Macromolecular Engineering*, vol. 44, no. 3, pp. 98–103, 2015.

[10] K. Ciecieląg *et al.*, "Non-Destructive Detection of Real Defects in Polymer Composites by Ultrasonic Testing and Recurrence Analysis," *Materials*, vol. 15, no. 20, p. 7335, 2022.

[11] V. Acanfora *et al.*, "On the Use of Digital Image Correlation to Assess the Damage Behavior of Composite Coupons Under Compression," *Macromolecular Symposia*, vol. 404, no. 1, 2022.

[12] H. Towsyfyan *et al.*, "Successes and challenges in non-destructive testing of aircraft composite structures," *Chinese Journal of Aeronautics*, vol. 33, no. 3, pp. 771–791, 2020.

[13] Y. Liu *et al.*, "Independent Component Thermography for Non-Destructive Testing of Defects in Polymer Composites," *Measurement Science and Technology*, vol. 30, no. 4, p. 044006, 2019.

[14] J. S. Bale *et al.*, "Damage Observation of Glass Fiber/Epoxy Composites Using Thermography and Supported by Acoustic Emission," *Applied Mechanics and Materials*, vol. 627, pp. 187–190, 2014.

[15] W. Świderski and M. Pracht, "Non-Destructive Evaluation of Composite Helmets Using IR Thermography and Ultrasonic Excitation," *Pomiary Automatyka Robotyka*, vol. 25, no. 4, pp. 89–92, 2021.

[16] N. Tao, A. G. Anisimov, and R. M. Groves, "Spatially Modulated Thermal Excitations for Shearography Non-Destructive Inspection of Thick Composites," 2021, p. 29.

[17] A. Gokul, S. Kuchipudi, and J. Dhanasekaran, "Inspection of Profiled Frp Composite Structures by Microwave NDE," *International Journal of Microwave Engineering*, vol. 5, 2020.

[18] M. E. Torbali, A. Zolotas, and N. P. Avdelidis, "A State-of-the-Art Review of Non-Destructive Testing Image Fusion and Critical Insights on the Inspection of Aerospace Composites towards Sustainable Maintenance Repair Operations," *Applied Sciences*, vol. 13, no. 4, p. 2732, 2023.

[19] Z. Li and Z. Meng, "A Review of the Radio Frequency Non-destructive Testing for Carbon-fibre Composites," *Measurement Science Review*, vol. 16, no. 2, pp. 68–76, 2016.

[20] N. Guillaud *et al.*, "Impact Response of Thick Composite Plates Under Uniaxial Tensile Preloading," *Composite Structures*, vol. 121, pp. 172–181, 2015.

[21] D. Mascareñas *et al.*, "Augmented Reality for Next Generation Infrastructure Inspections," *Structural Health Monitoring*, vol. 20, no. 4, pp. 1957–1979, 2020.

[22] M. Waqar *et al.*, "Composite pipelines: Analyzing defects and advancements in non-destructive testing techniques," *Engineering Failure Analysis*, vol. 157, p. 107914, 2024.

[23] D. Findeis, J. Gryzagoridis, and C. Lombe, "Comparing Infrared Thermography and ESPI for NDE of Aircraft Composites," *Insight - Non-Destructive Testing and Condition Monitoring*, vol. 52, no. 5, pp. 244–247, 2010.

[24] H. J. Shin and J. R. Lee, "Development of a Long-Range Multi-Area Scanning Ultrasonic Propagation Imaging System Built Into a Hangar and Its Application on an Actual Aircraft," *Structural Health Monitoring*, vol. 16, no. 1, pp. 97–111, 2016.

[25] A. Sellitto *et al.*, "Ultrasonic Damage Detection of Impacted Long and Short Fibre Composite Specimens," *Key Engineering Materials*, vol. 827, pp. 31–36, 2019.

[26] A. Bondyra and P. D. Pastuszak, "3D Scanning Inspection of the Composite Structures," *Journal of Kones Powertrain and Transport*, vol. 21, no. 1, pp. 31–36, 2014.

[27] R. Růžek *et al.*, "CFRP Fuselage Panel Behavior Monitoring Using Fibre Optic and Resistance Sensors and Optical Contactless Measurements," *Applied Mechanics and Materials*, vol. 827, pp. 51–56, 2016.

[28] S. Sundaram and A. Zeid, "Artificial Intelligence-Based Smart Quality Inspection for Manufacturing," *Micromachines*, vol. 14, no. 3, p. 570, 2023.

[29] P. Theodorakeas *et al.*, "Comparative Evaluation of Aerospace Composites Using Thermography and Ultrasonic NDT Techniques," 2015, vol. 9485, p. 948504.

[30] N. H. Gandhi *et al.*, "Understanding System Complexity in the Non-Destructive Testing of Advanced Composite Products," *Journal of Manufacturing and Materials Processing*, vol. 6, no. 4, p. 71, 2022.

[31] L. Mezeix and K. Wongtimnoi, "Non Destructive Testings on Damaged Multi-Cores Materials Sandwich Structures," 2020, p. 13.

[32] G. S. LeMay and D. Askari, "A New Method for Ultrasonic Detection of Peel Ply at the Bondline of Out-of-Autoclave Composite Assemblies," *Journal of Composite Materials*, vol. 53, no. 2, pp. 245–259, 2018.

[33] A. D. Abetew *et al.*, "Parametric Optimization of Pulse-Echo Laser Ultrasonic System for Inspection of Thick Polymer Matrix Composites," *Structural Health Monitoring*, vol. 19, no. 2, pp. 443–453, 2020.

[34] C. Casavola *et al.*, "Analysis of CFRP Joints by Means of T-Pull Mechanical Test and Ultrasonic Defects Detection," *Materials*, vol. 11, no. 4, p. 620, 2018.

[35] Y. Humeida *et al.*, "Simulation of Ultrasonic Array Imaging of Composite Materials With Defects," *IEEE Transactions on Ultrasonics Ferroelectrics and Frequency Control*, vol. 60, no. 9, pp. 1935–1948, 2013.

[36] Y. She *et al.*, "Nano-Additive Manufacturing and Non-Destructive Testing of Nanocomposites," *Nanomaterials*, vol. 13, no. 20, p. 2741, 2023.

[37] G. Poelman *et al.*, "Optical Infrared Thermography of CFRP With Artificial Defects: Performance of Various Post-Processing Techniques," 2018, p. 457.

[38] K. G. Dassios and T. E. Matikas, "Assessment of Fatigue Damage and Crack Propagation in Ceramic Matrix Composites by Infrared Thermography," *Ceramics*, vol. 2, no. 2, pp. 393–406, 2019.

[39] K. G. Dassios *et al.*, "Crack Growth Monitoring in Ceramic Matrix Composites by Combined Infrared Thermography and Acoustic Emission," *Journal of the American Ceramic Society*, vol. 97, no. 1, pp. 251–257, 2013.

[40] G.-W. Hong *et al.*, "The Evaluation of Bimaterial Specimen With FDM 3D Printing Technology by Infrared Thermography," 2017.

[41] R. Andoga *et al.*, "Intelligent Thermal Imaging-Based Diagnostics of Turbojet Engines," *Applied Sciences*, vol. 9, no. 11, p. 2253, 2019.

[42] W. Wang *et al.*, "Investigation on the Behavior of Tensile Damage Evolution in T700/6808 Composite Based on Acoustic Emission Technology," *Shock and Vibration*, vol. 2016, p. 1–9, 2016.

[43] Y. Zhang, W. Zhou, and P.-F. Zhang, "Quasi-Static Indentation Damage and Residual Compressive Failure Analysis of Carbon Fiber Composites Using Acoustic Emission and Micro-Computed Tomography," *Journal of Composite Materials*, vol. 54, no. 2, pp. 229–243, 2019.

[44] A. Mahdian *et al.*, "Damage Evaluation of Laminated Composites Under Low-Velocity Impact Tests Using Acoustic Emission Method," *Journal of Composite Materials*, vol. 51, no. 4, pp. 479–490, 2016.

[45] I. Silversides, A. Maslouhi, and G. LaPlante, "Acoustic Emission Monitoring of Interlaminar Delamination Onset in Carbon Fibre Composites," *Structural Health Monitoring*, vol. 12, no. 2, pp. 126–140, 2013.

[46] M. H. Zohari, J. Epaarachchi, and K.-T. Lau, "Modal Acoustic Emission Investigation for Progressive Failure Monitoring in Thin Composite Plates Under Tensile Test," *Key Engineering Materials*, vol. 558, pp. 65–75, 2013.

[47] D. Wang *et al.*, "Acoustic emission characteristics of used 70 MPa type IV hydrogen storage tanks during hydrostatic burst tests," *International Journal of Hydrogen Energy*, vol. 46, no. 23, pp. 12605–12614, 2021.

[48] W. Zhou *et al.*, "Review on optimization design, failure analysis and non-destructive testing of composite hydrogen storage vessel," *International Journal of Hydrogen Energy*, vol. 47, 2022.

[49] P. Liu, J. Yang, and X. Peng, "Delamination Analysis of Carbon Fiber Composites Under Hygrothermal Environment Using Acoustic Emission," *Journal of Composite Materials*, vol. 51, no. 11, pp. 1557–1571, 2016.

[50] M. Fotouhi *et al.*, "Investigation of the Damage Mechanisms for Mode I Delamination Growth in Foam Core Sandwich Composites Using Acoustic Emission," *Structural Health Monitoring*, vol. 14, no. 3, pp. 265–280, 2015.

[51] N. Beheshtizadeh and A. Mostafapour, "Characterization of Carbon Fiber/Epoxy Composite Damage by Acoustic Emission Using FFT and Wavelet Analysis," *Advanced Engineering Forum*, vol. 17, pp. 77–88, 2016.

[52] R. Mohammadi *et al.*, "A Quantitative Assessment of the Damage Mechanisms of CFRP Laminates Interleaved by PA66 Electrospun Nanofibers Using Acoustic Emission," *Composite Structures*, vol. 258, p. 113395, 2021.

ALKU Journal of Science 2024, Sayı 7(1): 55-65
e-ISSN: 2667-7814

Original

Experimental Research of Waste PET and Foundry Sand Recycling Into Bricks

Nigar Sezen BAL[1*], **Sevim YOLCULAR**[1]
[1]*Kimya Mühendisliği, Ege Üniversitesi, İzmir, Türkiye.*
**balsezen29@gmail.com*

Abstract

In this study, the aim is to produce Polyethylene terephthalate-sand bricks that are more durable, lighter, more economical, have less water absorption, and thermal conductivity compared to clay bricks by using waste Polyethylene terephthalate and waste foundry sand in different proportions. After the bricks were produced at different ratios; in three-point bending test, the brick with the highest percentage of Polyethylene terephthalate, S1, has the highest maximum stress (17.04 MPa), impact test result shows that S1 (1:2) and S2 (1:3) are impact-resistant bricks, in the water absorption test, S1 (1:2) has the lowest water absorption with 0.35%, lastly, in thermal conductivity test, the red brick had the lowest thermal conductivity with 0.713 W/mK. All bricks produced in different proportions weigh less than red bricks. Moreover, since the production of Polyethylene terephthalate-sand bricks does not require a long-term and high-temperature kiln, energy savings are provided, and the production of Polyethylene terephthalate-sand is more economical.

Keywords: Recycle, Polyethylene terephthalate, brick, foundry sand, sustainable construction material

Atık PET ve döküm kumunun tuğla olarak geri dönüştürülmesinin deneysel araştırması

Özet

Bu çalışmada, atık Polietilen tereftalat ve atık döküm kumunu farklı oranlarda kullanarak kil tuğlalara göre dayanıklı, hafif, ekonomik, daha az su emme ve ısı iletkenliğine sahip Polietilen tereftalat-kum tuğlaları üretmek amaçlanmıştır. Farklı kum/ Polietilen tereftalat karışım oranlarında tuğlalar üretildikten sonra fiziksel ve mekanik özellikleri kırmızı tuğlalarla kıyaslanmıştır. Sonuçta; üç nokta eğme deneyinde, en yüksek Polietilen tereftalat oranına sahip tuğla olan S1, maksimum gerilmeye (17.04 MPa) sahip olmuş, darbe testi sonucu S1 (1:2) ve S2 (1:3)'nin darbeye dayanıklı tuğlalar olduğunu, su emme deneyinde S1 (1:2)'in %0.35 ile en düşük su emme değerine sahip olduğunu, son olarak ısı iletkenlik deneyinde ise kırmızı tuğlanın 0.713 W/mK ile en düşük ısı iletkenliğine sahip olduğunu göstermiştir. Farklı karışım oranlarında üretilen tüm tuğlalar, kırmızı tuğlalardan daha az ağırlığa sahiptir. Ayrıca, Polietilen tereftalat-kum tuğlaların üretimi uzun süreli ve yüksek sıcaklıkta fırın gerektirmediğinden enerji tasarrufu sağlanmakta ve Polietilen tereftalat-kum üretimi daha ekonomik olmaktadır.

Anahtar Kelimeler: Geri dönüşüm, Polietilen tereftalat, tuğla, döküm kumu, sürdürülebilir inşaat malzemesi

1. INTRODUCTION

Plastics are one of the most useful inventions of the last century that make human life easier. They are cheap, durable, and lightweight materials that can be molded into a variety of products. They are used in many applications, including furniture, packaging, electronic materials, automotive, medical devices, industrial components, and so on. However, this situation becomes a disadvantage when these items are thrown away. The major problem is that plastics have non-biodegradable characteristics, and waste mismanagement leads to damage to the environment. In addition, since plastics cannot be broken down by bacteria, they do not decompose easily, and it takes between 20 and 600 years to decompose in nature. Therefore, as the use of plastics has increased over the years, there has been a dramatic increase in the volume of landfills. There have been many ways to overcome this problem, such as incineration, recycling, chemical, physical, and biological treatment, etc. In fact, recycling is one of the most important actions to take to solve this problem. Moreover, plastics can be blended with many materials. Recycling plastic items into new goods helps the environment, reduces plastic material production from petroleum, emissions of greenhouse gases, landfill volume, and creates new economic opportunities.

Among all plastic types, one of the most commonly used materials is polyethylene terephthalate. Polyethylene terephthalate, also known as PET, is a type of plastic that is strong, lightweight, recyclable, and has transparent, amorphous thermoplastic characteristics. PET is formed as a result of the polycondensation of ethylene glycol and terephthalic acids [1]. Blow molding, extrusion, and injection molding methods are used to produce products containing PET. PET is widely manufactured for packaging foods, beverages, water, cooking oils, shampoo, liquid hand soap, shopping bags, textiles, containers, etc. [2].

As mentioned before, PET is a recyclable material and can be recycled in many ways. New products are manufactured by using either all of the recycled PET or by mixing some of it with virgin one. This recycled PET can also be mixed with other types of plastic or non-plastic materials as well. In order to reuse PET, there are physical and chemical recycling methods applied in many parts of the world. In the physical recycling of PET, items that are made of PET are collected and sent to sorting centers, where they are sorted and squashed into bales to make the transportation easy to be sent to recycling plants. When waste PET enters the recycling process, in the first step, it is separated from any metal parts inside by using a magnet. Then, they are washed to remove the labels and glue. In order to not let non-PET go further, optical and manual sorting are done. After that, the items are sent to a grinder and grinded into flakes. The flakes go through various sorting machines to be separated according to their colors. The flakes are then dried, melted, filtered, and cut into pellets, ready to be reused. On the other hand, in chemical recycling, PET can be converted to monomers by complete depolymerization or to oligomers and other products by partial depolymerization. The monomers are then repolymerized, and these polymers are formed into new products. These polymers, regenerated monomers, or both may be blended with virgin materials. There are some methods for chemical recycling of waste PET, and most of them consist of esterifying polyester with an excess of reactants such as alcohols, diamines, diols, or water.

Moreover, there are lots of benefits to recycling PET bottles. First of all, the use of PET bottles is growing as the population increases over the years. This causes accumulation in landfill areas, which is a significant problem for the environment. Sales of bottled water have been steadily increasing, from 8.76 billion gallons sold in 2010 to 15.3 billion gallons in 2021 [3]. As the consumption of these bottles increases, the volume of waste will increase; therefore, recycling is a good solution for accumulation. Secondly, recycling PET reduces the amount of energy and resources that are needed to create PET. According to Stanford University (2023), recycling one ton of plastics provides 16.3 barrels of oil and 5.774 kWh of energy savings, which is enough to run an average household for months [4]. Thirdly, PET accumulation and the manufacturing process of PET bottles are major threats to ecosystems in an environmentally harmful manner. 90 percent of the waste that is seriously harmful and found on the surface of the oceans consists of plastic, which makes about 46,000 parts of plastic per square mile [5]. Every year, thousands of marine animals and seabirds die due to plastic pollution [6]. Finally, recycled

PET can be used in many areas, such as construction, textiles, and toys. Recycling supports businesses in developing innovative products and creates job opportunities for people. The effort that people make and the developments in the recycling industry have made huge differences in decreasing the volume of landfills and, therefore, pollution in the soil and ocean.

In addition to the waste plastic concern, there has been another waste problem for years: used foundry sand (FS). Virgin sand is purchased by foundries in order to make molds for metal casting, and in the manufacturing process, sand is reused repeatedly. Approximately 1 ton of foundry sand is used for each ton of metal production [7]. Reusing the sand eventually renders it inconvenient for casting. The grains of the sand begin to break down due to heat and mechanical abrasion, and it loses its uniformity and cleanliness; therefore, new sand must be added to the unit to maintain proper casting. The waste sand has to be recycled; otherwise, it is sent to landfills. Foundry sand recycling reduces virgin material mining and saves energy. The waste foundry sand can be safely and economically recycled and used in many fields, such as manufacturing soil plants, in soilless mediums, and as an additive for roads.

Many studies have developed various methods for recycling waste. One of the literature suggestions is to recycle waste plastic and foundry sand for construction. In this field, the primary material is bricks that are made of clay. The procedures for making traditional bricks are mixing, molding, drying, and firing at a temperature between 1000 °C and 1100 °C [8]. However, the soil material usage puts stress on the soil and therefore causes soil erosion, which leads to high energy consumption in production. Moreover, the emission of greenhouse gases causes acid rain, climate change, and global warming. The bricks that are made of plastic and sand reduce waste, which is a sustainable and ecological development. The advantages of thermoplastic waste aggregates are lower production costs, a lighter product because of the recycled plastics' lower specific gravity, greater flexibility in design, a lower dead load on the structure, and enhanced thermal insulation, which is important for energy conservation. Nowadays, commercial-level applications have been made by entrepreneurs in brick-making. These bricks are expected to have better properties than commercial bricks. These features include being more durable, lighter, and cheaper, having less water absorption, and having less thermal conductivity. Several developing countries have established factories to produce bricks that are made of plastic in order to clean the environment and provide affordable alternative construction materials.

In Argentina, Ecoinclusion was founded to solve environmental problems. They work for the reduction of PET bottle waste through the production of bricks made of plastic residues for use in the construction sector [9]. They started to manufacture eco-friendly bricks that consist of waste PET, cement, and different additives. To produce one brick, 1 kilogram (20 bottles) of recycled plastic is needed. The bricks are lighter and have better insulating and sound-proofing properties than red bricks [10]. They have a technical certification that is granted by the UN-Habitat Secretariat and were patented by Ceve-Conicet. In 2017, Ecoinclusion won the Google.org challenge [9].

In India, the casting industry causes millions of metric tons of dumped waste, which is hazardous for the environment [11]. An Indian company called Rhino Machines makes silica plastic blocks from plastic waste and recycled sand. These bricks are made of 20% mixed plastic waste and 80% recycled sand waste/foundry dust. The conventional bricks that we use for daily construction activities fall apart when they are disintegrated into smaller sizes; however, silica plastic bricks keep their shape and strength even after you drill a hole in them [12]. The cost of production will be relatively low. The mixed plastic waste was used as a bonding agent. The bricks were 2.5 times stronger than the commercial red clay bricks, and 80% less natural resources were used. Moreover, the other best thing about Rhino bricks is that they are cheaper than commercial bricks [13].

Another example is Gjenge Makers Ltd, which produces plastic-sand bricks as well. In Kenya, they started designing machines for recycling plastic waste into bricks [14]. High-density polyethylene and low-density polyethylene are used for production. The result is a brick that is 5 to 7 times stronger than concrete, weighs half as much, and therefore reduces CO_2 emissions and logistics costs. The positive results of brick production include increased income for garbage collectors, a stronger construction industry due to more affordable materials, a contribution to the circular economy, and fewer CO_2 emissions during transportation.

In another study, single-use surgical masks were used to solve the plastic pollution problem. The recycled surgical masks were mixed with ground granulated blast furnace slag, ash, sand, rice husk, and sodium silicate. The bricks were then tested for water absorption, compressive strength, flexural strength, efflorescence, density, and drying shrinkage. The results show that the recycled surgical masks in the bricks improved compressive strength and flexural strength. Additionally, with the increase in recycled surgical masks, there was a decrease in the brick weight. The recycled surgical masks reduced the drying shrinkage of the bricks. However, there was no significant effect on the water absorption or properties of recycled surgical masks [15].

In this thesis study, the aim is to produce PET-sand bricks that are more durable, lighter, more economical, have less water absorption, and have less thermal conductivity compared to red bricks that are made of clay by using waste PET and FS in different proportions. Waste PET and foundry sand were chosen as ingredients since PET is one of the most wasted materials in the world, and waste foundry sand is a major problem for casting factories. The importance of the thesis is to reduce the volume of waste PET and foundry sand in landfills by recycling them into bricks and trying to reduce environmental pollution to some extent. In the experiments, the bricks were produced at different rates and subjected to three-point bending, impact, water absorption, and thermal conductivity tests. After the tests, the results are compared first among the PET bricks with different ratios and then with the red brick.

2. MATERIALS AND METHODS

2.1 Materials

In the production of the PET-sand bricks, PET and FS were mixed in different proportions. The ratio of sample 1 (S1) is 1:2, the ratio of sample 2 (S2) is 1:3, and the ratio of sample 3 (S3) is 1:4 according to the PET:FS. The reason behind taking different proportions is to find the optimum results while investigating various properties. After the experiments, the produced PET-sand bricks will be compared with red bricks. The size of the shredded pieces varied from 2–5 mm in length and 1–3 mm in width. The thickness of the shredded pieces was less than 1 mm. The components of foundry sand are 85% silica sand, 10% bentonite, and 5% coal dust. Its particle size distribution varies between 0.075 and 0.600 mm. The clay brick components are 75% SiO_2, 16% Al_2O_3, 5% K_2O, 1.25% Na_2O, 0.96% FeO, 0.25% CaO, 0.25% MgO, and 0.15% TiO_2. Their usage areas are pedestrian and light vehicle traffic floors. Its dimensions are 210 mm x 105 mm x 40 mm. The average weight of the brick is 1.900 kg.

2.2 Instruments

In the production of the PET-sand bricks, PET and FS are heated separately. A granite-covered container, a steel container, and a metal thermometer are used in the experiment. The granite-covered container is used as a drum to prevent the hot mixture from sticking to the container. The steel container is used for heating the sand. Both containers are heated on a gas stove and mixed with wooden mixers. Wooden material is used due to its low thermal conductivity. A metal thermometer that is capable of measuring up to 300 °C is used to measure the temperatures during the process. The molds for the bricks are made of medium-density fiberboard. Waxed paper is used inside the mold to avoid contact between the mixture and the mold surface. The size of the mold is 210 mm x 105 mm x 40 mm, which has the same dimensions as the red brick to give precise results. For the three-point flexural test, a 210 mm x 55 mm x 40 mm mold is used.

2.3 Methods

In the first step, PET powder and sand are weighed in certain proportions for the bricks that have different proportions. In the heating and mixing process, while the waste PET powder is heated in the granite-covered pan, the FS is heated in the steel container as well. PET is allowed to melt and is continuously mixed in the temperature range of 220-270 °C. After the PET is completely melted, the heated FS is gradually added to the container and mixed with the PET continuously. When the mixture becomes homogeneous, it will be ready to be filled into the molds. The mixture is filled into the molds, which are covered with waxed paper in order to avoid sticking to the mold itself. Lastly, the lid is placed on the mold, and a weight of 100 kg is placed on the lid, allowing the mixture to pass into each other with pressure, and it is left to cool for about 5 hours.

2.4 Tests

After the production of the bricks with different ratios, they will first be weighed to be able to compare them with the red brick's weight. Then, the products were tested for three-point flexural, impact, water absorption, and thermal conductivity. They will be compared among themselves and with the red brick. The three-point flexural tests will be done at the Central Research Test and Analysis Laboratory Application and Research Center at Ege University, and the thermal conductivity tests will be done at the Mechanical Engineering Laboratory at İzmir Katip Çelebi University.

2.4.1 The Three-point Flexural Test

The three-point flexural test is a standard test method for bricks and structural clay tiles. The purpose of the test is to find the resistance of the brick to bending through the internal stresses in the brick structures. The loading and support noses, which are cylindrical materials, have a diameter of 30 mm and a length of 60 mm. Since the size of the bricks should fit the testing machine, the size of both red brick and PET-sand was reduced to 210 mm x 5-6 mm x 4-5 mm. Therefore, a smaller mold for the PET-sand brick was made, and the red brick was cut in half for this test. In a three-point flexural test, the dimensions of the bricks are measured. The locations where the load will be applied under three-point bending are marked, and the length between the supports is noted. The servo controller device that is shown will be used for operating the tests. Loading is applied continuously until failure, and the maximum load is recorded. After the failure, a stress vs. stroke graph is drawn. Lastly, the results are compared first among the PET bricks with different ratios and then with the red brick. The aim is to test the samples for elastic modulus in bending, stress-strain behavior, and failure limits in bending.

2.4.2 The Impact Test

An impact test aims to certify the proper bonding of a brick so that it cannot be damaged easily. If the brick is damaged or broken, it means that its impact value is low. The impact test will be considered a failure and not acceptable for construction work. If it is not broken, it is considered a good-quality brick. In this test, each brick is forced to break by free falling from 1 meter. The bricks are checked for falling to pieces. If any, the number of pieces is noted. The results are compared first among the PET bricks with different ratios and then with the red brick. The aim of the test is to find the brick that does not break or is the least fragmented.

2.4.3 The Water Absorption Test

The water absorption test gives the quantity of water being absorbed by bricks. The aim of the test is to find out which brick has the lowest absorbed water because it decreases the durability of the brick. The results of this test show the bonding of the mortar to the brick. After cooling every brick to room temperature, they are weighed in total dry conditions (M_1). Then, they are immersed in fresh water in a container at room temperature for 24 hours. After 24 hours, they are removed, wiped out of any traces of water with a cloth, and weighed (M_2). The amount of absorbed water (by mass) is calculated by the formula below:

$$\text{Water Absorption} = (M_2 - M_1/M_1) * 100\% \quad (1)$$

Where,

M_1= dry weight of brick

M_2= wet weight of brick

Lastly, the results are compared first among the PET bricks with different ratios and then with the red brick.

2.4.4 The Thermal Conductivity Test

In a thermal conductivity test, the aim is to determine the thermal conductivity value of a poor conductor. It is often denoted as k with a unit of W/mK. A suitable probe that is connected to the thermal conductivity meter is placed on the sample. A C-therm thermal conductivity analyzer will be used for the test. The device is used for testing ceramics, polymers, composites, etc. Then, the heater's current value is selected to complete the measurement. After the measurement, the heat transfer coefficient of the sample is shown in tabular form. The results of this test show the thermal conductivity coefficients (k) of the bricks. Then, the results are compared first among the PET bricks with different ratios and then with the red brick. The aim of the test is to find the brick that is the least conductive.

3. RESULT AND DISCUSSION

After the production of the bricks, they were first weighed. The weight proportions of each brick are as follows:

Table 1. The weight proportions of each brick

	PET (gr)	Sand (gr)	Clay (gr)	Total (gr)
Ratio 1:2	537	1073	-	1610
Ratio 1:3	399	1196	-	1595
Ratio 1:4	295	1180	-	1475
Red brick	-	-	1900	1900

As seen in Table 1, S3 has the lightest mass among them, with a value of 1475 g. S2 and S1 are 1595 g and 1610 g, respectively. Red brick is the heaviest brick, with a mass of 1900 g. In this study, as in other studies, bricks with pet content were found to be lighter than red bricks. The weight of a 0.5-liter bottle that is made of PET is approximately 10.35 grams. Therefore, 295 grams of PET powder are used in the production of S3, which is equivalent to 28.5 bottles. For S1, it is 52, and for S2, it is 38,5 PET bottles. The material cost of the bricks was zero since waste PET and FS were provided free of charge by the factories. Only natural gas, which was used as fuel during production, could be shown as an expenditure. Red bricks are made of clay, and mining is required to obtain the material. Therefore, mining is an expenditure for red brick production. Moreover, red brick requires staying in a tunnel kiln at 1050 °C for 3.5 days during production, while in the production of PET-sand brick, two containers were used for sand and PET separately at 220-270 °C for 50 minutes. Therefore, the production of PET-sand bricks consumes less energy and is more economical. Energy savings were achieved as there was no need for a high-temperature ceramic furnace as in the production of red bricks. In addition, this production method could reduce the air pollution from brick kilns due to the long production time of red brick. To solve this problem, this study explored how the use of plastic bricks can be a cost-effective, beneficial, and sustainable solution, as well as an effective way to manage the country’s plastic waste and the environmental degradation caused by it. In the production of S1 and S2, the mixtures were blended very well. However, S3 fell apart due to having less PET than the other two PET-sand bricks. An insufficient situation in the production of PET-sand bricks was not working with higher pressures. During the production of the bricks, higher pressure was needed in the molding process. The advantage of working with high pressure is that the gaps formed in the bricks are as small as possible.

3.1 The Three-point Flexural Test Results

In a three-point flexural test, the brick's ability to resist deformation was examined. Before the test, the dimensions of the red and PET-sand bricks were measured. The locations where the load would be applied under three-point bending were marked, and the length of the support was noted. The brick was placed on the stage of the 3-point bending fixture of the device. The servo controller device was used for operating the tests. Loading was applied continuously until failure, and the maximum loads were recorded. After the failure, the stress vs. stroke (TD2) graph is drawn. Then, the results were compared first among the PET bricks with different ratios and then with the red brick. The aim was to test the samples for their strengths. (where length of brick: 210 mm, rate of loading = 0,5 mm/dk and T = 25 °C (room temperature)

The diameter of the support noses is 30 mm x 2 = 60 mm, (2)

Effective span= (210-60) mm = 150mm (3)

Table 2. Results of the three-point flexural test

Sample	Maximum Load (kN)	Maximum Stress (MPa)
Red Brick	4,63	13,02
Sample 1	8,52	17,04
Sample 2	4,76	10,58
Sample 3	2,70	6,67

As seen from Table 2, the highest maximum load was applied to S1. It had the highest maximum stress, which was 17.04 Mpa; red brick was the second one with 13.02 Mpa; S2 was the third one with 10.58 Mpa; and lastly, S3 had the lowest value, which was 6.67 Mpa. The broken bricks are shown in Figure 1. It was observed that the PET addition had increased the strength of the brick. It has been determined that S1 is a good composite as a construction material.

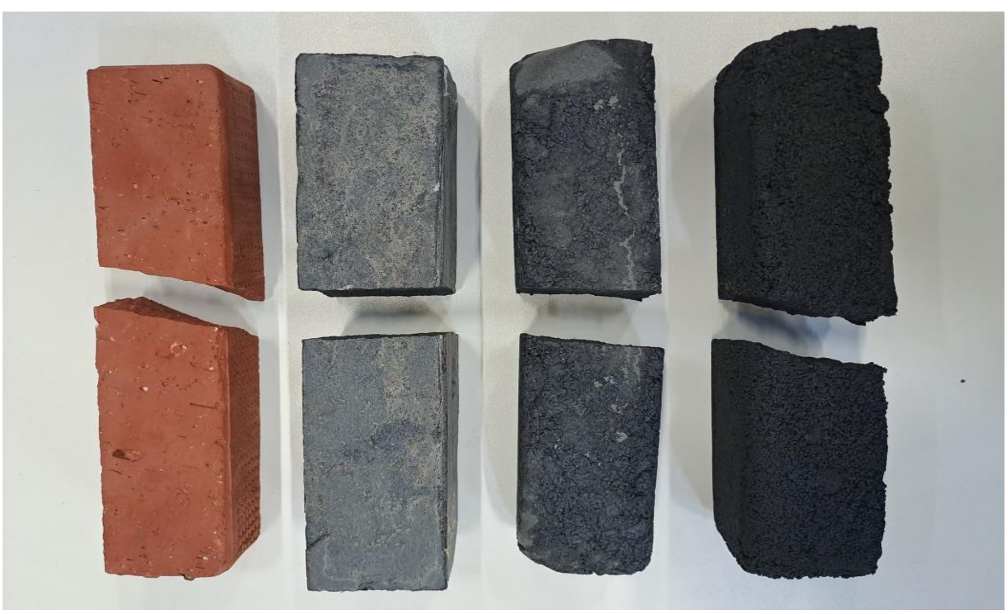

Figure 1. Broken sample bricks after three-point flexural test

Figure 2 shows the curves that are collected in a single stress vs. stroke (TD2) graph. It is understood that S1 has the highest maximum stress.

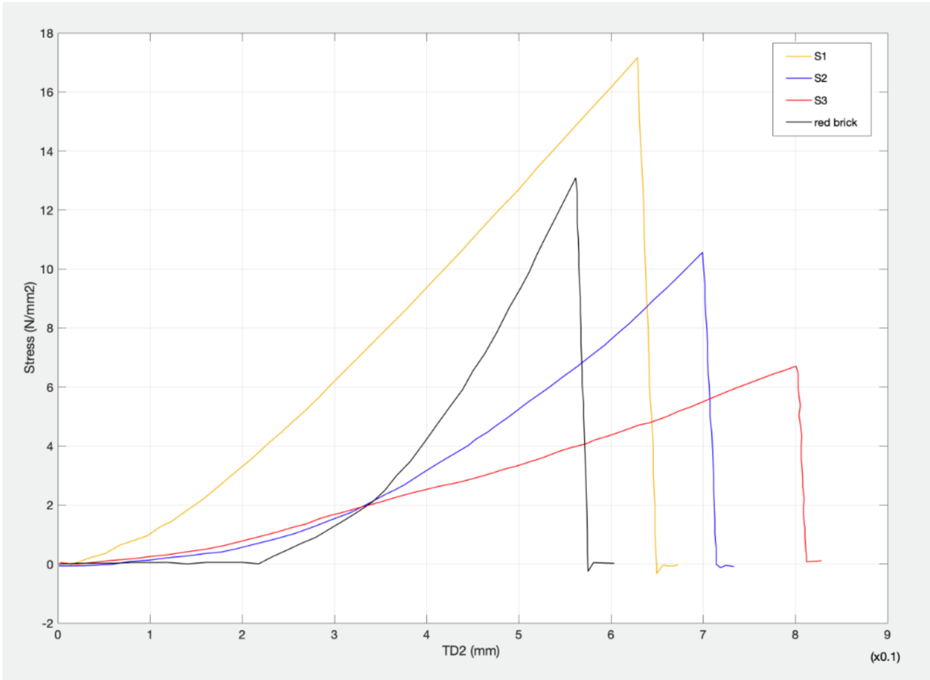

Figure 2. Stress vs stroke (TD2) graph of all bricks

3.2 The Impact Test Results

In the impact test, PET-sand bricks and the red brick were dropped from 1 meter. The red brick fell apart in two pieces (Figure 3.a). S1 (Figure 3.b) and S2 (Figure 3.c) were not broken; however, S3 (Figure 3.d) was already falling apart before freefall, and after the fall, while small pieces were separated from the edges, there was no complete breakage.

The aim of this test was to ensure the proper bond in a brick so that it would not break easily. S1 and S2 were not broken, the test results are considered passed, and the bricks are considered to be of good quality. However, small pieces were separated from the edges of S3, and the red brick was broken, which means their impact values are low, and they are not acceptable for construction work. Their impact tests were failures. This test result showed that S1 and S2 are impact-resistant and good-quality bricks.

Figure 3. a) Impact test result of red brick b) Impact test result of S1 c) Impact test result of S2 d) Impact test result of S3

3.3 The Water Absorption Test Results

In the water absorption test, the quantity of water being absorbed was determined. After cooling each brick to room temperature, they were weighed in total dry conditions (M1). Then, they were immersed in fresh water in a container at room temperature for 24 hours. After 24 hours, they were taken out of the water, wiped out of any traces of water with a cloth, and weighed (M2). The water absorption percentages (by mass) were calculated as follows:

Table 3. Results of the Water Absorption Test

	M1(dry)	**M2(wet)**	**%water(gr/gr)**
Red Brick	1900	1966,5	3,20
S1	1610	1666	0,35
S2	1595	1616	1,31
S3	1475	1497	1,46

In the water absorption test, Table 3 shows that S1 has the lowest water absorption with 0.35%. S2 is the second one, with the lowest value of 1,31%. S3 is the third one, with a value of 1,46%. The red brick has the highest percentage, with a value of 3,2% when compared to S1, S2, and S3.

Absorbed water decreases the durability of the brick. For clay bricks, to increase the density and decrease the water absorption, the firing temperature must be increased. According to the results, S1 has the lowest value and is more durable than the other bricks.

3.4 The Thermal Conductivity Test Results

In the thermal conductivity test, the aim was to determine the thermal conductivity, k value, of a poor conductor since the brick would be used as pavers. The results of the experiment were taken from the computer. Each k value was found by averaging the highest five data in the tables. According to the results, S3 has the lowest conductivity with 0.165 W/mK; followed by Red Brick with 0.713 W/mK; S2 with 0.955 W/mK; and lastly, S1 with the highest conductivity with 1.009 W/mK.

A high thermal conductivity is a sign of a good heat conductor. It seems that S3 is the one that is suitable for the purpose; however, the reason behind the lowest value is the air gaps inside the brick. Since the thermal conductivity of the air is 0.025 W/mK when we compare the PET sand bricks, there is a huge difference between S3 and other PET-sand bricks with different ratios [16]. The reason for the large air gaps is due to the low PET ratio, which was used as a bonding agent between the sand particles. The test showed that, as far as thermal conductivity is concerned, the red brick is the most suitable among the other bricks.

$$\text{Conductivity of a brick} = k_b = \frac{k_{b1}+k_{b2}+k_{b3}+k_{b4}+k_{b5}}{5} \tag{4}$$

$$\text{Conductivity of red brick} = k_{rb} = \frac{0{,}717+0{,}714+0{,}713+0{,}711+0{,}710}{5} = 0.713\text{W/mK}$$

$$\text{Conductivity of S1} = k_{S1} = \frac{1{,}012+1{,}009+1{,}008+1{,}008+1{,}008}{5} = 1.009\text{ W/mK}$$

$$\text{Conductivity of S2} = k_{S2} = \frac{0{,}981+0{,}972+0{,}967+0{,}932+0{,}925}{5} = 0{,}955\text{ W/mK}$$

$$\text{Conductivity of S3} = k_{S3} = \frac{0{,}167+0{,}166+0{,}165+0{,}164+0{,}163}{5} = 0{,}165\text{ W/mK}$$

4. CONCLUSION

This research has investigated the possibility of using sustainable and affordable alternative bricks that are made of waste PET and foundry sand as a substitute for red bricks. The main goal of this study was to produce bricks that are stronger, lighter, cheaper, have less water absorption, and have less thermal conductivity than red bricks by doing experiments with different ratios of the materials.

After the production of the bricks, they were weighed. S3 is the lightest sample, with a weight of 1475 grams. During the production of S1 and S2, the PET and sand blended very well. However, S3 fell apart due to having less PET than the other two PET-sand bricks. For this reason, although the lightest brick was S3, it was not suitable as an image because there were some scatterings of the brick. Furthermore, when production times and temperatures are considered, red bricks need to stay in a tunnel kiln at 1050℃ for 3.5 days during production; however, two containers were used for sand and PET, and they were heated on a gas cooker at 220-270℃ in 50 minutes. Energy savings were achieved as there was no need for a high-temperature ceramic furnace as in the production of red bricks. Since less energy is consumed, the production of PET-sand bricks is more economical than the production of red bricks.

Moreover, the PET-sand bricks and red bricks were tested for three-point flexural, impact, water absorption, and thermal conductivity. The result of the tests showed that in the three-point flexural test, PET addition increased the strength of the brick. S1 is a good composite. The flexural strength of S1 showed some fair results in its structural efficiency when compared to the red brick. In the impact test, S1 and S2 did not break, which shows high impact values. However, the red brick and S3 bricks were broken, so the impact test failed. These test results showed that S1 and S2 are impact-resistant, good-quality bricks, and acceptable for construction work. In the water absorption test, the PET-sand bricks have an advantage over clay bricks. In the water absorption test, the least amount of water was absorbed by S1 at 0.35%. Absorbed water decreases the durability of the brick. Therefore, S1 performed well in the water absorption test. Lastly, in the thermal conductivity test, the red brick has the lowest conductivity with 0.713 W/mK. The test showed that, as far as thermal conductivity is concerned, the red brick is the most suitable among the other bricks.

With this study, it was proven that a good-quality PET-sand brick, S1, could be produced. When it is compared to commercial red brick, a brick that is lighter, more durable, more economical, absorbs less water, and consumes less energy due to its shorter production time and lower working temperature has been produced. However, the desired result could not be obtained in terms of thermal conductivity.

REFERENCES

[1] Britannica, 2023. "*polyethylene terephthalate*", https://www.britannica.com/science/polyethylene-terephthalate [Access date: 23 September 2023]

[2] Sin, L. T., Tueen, B. S., 2023. “*Plastics and environmental sustainability issues*”, https://doi.org/10.1016/B978-0-12-824489-0.00006-4 pp 1-43 [Access date: 20 September 2023]

[3] The statistics portal for market data, 2023. “*Sales volume of bottled water in the United States from 2010 to 2021*”, https://www.statista.com/statistics/237832/volume-of-bottled-water-in-the-us/ [Access date: 1 June 2023]

[4] Stanford University. “*Frequently Asked Questions: Benefits of Recycling*”, https://lbre.stanford.edu/pssistanford-recycling/frequently-asked-questions/frequently-asked-questions-benefits-recycling#:~:text=Plastic.,cubic%20yards%20of%20landfill%20space [Access date: 25 May 2023]

[5] Nair, A., 2023. Bio Market Insights. "*Biggest Breakthrough in Plastic Recycling*", https://worldbiomarketinsights.com/biggest-breakthrough-in-plastic-recycling/ [Access date: 10 December 2022]

[6] World Wildlife Fund, 2023. "Plastic in our oceans is killing marine mammals", https://wwf.org.au/blogs/plastic-in-our-oceans-is-killing-marine-mammals/ [Access date: 28 June 2023]

[7] Tittarelli, F., 2018. "*Waste and Supplementary Cementitious Materials in Concrete: Waste foundry sand",* https://doi.org/10.1016/j.conbuildmat.2017.09.010 pp. 121-147 [Access date: 2 February 2023]

[8] Wienerberger, 2024. How are bricks made? https://www.wienerberger.co.uk/tips-and-advice/brickwork/how-are-bricks-made.html [Access date: 30 April 2024)

[9] ArchDaily Team, 2017. Archdaily. "*Housing Construction in Argentina Uses Recycled PET Bricks*", https://www.archdaily.com/885340/housing-construction-in-argentina-uses-recycled-pet-bricks [Access date: 22 November 2022]

[10] Material district, 2018. "*Bricks Made From Recycled Pet Bottles*", https://materialdistrict.com/article/bricks-recycled-pet-bottles/ [Access date: 18 September 2022]

[11] Shiell, A., 2020. "*India Based Rhino Machines Introduces Brick Made From Recycled Plastic and Sand*", https://archello.com/news/india-based-rhino-machines-introduces-brick-made-from-recycled-plastic-and-sand [Access date: 13 June 2022]

[12] Mukherjee, A., 2021. "*Rhino Bricks, Eco-friendly bricks made from recycled sand and plastic waste, Cheaper and stronger than clay bricks*", https://mad4india.com/mad-for-nature/rhino-bricks-eco-friendly-bricks-by-rhino-machines/ [Access date: 13 June 2022]

[13] Thukral, C., 2020. "*Recycled Sand and Plastic Waste are Used to Make Sustainable Brick!*", https://www.yankodesign.com/2020/06/15/recycled-sand-and-plastic-waste-are-used-to-make-this-sustainable-brick/ (2020) [Access date: 5 September 2022]

[14] Mcdonald, L., 2020. "*Plastic Sand Bricks Offer Affordable And Sustainable Housing In Kenya*", https://ceramics.org/ceramic-tech-today/ceramic-video/video-plastic-sand-bricks-offer-affordable-and-sustainable-housing-in-kenya [Access date: 15 June 2022]

[15] Thoudam, K., Hossiney, N., Lakshmish Kumar, S., Alex, J., Prakasan, S., Chandra, S., Urs, Y., Arunkumar, A.S. Recycled Surgical Mask Waste as a Resource Material in Sustainable Geopolymer Bricks. Recycling. https://doi.org/10.1016/j.conbuildmat.2024.135197 (2023) [Access date: 30 April 2024]

[16] Material Properties, 2023. "*Air-Density-Heat Capacity-Thermal Conductivity*", https://material-properties.org/air-density-heat-capacity-thermal-conductivity/ [Access date: 3 April 2023]